MASTERARBEIT | MASTER'S THESIS

Titel | Title

OPTO-MECHATRONICAL CHARACTERIZATION OF THE 1.5 M TELESCOPE OF THE LEOPOLD-FIGL OBSERVATORY FOR ASTROPHYSICS

verfasst von | submitted by

Costin-Florin Luchian

angestrebter akademischer Grad | in partial fulfilment of the requirements for the degree of

Master of Science (MSc)

Wien | Vienna, 2025

Studienkennzahl lt. Studienblatt | Degree programme code as it appears on the student record sheet:	UA 066 861
Studienrichtung lt. Studienblatt | Degree programme as it appears on the student record sheet:	Masterstudium Astronomy
Betreut von | Supervisor:	ao. Univ.-Prof. Dr. Werner Zeilinger

Acknowledgements

I wish to thank my supervisor, Univ.-Prof. Dr. Werner W. Zeilinger, for his invaluable support over the last two years. I would also like to thank my co-supervisors, Univ.-Prof. Dr.sc.techn. Dr. Georg Schitter and Dipl.-Ing. Andreas Sinn from the Automation and Control Institute (ACIN) at TU Wien for their help with developing and implementing the metrology system required for this work. I am also grateful to Florian Kreuzmair, who has worked beside me on his project at the "Leopold-Figl" Observatory for Astrophysics. I'd like to also thank Andreas Zeiner and the Konrad Technologies team, currently working on the system-wide upgrade of the LFOA, for their assistance in developing the web-based graphical interface and their continued work on making the LFOA telescope a competitive tool for the upcoming years. Lastly, I'd like to mention my friends and family who have supported me over the course of this project, and to whom I am very thankful. To everyone, thank you!

Abstract

Regardless of size, the imaging quality of ground-based reflective telescopes is influenced by numerous factors, among which are mechanical deformations in the telescope structure itself. Depending on the telescope's condition and the surrounding environment, these systems could be susceptible to errors due to flexure, aging, gravitational and thermal influences, which may lead to a considerable degradation of imaging quality. The 1.5 m telescope at the "Leopold-Figl" Observatory for Astrophysics (LFOA) is Austria's largest reflective telescope, and after more than 50 years of operation its optical, imaging, and structural properties must be evaluated. An opto-mechanical analysis of the 1.5m LFOA was realized, leading to a characterization of its expected mechanical disturbances and their corresponding optical errors. Currently, access to ground-based telescopes can be a valuable resource to scientists and enthusiasts alike. This work aims to ensure that the 1.5m LFOA telescope is a competitive, accessible, and sustainable tool for everyone. This was achieved through the adaptation and implementation of a metrology system originally developed at the Automation and Control Institute (ACIN) at TU Wien. With the help of this system, measurements of the five degrees of freedom between the primary and secondary mirror of the telescope have been made, which show the telescope behaviour to be within the expected parameters. These measurements have found an overall expected axial defocus of 36 ± 9 µm, a tip rotation of 8 ± 5 arcsec, a tilt rotation of 4 ± 2 arcsec, X-axis displacement of 73 ± 3 µm, and a Y-axis displacement of 118 ± 16 µm. These disturbances combined lead to an expected Strehl ratio of $S_R = 0.94$ while the worst-case scenario considered would result in $S_R = 0.77$. On their own, these disturbances are negligible; however, if combined with other optical errors, their correction could improve imaging quality. Because of this, several active optics solutions have been discussed as possible upgrades to the telescope system.

Kurzfassung

Die Abbildungsqualität erdgebundener Spiegelteleskope wird neben der Größe des Teleskops von zahlreichen weiteren Faktoren beeinflusst, darunter auch mechanische Verformungen der Teleskopstruktur selbst. Je nach Zustand des Teleskops und dessen Umgebung können diese Systeme aufgrund von Biegung, Alterung, Gravitation und thermischen Einflüssen fehleranfällig sein, was zu einer erheblichen Verschlechterung der Abbildungsqualität führen kann. Das 1,5-m-Teleskop des Leopold-Figl-Observatoriums für Astrophysik (LFOA) ist Österreichs größtes Spiegelteleskop. Nach über 50 Jahren in Bertieb werden seine optischen, bildgebenden und strukturellen Eigenschaften bewertet. Eine optomechanische Analyse des 1,5-m-LFOA führte zu einer Charakterisierung der erwarteten mechanischen Störungen und der damit verbundenen optischen Fehler. Derzeit kann der Zugang zu erdgebundenen Teleskopen eine wertvolle Ressource für Wissenschaftler und Enthusiasten gleichermaßen sein. Das Ziel dieser Arbeit ist demnach, sicherzustellen, dass das 1,5-m-LFOA-Teleskop ein wettbewerbsfähiges, zugängliches und nachhaltiges Werkzeug ist. Dies wurde durch die Anpassung und Implementierung eines ursprünglich am Institut für Automatisierungs- und Regelungstechnik (ACIN) der TU Wien entwickelten Messsystems erreicht. Mithilfe dieses Systems wurden Messungen der fünf Freiheitsgrade zwischen dem Primär- und Sekundärspiegel des Teleskops durchgeführt, welche zeigten, dass das Teleskopverhalten innerhalb der erwarteten Parameter liegt. Diese Messungen ergaben einen insgesamt erwarteten axialen Defokus von 36 ± 9 µm, eine Spitzenrotation von 8 ± 5 Bogensekunden, eine Neigungsrotation von 4 ± 2 Bogensekunden, eine X-Achsenverschiebung von 73 ± 3 µm und eine Y-Achsenverschiebung von 118 ± 16 µm. Gemeinsam führen diese Störungen zu einem erwarteten Strehl-Verhältnis von $S_R = 0,94$, während das betrachtete Worst-Case-Szenario $S_R = 0,77$ ergeben würde. Diese Störungen können alleinstehend ignoriert werden, in Kombination mit anderen optischen Fehlern allerdings, könnte durch deren Korrektur die Bildqualität verbessert werden. Aufgrunddessen wurden mehrere aktive Optiklösungen als mögliche Upgrades des Teleskopsystems diskutiert.

Contents

List of Tables

List of Figures

1. Introduction

The base purpose of a telescope is to provide high-quality images of distant objects. A telescope should be able to be pointed at a desired object, track its motion across the sky, and, using precise optics, maintain a clear image of its target. They are therefore complex and often motorised moving systems, which, together with precise optics, can be a powerful tool in the imaging and study of astronomical objects. The main subject of this thesis will be the relation between the mechanical and optical behaviour of the 1.5m telescope at the “Leopold-Figl” Observatory for Astrophysics (LFOA) and how it affects its use as an astronomical ground based telescope.

1.1. Basic Telescope Theory

Telescopes, like most practical optical systems, have centered optics, meaning that a unique axis of symmetry can be assumed. These systems are considered ideal, having fewer degrees of freedom, and non-centered systems being much more complex. The theory of ideal optics was first introduced by Gauss in 1841 [8] and was further explained in the context of reflecting telescope optics by R. N. Wilson in his “Reflecting Telescope Optics I” [1]. In this work, Wilson covers the basics of telescope theory for various types of reflective telescopes from Gaussian (ideal) optics to aberration theory.

While in the early history of telescope manufacturing, the refractor was the more popular telescope architecture, modern telescopes are most commonly reflective telescopes. In this category, the most important types are the Gregory and Cassegrain telescopes, the latter of which has, over time, become the preferred choice for astronomers. Fig. 1.1 shows an overview of the evolution of major ground based telescopes and observatories. Starting from William Herschel’s “40-foot” telescope marking the beginning of large reflectors, to George Ritchey’s 60-cm telescope at Yerkes, considered the first to posses all the characteristics of a modern telescope, followed by ESO’s Very Large Telescope (VLT), one of the most advanced observatories of the last two decades, and finally ESO’s upcoming Extremely Large Telescope (ELT), which is expected to push the frontier of ground based telescopes forward.

The design of the last two telescopes is a variant of Cassegrain telescope architecture known as a Ritchey-Chretien telescope (or RC-focus), which has been adapted by many telescopes in the last few decades as it achieves a wider field than other Cassegrain types while also diminishing off axis optical errors known as coma aberrations. The 1.5m LFOA

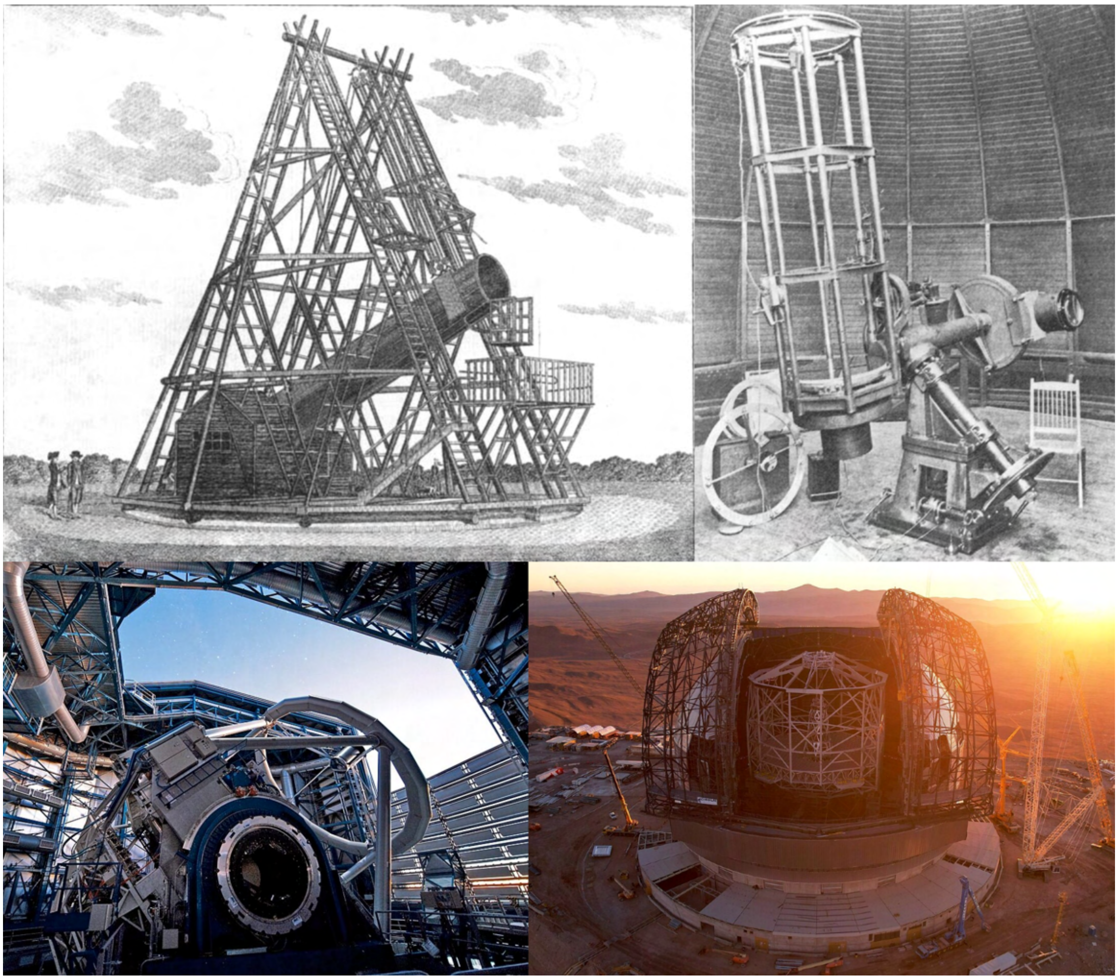

Figure 1.1.: The evolution of the reflector. The telescopes shown appear in the following order: William Herschel's "40-foot" telescope (top-left, reproduced from [1], courtesy Deutsches Museum, Munich); George Ritchey's 60-cm telescope at Yerkes (top-right, reproduced from [1], courtesy Deutsches Museum, Munich); ESO's 4m VLT (bottom-left, courtesy of ESO, photograph by José Francisco Salgado) and ESO's upcoming 39m ELT (bottom-right, courtesy of ESO, photograph by G. Vecchia).

l	m	n=0	n=1	n=2	n=3	Order
0	0		${}_1k_{11}\sigma\rho\cos\phi$			First
	2	${}_0k_{20}\rho^2$				$N_H = 1$
2	0		${}_3k_{11}\sigma^3\rho\cos\phi$	${}_2k_{22}\sigma^2\rho^2\cos^2\phi$		Third
	2	${}_2k_{20}\sigma^2\rho^2$	${}_1k_{31}\sigma\rho^3\cos\phi$			$N_H = 3$
	4	${}_0k_{40}\rho^4$				
4	0		${}_5k_{11}\sigma^5\rho\cos\phi$	${}_4k_{22}\sigma^4\rho^2\cos^2\phi$	${}_3k_{33}\sigma^3\rho^3\cos^3\phi$	
	2	${}_4k_{20}\sigma^4\rho^2$	${}_3k_{31}\sigma^3\rho^3\cos\phi$	${}_2k_{42}\sigma^2\rho^4\cos^2\phi$		Fifth
	4	${}_2k_{40}\sigma^2\rho^4$	${}_1k_{51}\sigma\rho^5\cos\phi$			$N_H = 5$
	6	${}_0k_{60}\rho^6$				

Table 1.1.: Aberration types according to Hamilton's Characteristic Function (Eq. 1.1), from [1].

also uses primarily this RC-focus variant of the Cassegrain design; therefore, the following theory will take into account Cassegrain architecture.

1.1.1. Geometrical Wavefronts and Wavefront Aberration

An important concept in telescope theory is that of geometrical wavefronts. This concept was introduced by Fermat in 1667 and describes a surface of constant phase, orthogonal to the path of rays within the optical system. While it can be used to describe most of telescope optics, the approximation of geometrical optics has limitations such as resolution and optical errors, which require an understanding of wavefronts and wavefront aberration. In this context, a perfect image is associated with a perfectly spherical wavefront, while phase deviations are the study of aberration theory and provide a description of errors in optical systems.

The Characteristic function, published by Hamilton in 1833 [9], uses the symmetry of centered optics to describe the optical path difference of the wavefront aberration. This aberration function was deduced in terms of three parameters: aperture radius ρ, field radius σ, and azimuth angle ϕ. Due to symmetry, these parameters can only appear as ρ^2, σ^2, and $\rho\sigma\cos\phi$, and the generalised form of the Characterisation function can be written as Eq. 1.1:

$$W(\rho,\sigma,\theta) = \sum_{(l+n)} k_{(m+n),n}\sigma^{(l+n)}\rho^{(m+n)}\cos^n\phi \tag{1.1}$$

The order of each aberration can be described by $N_H = (l + m + 2n) - 1$, which is derived from the sum of coefficients of σ and ρ in Eq. 1.1. Table 1.1 shows the first, third, and fifth order aberrations and their dependence on ρ, σ, and ϕ.

The first row represents first order aberrations, which are errors in the region of Gaussian optics. The first term, ${}_0k_{20}\rho^2$, is a defocus error while the second term, ${}_1k_{11}\sigma\rho\cos\phi$, is a

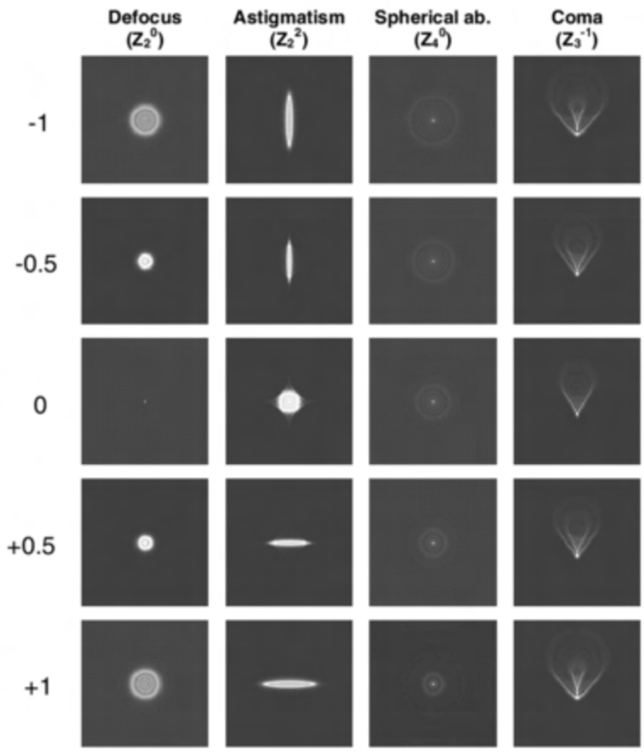

Figure 1.2.: Optical effect of defocus error and the following third order aberrations: coma, astigmatism, and spherical aberration. (reproduced from [4])

tilt error, caused by a tilt in the imaging wavefront. The next five terms in the second row are third order aberrations or Seidel aberrations. The individual third order error types are third order spherical aberration (${}_0k_{40}\rho^4$) and field curvature (${}_2k_{20}\sigma^2\rho^2$) in the first column ($n = 0$), distortion (${}_3k_{11}\sigma^3\rho\cos\phi$) and third order coma (${}_1k_{31}\sigma\rho^3\cos\phi$) in the second column ($n = 1$), and third order astigmatism (${}_2k_{22}\sigma^2\rho^2\cos^2\phi$) in the third column ($n = 2$). Together with the two Gaussian terms, they constitute the most dominant errors in most optical systems, including telescope imaging.

The fifth and higher order terms are less dominant and can be interpreted as combinations of the previous types of aberrations. Terms in the first column ($n = 0$), with no dependence on azimuth angle ϕ, are a combination of spherical aberrations and field curvatures, terms in columns with odd n are considered "comatic" effects, and terms in columns with even n, "astigmatic" effects. Fig. 1.2 illustrates the physical effects on image quality of some of these wavefront aberrations, namely defocus, astigmatism, coma, and spherical aberration. [1]

1.1.2. Indicators of Image quality

The imaging quality of a telescope has been historically expressed as angular aberrations, usually measured in arcsec, and linked with achieving the angular resolutions required for the observation of astronomical objects in our solar system. It is understood that this angular resolution can often be limited by atmospheric effects or telescope errors; however, any optical system has a fundamental resolution limit arising from the physics of light diffraction in said system. In astronomy, an optical system is said to be diffraction-limited when it achieves its theoretically ideal angular resolution and is essentially limited only by diffraction.

One of the earliest image quality specifications states that an optical system can be considered diffraction-limited as long as its wavefront error does not exceed $\lambda/4$, where λ is the wavelength of observed light. This term is known as the Rayleigh limit, it is a general approximation which works reasonably well for small telescopes with apertures of about $D \sim 75cm$, such that the diameter of the Airy disk, d_A, is a significant fraction of the atmospheric seeing.

Introduced in 1902 by Karl Strehl, the Strehl ratio, S_R, is another important criterion for the imaging quality of an optical system. Its value is given by the ratio between the peak observed intensity and the maximum possible intensity in an ideal system (Eq. 1.2), and it describes aberrations in the central diffraction peak. Therefore, it can also be expressed in terms of the root mean square wavefront error W_{rms} as shown in Eq. 1.2. The standard specification for image quality given by the Strehl ratio is that an optical system is considered to be diffraction-limited as long as the loss in intensity from the diffraction peak due to aberrations does not exceed 20%, or in other words, $S_R = 0.8$.

$$S_R \equiv \frac{I(Q)}{I_0} = 1 - (\frac{2\pi}{\lambda})^2 W_{rms}^2 \tag{1.2}$$

Similarly to the Rayleigh limit, the specification of Strehl ratio, $S_R = 0.8$, is also arbitrary. The theoretical basis for justifying this criterion was given in 1947 by Maréchal [10], connecting the combined aberration coefficients and their corresponding wavefront errors to their effect on the diffraction pattern. This work establishes that aberrations can be considered small if the structure of the central diffraction peak is preserved. Under this approximation, the effects of small aberrations are sufficiently described by the rms wavefront error, W_{rms}. For stronger aberrations, $S_R < 0.5$, which cause a more significant reduction of the central peak, S_R and W_{rms}, no longer provide a useful description of aberration effects on image quality. A more detailed description of the individual coefficient making up the wavefront error is needed in this situation, requiring a more complex approach. [2]

Sources of error	Bandpass (Hz)	
Optical design and manufacture	–	(fixed)
Errors of the structure (mirror supports, focus and centering)	$< 10^{-3}$	(fixed → minutes)
Maintenance errors (structure and mirror supports)	$10^{-6} \rightarrow 10^{-5}$	(weeks → days)
Thermal distortions: - Mirrors - Telescope structure	 $10^{-5} \rightarrow 10^{-4}$ 10^{-3}	 (days → hours) (minutes)
Mechanical warping of the mirrors	10^{-7}	(years)
Thermal effects of ambient air (site seeing)	$10^{-4} \rightarrow 10^{2}$	(hours → 0.01 s)
Mirror deformations of wind gusts	$10^{-2} \rightarrow 10^{1}$	(minutes → 0.1 s)
Atmospheric turbulences	$10^{-2} \rightarrow 10^{3}$	(1 minute → <1 ms)
Tracking errors	$5 \rightarrow 10^{2}$	

Table 1.2.: Analysis of possible sources of optical errors and their bandpass from R. N. Wilson [2].

1.1.3. Errors in Optical Systems

The imaging quality of ground-based reflective telescopes can be influenced by numerous factors, from aging and warping of the mirrors to structural flexures caused by thermal and gravitational effects or even atmospheric turbulence. Some of these errors are fixed or evolve over the span of days, weeks, or even years, while other errors progress quicker, having a bandpass of minutes or less. An analysis of common sources of error for telescopes can be seen in Table 1.2 from R. N. Wilson's "Reflecting Telescope Optics II" [2] and provides a list of possible telescope errors and their corresponding bandpass. An important feature of these errors is that effects linked with air, atmosphere and changes in seeing caused by these tend to be much faster, in the range of minutes to milliseconds (up to 100 Hz or more), while defects related to changes in the telescope or mirror structures change on much larger timescales, primarily from minutes to hours or days (generally $< 10^{-2}$ Hz). Compensating fast changing atmospheric effects can be a challenge, often tackled by the field of Adaptive Optics; however, structural errors fall in the bandpass of Active Optics ($< 1/30$ Hz).

1.2. Active Optics

Active control systems, or active optics, are a technology used in improving the imaging quality of telescope systems through the process of repositioning telescope mirrors relative to each other or changing their form in such a way as to compensate for optical errors within the system. It is generally concerned with low frequency errors typically related to the telescope's mirrors or mechanical structure. This is in contrast to its counterpart, adaptive optics, which are high frequency control systems tasked with compensating for atmospheric effects. Active optics generally works as an open-loop process, that takes an input from the telescope system and returns a pre-determined output in order to correct any existing errors, while adaptive optics is a closed-loop process, relying on constant feedback from its corrections to operate at higher frequencies.

The introduction of active optics was essential for the size increase of ground based reflective telescopes, which were impractical at the time due to unmanageable optical errors arising from structural instabilities. First efforts of developing active optics took place in the 1970s, as it was initially proposed as a feature for the still in development at the time Hubble Space Telescope (HST). While its implementation in the HST was not approved, it went on to be developed at ESO and implemented in ground based telescopes such as the 3.5m NTT in 1989 and the VLT in 1998. [2]

1.2.1. Active Optics in Practice

The 3.5m New Technology Telescope (NTT) was developed by ESO and had its first light in 1989. Its Active control system was developed by R. N. Wilson and was one of the earliest implementations of this technology, being deemed "the first fully active telescope". A schematic of the servo-loop used in the active optics of the NTT can be seen in Fig. 1.3. In its operation, the image of a reference star in the field of view of the telescope is "borrowed" by a Shack-Hartman image analyser. The image produced is then analysed, and necessary corrections are sent to the axial supports of the primary mirror and the position actuators of the secondary mirror. The intended goal, which this control system successfully achieved, was to reduce the effects of opto-mechanical errors until their contributions were comparable to that of local and external seeing. The success of this telescope has served as a proof of concept for the implementation of active optics in both ground-based and space-based applications. Active optics not only improve the optical performance of a telescope, but it does so in a cost effective manner, allowing smaller telescopes, like the 3.5m NTT, to rival the optical efficiency and capabilities of larger telescopes in the range of 8-10m. [5]

Another implementation of active optics can be found at the VLT's Survey Telescope (VST), a 2.6m wide-field telescope located next to the four Very Large Telescope (VLT) unit telescopes. Its first light was in 2011, making it a more recent example of a fully active ground-based telescope control system. The support system for the primary mirror of the VST has two components, an axial and a lateral one. The distribution of the 84 axial supports and 27 lateral supports can be seen in Fig. 1.4. The active support of the secondary mirror, also seen in Fig. 1.4, is based on a hexapod system, a combination of six angled supports which can compensate for 5 degrees of freedom, specifically the X, Y, and Z displacements and rotation around the X and Y-axis. The most critical component of the VST's active optics is considered the primary mirror support system. With its active supports, any potential optical defects of the primary mirror due to manufacturing or warping can be actively controlled and corrected. The secondary mirror supports are

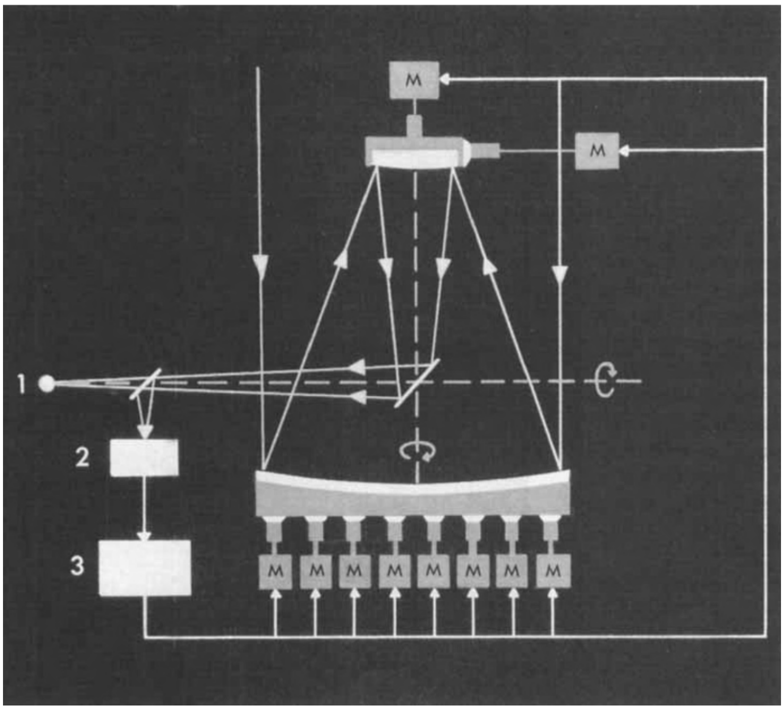

Figure 1.3.: Diagram showing the various elements of the NTT's active optics, including optical focus (1), wavefront analyser (2), Computer (3), primary mirror actuators, and secondary mirror lateral and axial actuators. (reproduced from [5])

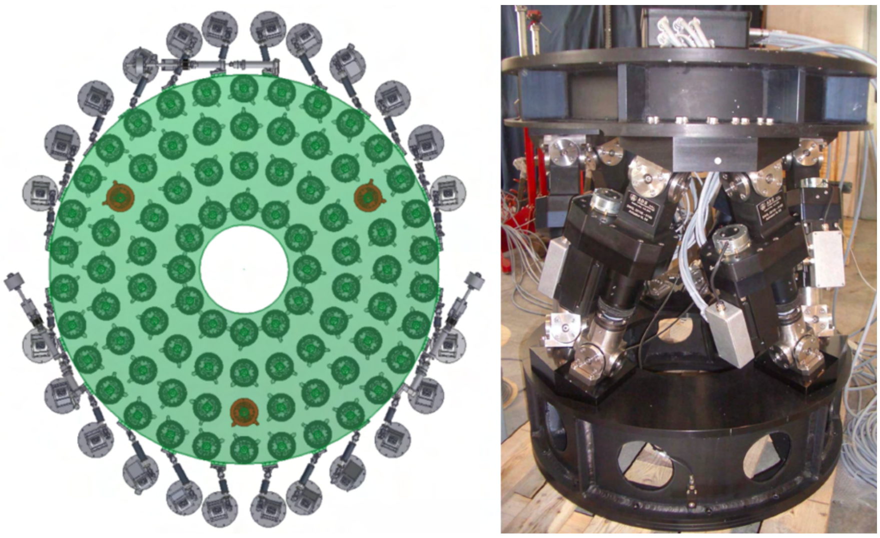

Figure 1.4.: Image representation of the actuator system for the VST's active primary mirror (left) and photograph of the hexapod system for the VST's active secondary mirror (right). (reproduced from [6])

also essential for correcting the relative motion between the two mirrors, reducing errors such as defocus, coma, or off-axis astigmatism. Together, all of these components can reliably reduce the measured errors of opto-mechanical origin of the 2.6m VST telescope, drastically improving its performance. [6] [11]

1.3. The Leopold Figl Telescope

The Leopold-Figl Observatory for Astronomy is home to Austria's largest ground-based optical telescope, a 1.5m class Cassegrain seen in Fig. 1.5. The optical components of the telescope were manufactured by Carl Zeiss, while the mechanism was produced by Rademakers. Starting construction in 1965 and with its scientific operation beginning in 1970, the telescope was designed as a versatile tool that could cover many modes of observation. For this reason, the telescope was built with three possible focus types and a revolving secondary mirror cell that enables these light path changes. Built around a Cassegrain architecture, the three light paths of the telescope are as shown in Fig. 1.6: A Cassegrain focus for spectroscopy, A Coudé focus for high-resolution spectroscopy, and an RC focus for wide-field imaging. [3]

Figure 1.5.: Photograph of the 1.5m LFOA telescope in park position.

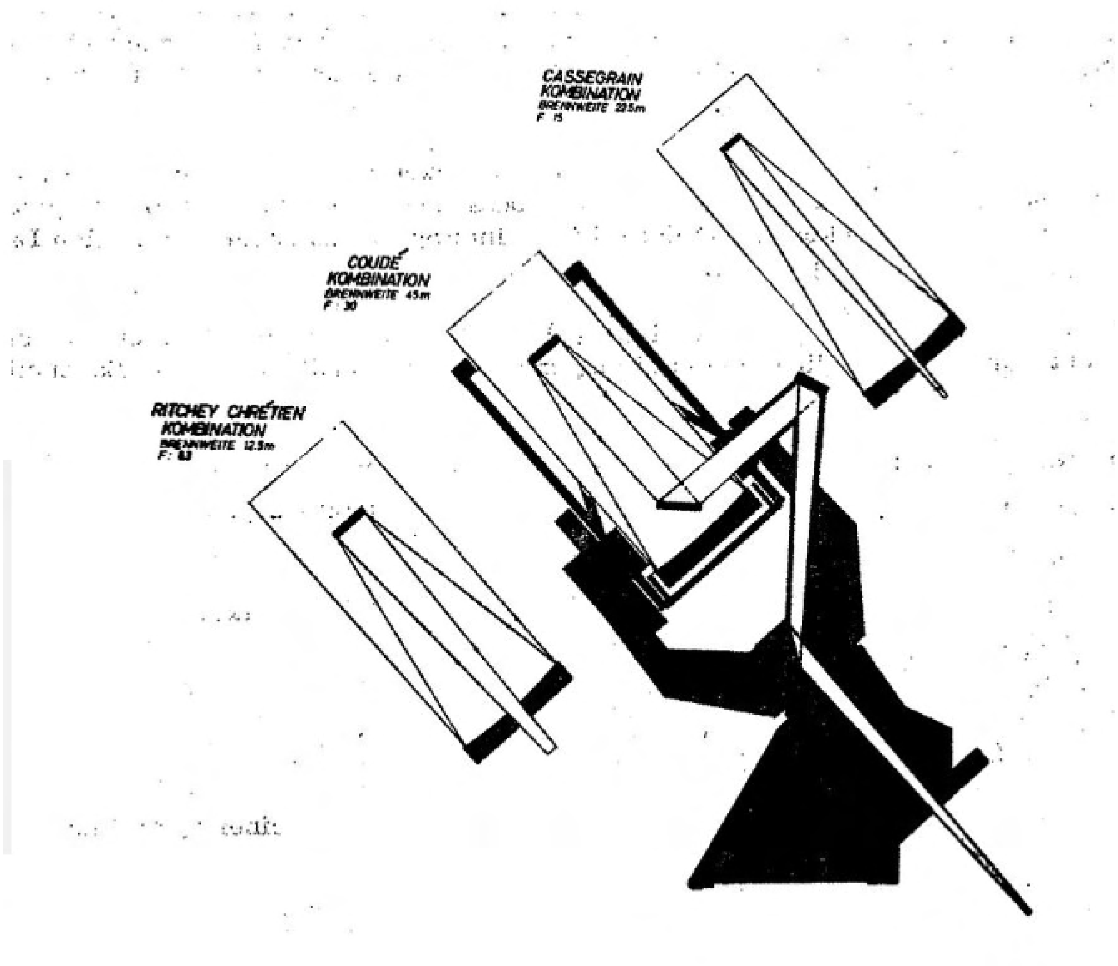

Figure 1.6.: Diagram illustrating the three light paths of the 1.5m LFOA telescope. (reproduced from [3])

Focus Type	D/f	FoV	D_1 [mm]	D_2 [mm]	g [mm]
Casegrain	f/15	$0.5° \times 0.5°$	1524	323	750.5
Ritchey-Crétien	f/8.3	$1.0° \times 1.0°$	1524	519	750.2
Coudé	f/30	$0.1° \times 0.1°$	1524	467.4	10853.6

Table 1.3.: Light paths of the 1.5m LFOA telescope detailing the f-number (D/f), field of view (FoV), mirror diameters for the primary and secondary mirrors (D_1 and D_2) and the effective distance between the focus plane and the primary mirror surface (g) for each of the three focus types, from [3].

The specification of these light paths can also be seen in Table 1.3. The Coudé focus works by redirecting the light path from the center of the primary mirror to a side channel in one of the arms of the telescope and into a chamber underneath the telescope, this has the benefit of making the location of the focus point fixed from the motion of the telescope and thus making any instrumentation placed at this spot much more stable since it does not need to move with the telescope. This observation mode was, however, never used, with only the Cassegrain and RC focus paths ever being equipped with instrumentation. The 1.5m primary mirror of the LFOA telescope consists of an aluminium coated solid block of heat resistant borosilicate glass, which weighs approximately 1 ton, while the entire telescope structure weighs about 23 tons. The reflective aluminium coating of the mirror can be maintained and reapplied on the observatory site, eliminating the risks and costs involved in the transportation of the mirror to a different location. Currently, the only observation mode that is actively in operation is the wide-field RC focus mode. [3]

The location of the LFOA plays a major role in the optical performance of the telescope since limitations can arise from both atmospheric conditions and light pollution. The observatory is located at Mitterschöpfl in the Wienerwald at a height of 890m above sea level. The values for atmospheric seeing for typical observing nights are between 1.5 to 2.0 arcsec, while on exceptional nights they can reach approximately 1.0 arcsec. That being said, meteorological conditions at the location are often unpredictable, making observations with the telescope only possible around 100 days per year on average. While spring and autumn are often the best observing times, during the period from November to April, the snowy conditions and high humidity restrict the use of the telescope. To ensure the safety of the telescope equipment, the observatory monitors certain weather conditions at the site and blocks telescope operations as the weather reaches certain humidity, temperature, and wind speed restrictions. Aside from the atmosphere and weather, another factor for optical performance is light conditions. Despite the remote location of the telescope, its proximity to the city of Vienna still has an observable effect on telescope operations, which has led to the telescope being used to monitor and document Vienna's light pollution. [3] [12]

1.4. Goals and Motivation

A project realised by the Automation and Control Institute (ACIN) at TU Wien [7] has investigated the implementation of an active positioning system for the secondary mirror of a small RC-focus telescope system shown in Fig. 1.7. By using a combination of precise positioning with a newly developed actuator system for the secondary mirror, the image quality of the telescope system was maintained over a varying range of gravitational and thermal influences. Since the metrology system did not obstruct the light path of the telescope, it did not reduce incoming light, as opposed to a wavefront analyser. The actuator system also shows benefits when compared to the "Hexapod" system of the VLT, being less massive and having a smaller footprint. The active positioning system was developed on a 25cm telescope and was designed to be scaled up to 80cm

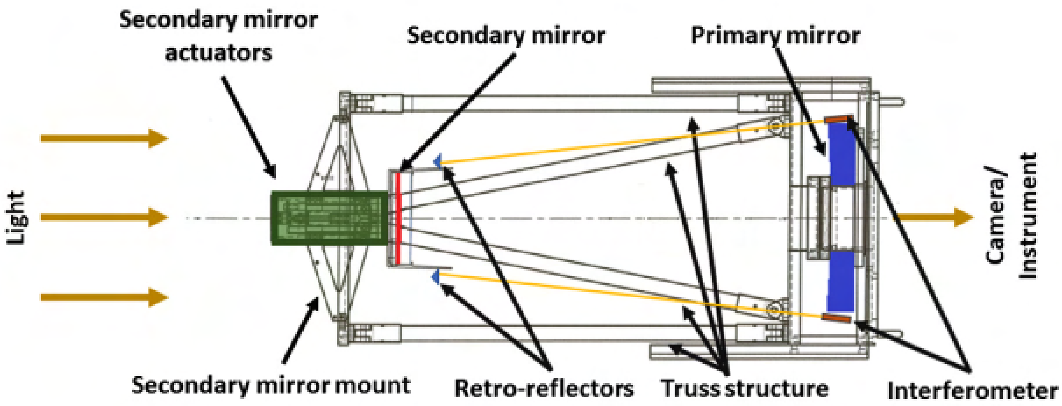

Figure 1.7.: Diagram of the metrology and actuator system installed on the 25cm telescope from ACIN. (reproduced from [7])

telescopes. In collaboration with ACIN, this work will investigate the extension of their active positioning and metrology system to larger telescopes such as the 1.5m LFOA. This active metrology system will serve as the starting point for the instrumentation required in the mechanical analysis of the LFOA telescope.

The maintenance and operation of existing ground-based telescopes is also an important aspect of sustainable research in the field of astronomy. Even 25 years ago, concern has been shown in the works of R. N. Wilson [1] for the uneven attention directed towards the development of cutting-edge observatories at exceptional sites compared to upgrading existing ones. In the past years, however, sustainability has become part of the conversation for the scientific community, and efforts to improve existing infrastructure, such as the development of the Mercator telescope's control system in 2017, are becoming more common. [13]

As previously stated, the goal of this thesis is to study the opto-mechanical behaviour of the 1.5m telescope at the LFOA and make an assessment of its current performance as well as possible improvements. Using the previously discussed tools, a quantitative analysis of the telescope structure was performed. This analysis, together with the presented theory, was used to assess the potential effects of mechanical errors on image quality and discuss the feasibility of implementing active or semi-active technology in order to improve and maintain the imaging quality of this telescope, maintaining its scientific relevance for the future. As ground based observatories are valuable resources in the field of astrophysics, the long term plans of this study are to ensure the continued optimisation of operations at the LFOA as an important asset to the science community and its network of space observatories.

2. Methodology

2.1. Equipment

In order to characterise the opto-mechanical properties of the 1.5m LFOA, the metrology system from the ACIN project has been adapted to suit the larger telescope. The same interferometer system was used for axial defocus and angular displacements, while a new detector had to be introduced to measure the possible lateral displacements between the primary and secondary mirrors of the telescope.

2.1.1. Interferometer

The IDS3010 interferometer from Attocube Systems AG [14] is used for the axial defocus, tip and tilt measurements. It is equipped with M12/C7.6 heads, which have a range of up to 5 meters. The device's compact design is suitable for use in the limited space offered by the telescope, its micrometer range accuracy fits with the measurement needs and its compatibility in extreme environments ensures that the instrument will be operational outside of the controlled lab conditions. Fig. 2.1 shows the interferometer setup with one sensor head and a retroreflector. The instrument can be accessed via a real time digital interface over Ethernet connection. This interface offers an alignment tool with a visible guiding laser. Real time data can also be accessed via IP connection and recorded with the help of a Python program.

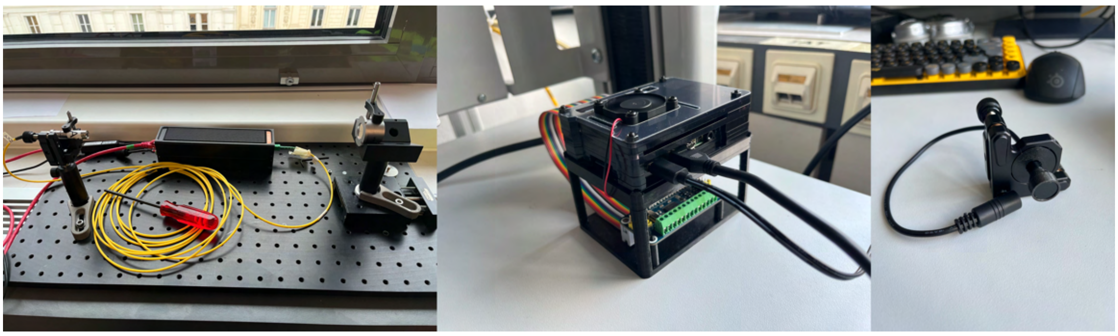

Figure 2.1.: Some of the equipment used for the metrology system, including the interferometer setup with a sensor head and a retroreflector (left), the Raspberry Pi and AD Converter unit (center) and the Laser pointer unit (right).

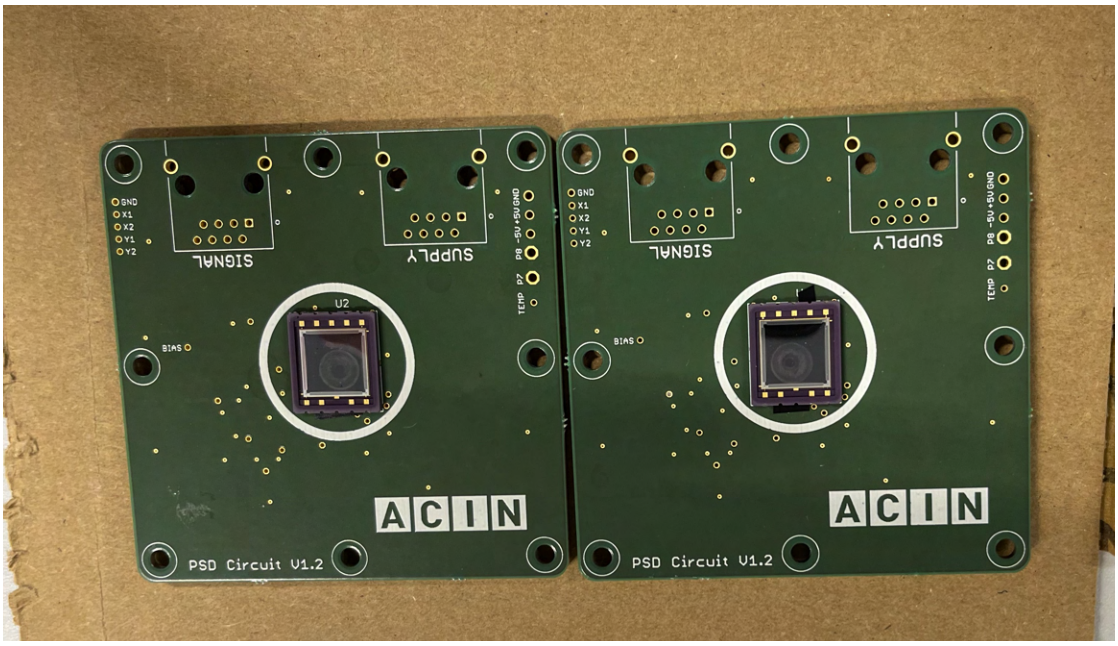

Figure 2.2.: Photograph showing the first iteration of the PSD circuits.

2.1.2. PSD Detector

A pair of Hamamatsu (S5991) surface mountable, high accuracy position sensitive detectors [15] is used to monitor the change in position of a laser onto their detector surfaces. Each detector has a photovoltaic surface (9x9 mm) made up of 4 panels. It has a 4-channel output, which describes the position of an incoming light beam relative to the centre of the detector surface. The chip is integrated within a circuit in order to amplify, filter and record its measured signal. The two PSDs used in this project, along with the first iteration of the PSD circuits, are shown in Fig. 2.2. While lateral displacement alone can be measured with a singular detector, a second one was introduced as an additional source of data, as well as facilitating the investigation of possible rotation around the optical axis between the two mirrors.

2.1.3. AD Converter and Raspberry Pi

A 10-Channel 32-Bit Analog to Digital converter (ADC) [16] is used to read the incoming signal from the PSD circuits. Each detector circuit outputs a 4-channel DC Voltage signal representing the 4 outputs of the PSD chip. It has a variable sampling rate that can be adjusted in order to balance noise levels and signal frequency. The ADC operates as an extension to a Raspberry Pi, which acts as a platform capable of running various processes such as recording, storing and processing data. Normally, the ADC is powered by the Raspberry Pi (0 to 5 V); however, to accommodate the negative voltage coming from the detector circuits, it can operate under an alternative supply in order to record voltages between -2.5 and 2.5 V. The ADC and Raspberry Pi unit are shown in Fig. 2.1 assembled into a shared housing.

2.1.4. Laser

A 2 mW laser with an 850 nm operational wavelength (RLDC850-2-3) [17] is used to bridge the two mirrors of the telescope for the lateral displacement measurement. It has a beam that is focusable up to a 3.5 mm beamwidth and an operational temperature between $-10°$C to $40°$C, making it suitable for the telescope environment. To facilitate a safe lab environment, it is equipped with a 0.9 optical density ND filter. It can be easily adapted to kinetic mounts for use in the lab and for mounting on the telescope. The Laser unit with ND filter and kinetic mount is shown in Fig. 2.1.

2.1.5. PSD Circuit

To convert the PSD signal into a DC Voltage signal for the ADC, an amplifier circuit was built. The first iteration of the circuits can be seen in Fig. 2.2 and contains a PSD at the center, two dual operational amplifiers (dual-OpAmps) and low-pass filters for each of the 4 outputs of the PSD. A bias supply circuit was also added, together with a Bias/GND switch for choosing between connecting the PSD to ground or to a bias voltage. The circuit also contains a temperature sensor and 2 Ethernet ports, one for signal output and the other for power supply. A more detailed look at the circuit schematics can be found in the Appendix.

2.1.6. Circuit Redesign

During the implementation of the metrology system at the telescope, a mounting solution was reached which was not compatible with the initial circuit design. Because of this, a redesign of the PSD circuit was made, which has the detector at the edge of the circuit. The other components of the circuit are also rearranged, and an additional layer of low-pass filters was introduced to further mitigate noise in the lateral displacement measurements. The redesigned circuit boards can be seen in Fig. 2.3, and a complete illustration of the circuit design can be found in the Appendix.

2.2. Testing and Calibrating

2.2.1. Testing the ADC

While setting up the lateral displacement detector unit (Laser+PSD+ADC), it became clear that the ADC introduces a large amount of noise into the measurements. After investigating possible sources and working on optimising the sampling rate, laser beam width and filter options, an uncertainty in the range of 10 to 20 µm was achieved for a sampling rate of 400 samples per second for all 10 channels, or a signal frequency of about 40 Hz for each signal.

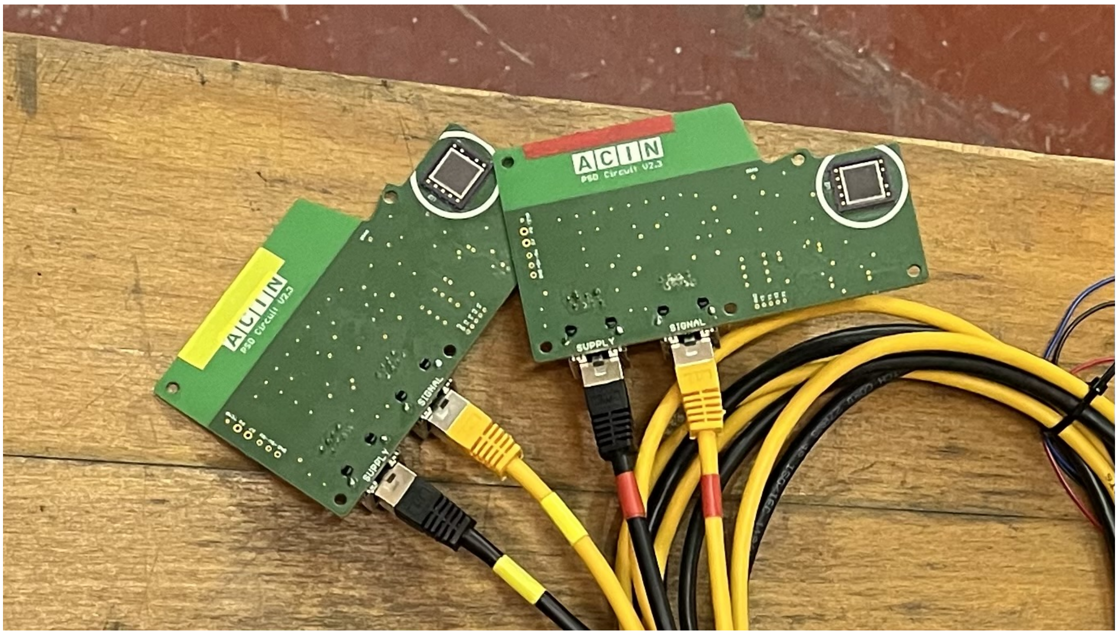

Figure 2.3.: Photograph showing the second iteration of the PSD circuits as it was used at the telescope, including marked Ethernet connections for power (black) and signal (yellow).

2.2.2. Calibrating PSD Detectors

The signal recorded from each PSD circuit contains 4 voltage measurements which can be used to estimate position measurements as shown in Eq. 2.1, where V_{xi} and V_{yi} are the four voltage signals received from the detector circuit, L_x and L_y are the calibration constants and D_x and D_y are the calculated displacements. [18]

$$
\begin{aligned}
D_x &= \frac{L_x}{2} \frac{(V_{x2} + V_{y1}) - (V_{x1} + V_{y2})}{V_{x1} + V_{x2} + V_{y1} + V_{y2}} \\
D_y &= \frac{L_y}{2} \frac{(V_{x2} + V_{y2}) - (V_{x1} + V_{y1})}{V_{x1} + V_{x2} + V_{y1} + V_{y2}}
\end{aligned}
\tag{2.1}
$$

The origin of the measured values is the center of the detector. The calibration constants L_x and L_y set the physical scale of the measurements and can be determined experimentally. Fig. 2.4 shows the laboratory setup used for testing and calibrating the first iteration of the detector circuit by creating a set of calibration curves. It consists of a movable stage with a millimetre measurement and a frame for fixing the laser module. By fixing the PSD circuit to the movable stage and adjusting its position, the beam of the laser can be moved across the detector surface, simulating lateral displacement.

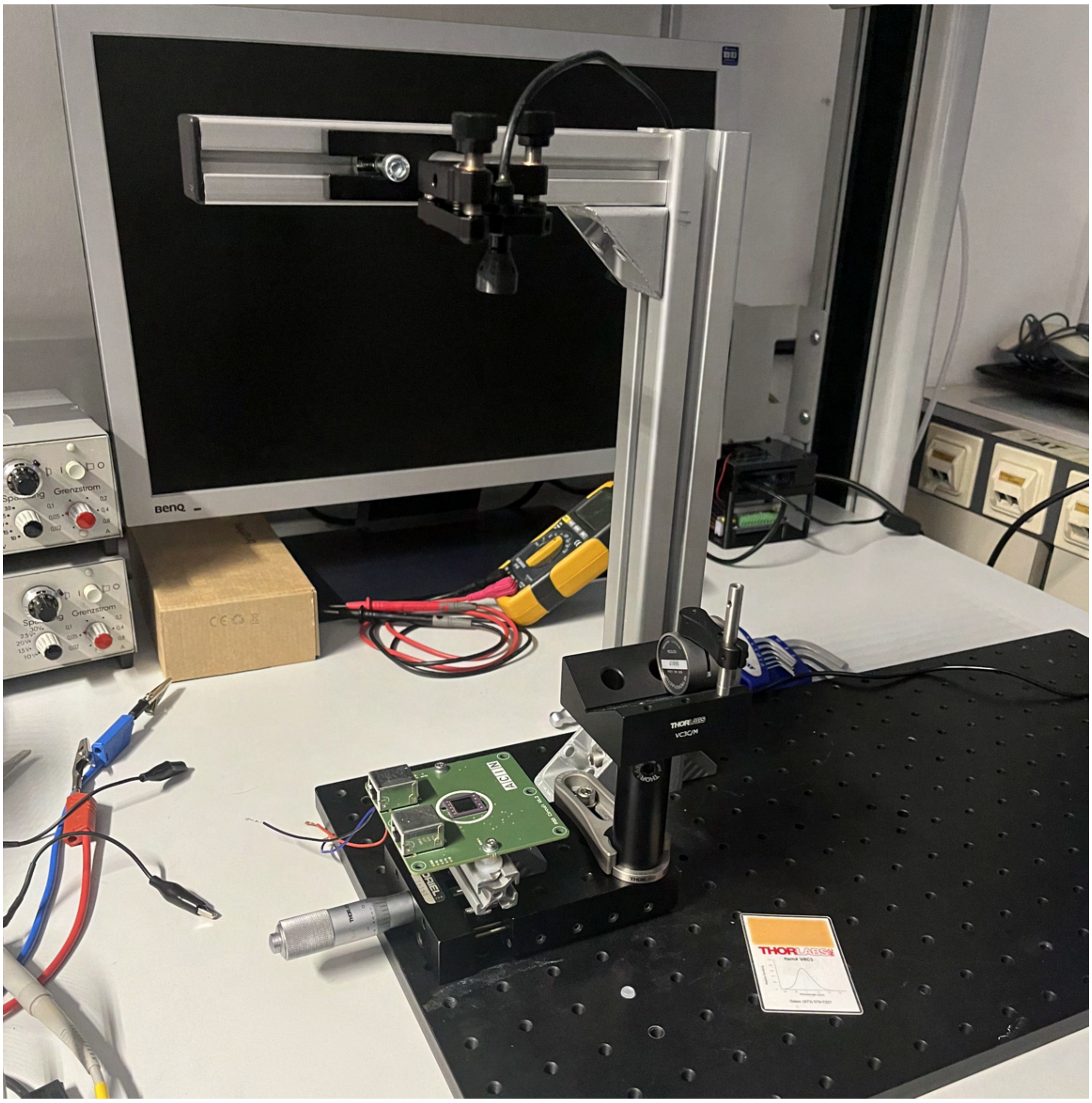

Figure 2.4.: Photograph of the laboratory setup used for testing and calibrating the PSD circuits. The laser pointer is fixed while the detector can be moved using a movable stage with a millimetre scale.

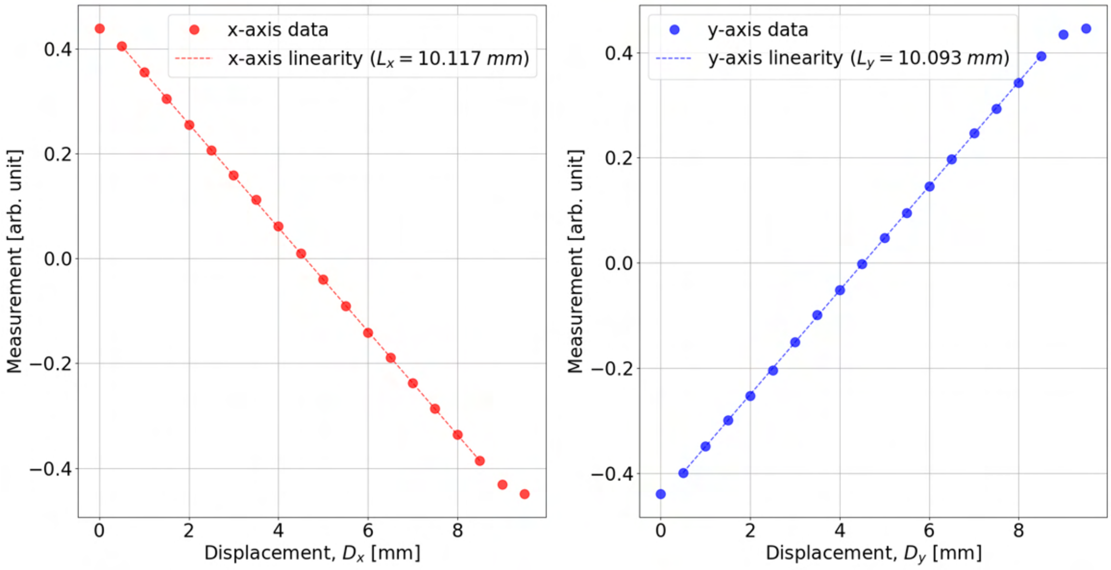

Figure 2.5.: Calibration and linearity test of the PSD circuit, including the x-axis calibration curve (left) and y-axis calibration curve (right). Calibration was realised by setting $L = 1$ and then fitting to make the conversion to mm (or µm). The uncertainties of the manually recorded position measurements are in the range of µm.

2.2.3. Testing the Linearity of the Detectors

A calibration curve is created by setting the calibration constants to $L = 1$ and measuring the estimated displacements as the position of the lateral mount is changed between 0 and 10 mm. Plotting the measured displacement in arbitrary units against the real displacement measured in mm gives the calibration curve of the detector. By rotating the detector 90 degrees and repeating the experiment, two calibration curves are made corresponding to the x and y axes of the detector. Fitting these data points with a linear function reveals the calibration constants L_x and L_y as the slope of the real displacement against the measurement values in arbitrary units. The calibration curves for the x and y-axis of one of the first detector circuits are shown in Fig. 2.5. These measurements were recorded manually, and the estimated precision, according to the calibration constants, is on the order of micrometers. This curve is also useful for testing the linearity of the detector by finding the range in which the detector measures the displacement of the laser beam linearly.

2.2.4. Testing the Detectors under Temperature changes

It's important that temperature changes do not affect the functionality of the detector circuit. Because of this, the circuit has also been tested under varying temperature conditions. In order to test the linearity of the detector at different temperatures, the calibration curve of the detector was repeated with the circuit at room temperature (26°C) and while being heated to 33°C and 50°C respectively. The results of these tests are shown in Fig. 2.6 and reveal no temperature dependence, as the detector maintains the same range of linearity at all three temperatures.

The stability of the detector measurements under temperature changes was also investigated by having the experimental setup in a fixed position (1 mm, 4.5 mm and 8 mm), heating up the circuit board and measuring the temperature and position fluctuations. Measurements were repeated three times for each position, leading to a total of 9 tests, which can be seen in Fig. 2.7. The temperature of the circuit ranged from 23 to 50 degrees, and the position drifts were in the range of 20 to 40 µm. The position data was recorded manually based on the live output of the circuit to the ADC, and its estimated uncertainty is in the range of 10 to 20 µm. As the position drifts and measurement uncertainties are comparable in size, and no consistent trend can be observed across repeated measurements, no temperature dependency can be deduced from these results.

2.2.5. Testing the Detectors with Varying Laser Intensity

Another aspect of the operation of the PSD circuits that was investigated was changing the intensity of the incoming laser beam. This was done by placing a variable density filter between the laser unit and the detector circuit. Adjusting the level of filtering applied to the beam while keeping the laser and the detector fixed allowed the recording of the measured position as the intensity of the beam increased. Fig. 2.8 shows that for attenuations of the laser intensity higher than 40% the measured values deviate rapidly from the reference value, while for lower attenuations the measurement drift remains in a range of 100 µm. Once again, these measurements were recorded manually and have an uncertainty of approximately. 10-20 µm. This indicates some dependency between the sensitivity of the detector and the contrast of the laser beam. This contrast can be decreased either by filtering the incoming beam or increasing the amount of ambient light, making the shielding of the PSD detectors from stray light important for increasing measurement stability.

2.3. Preparation for Telescope Setup

After testing and calibration, the following steps involve integrating the metrology system onto the telescope for measurements. Mounting the equipment as close as possible to the mirror cells is essential for eliminating any other disturbances not caused by the relative motion between the two telescope mirrors. Because of this, a strong inelastic connection to the mirror cells is needed, while also allowing for the adjustment and alignment of the detectors. In order to achieve all of these conditions, prototyping and manufacturing a bespoke mounting solution was necessary. Afterwards, the mounting and alignment of the metrology system took place, followed by measurements and data analysis.

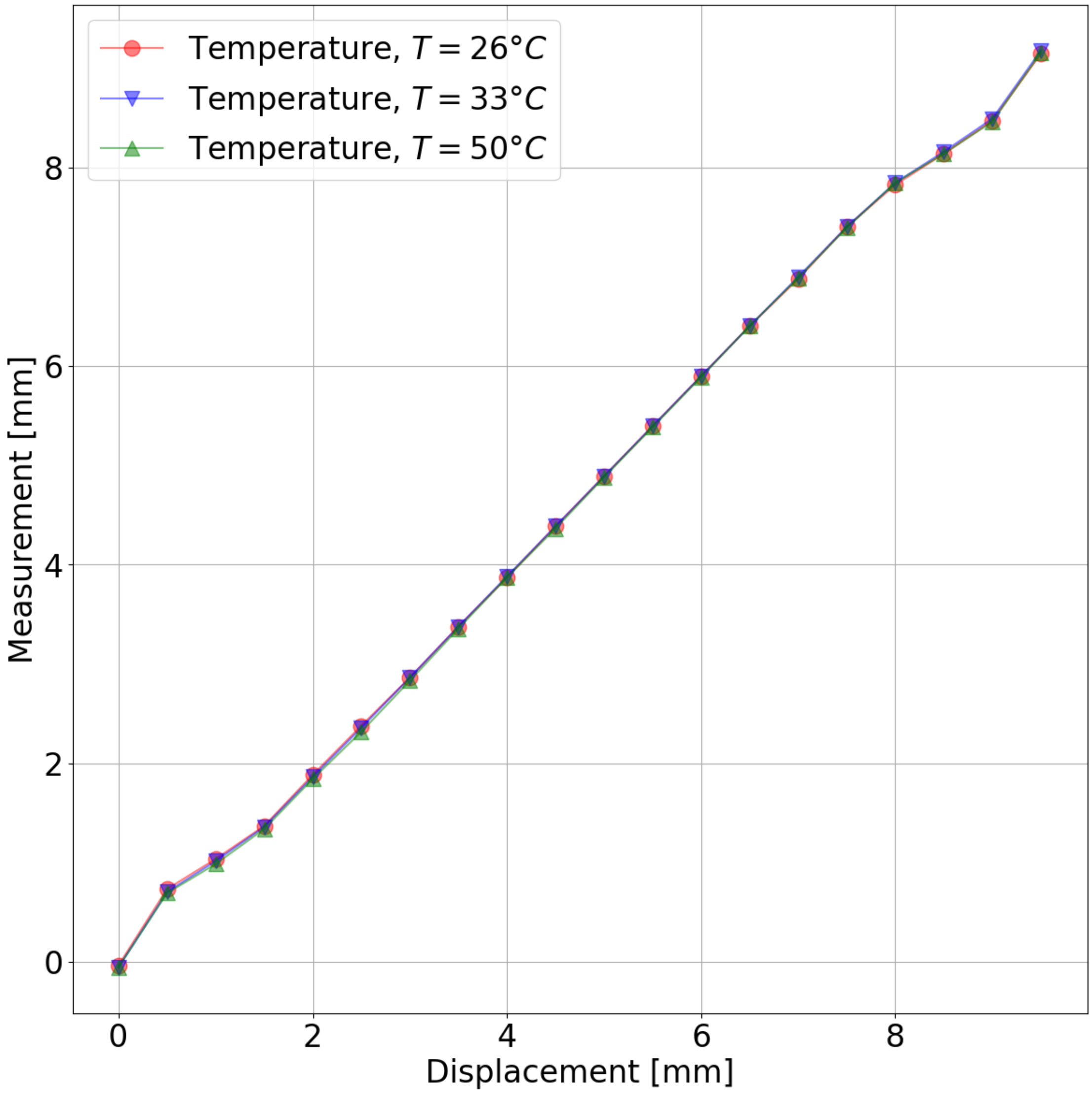

Figure 2.6.: Linearity test for the y-axis of the PSD detector shows no changes in the linearity range with temperature increase. The uncertainties of the manually recorded position measurements are in the range of µm.

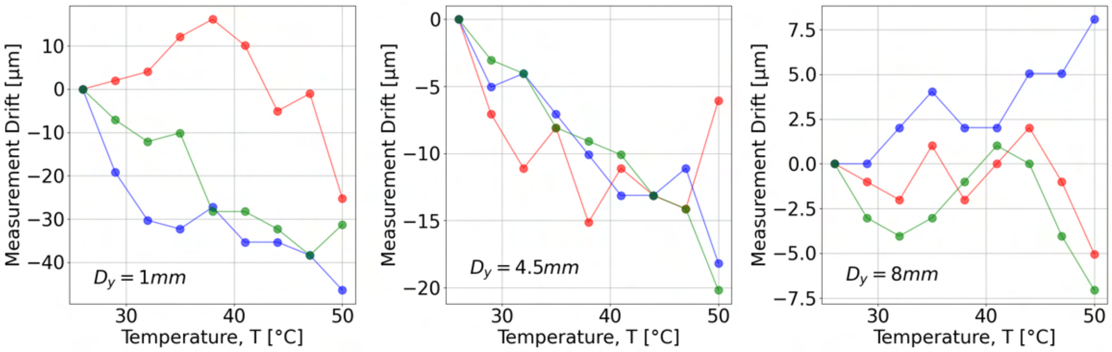

Figure 2.7.: Temperature stability test at varying positions on the detector. Each colour represents a separate set of measurements for a total of 9 (3 for each position). Results show measurement drifts in the range of 20 to 40 µm. The uncertainties of these manually recorded position measurements are in the range of 10-20 µm.

2.3.1. Mounting Strategy

After several runs of prototyping, a mounting solution was reached consisting of an adapter ring mounted onto the primary mirror cell, which can hold two PSD detectors (with their redesigned circuits) and three interferometer heads. The PSD detectors are fixed and at an angle of 90°. The interferometer heads are attached to kinetic mounts, which allow fine adjustments for alignment purposes. The secondary mirror adapter consists of a fixed housing for the interferometer's retroreflectors, as well as a mounting place for the laser units used in the lateral displacement detector unit. The final adapters were manufactured out of aluminium and can be seen mounted in Fig. 2.9.

2.3.2. Setup and Alignment

The setup of the adapter mounts and metrology system was done over several visits to the telescope. The mounting of the interferometer system was done using software incorporated in the interface of the interferometer. The device also contains a visible pilot laser that enables easier alignment without the need for additional equipment. The PSD detector system, however, required more attention when aligning. The laser used for the PSD measurements operates in the infrared range, and there is no additional alignment laser. Because of this, an infrared camera was necessary in order to align the laser pointer with the PSD detectors on the primary mirror cell. Fine adjustments were possible using the interface of the Raspberry Pi in order to visualise the live detector feedback. This process is pictured in Fig. 2.10.

The various components of the metrology system and their mounting on the telescope structure are represented in Fig. 2.11. In order to integrate all of the different detectors into one measurement system, all measurements obtained were projected onto a common

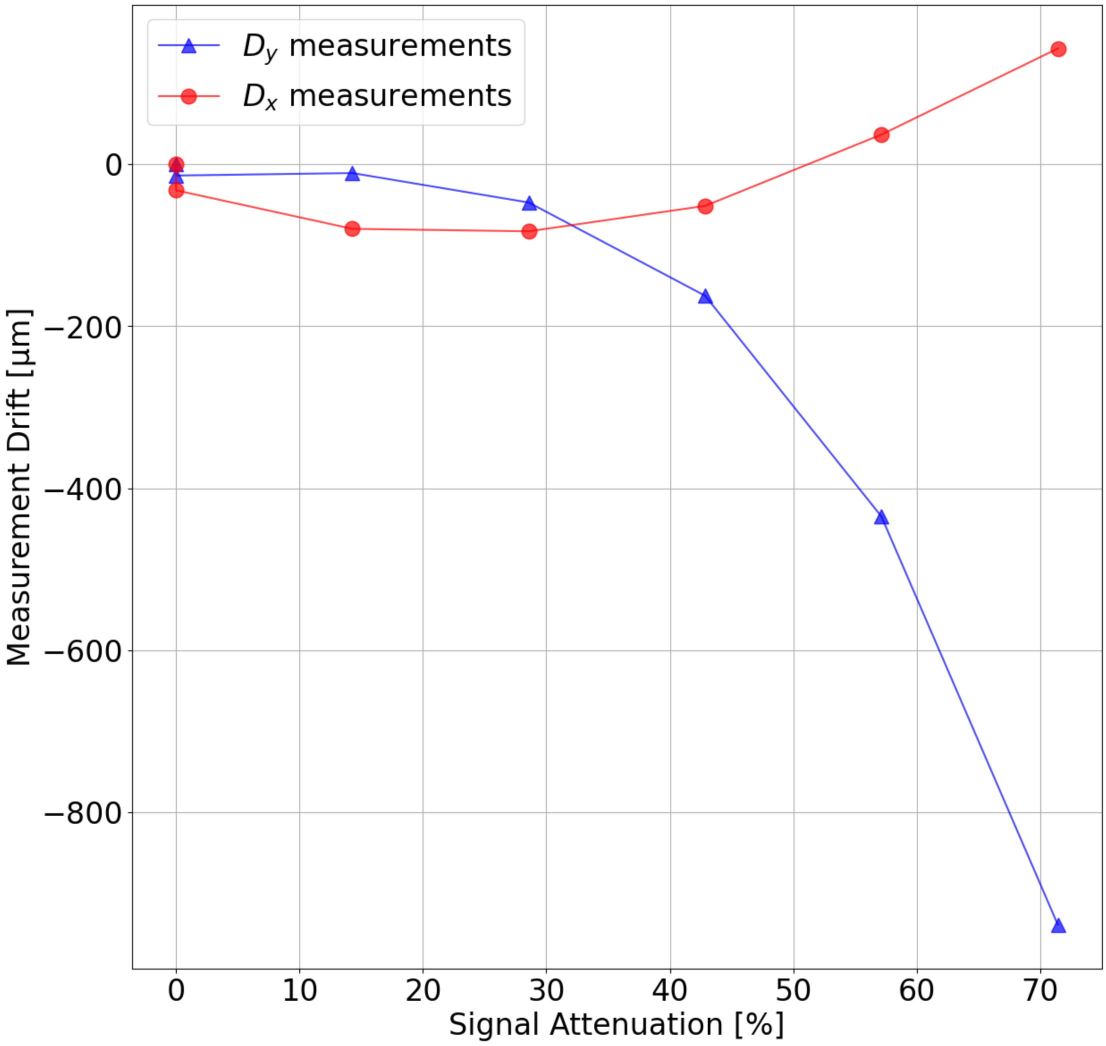

Figure 2.8.: Signal strength dependent stability test for x(red) and y(blue)-axis. Results show drifts of up to 100 µm with attenuations of up to 40% and up to 1 mm for higher attenuation. The uncertainties of these manually recorded position measurements are in the range of 10-20 µm.

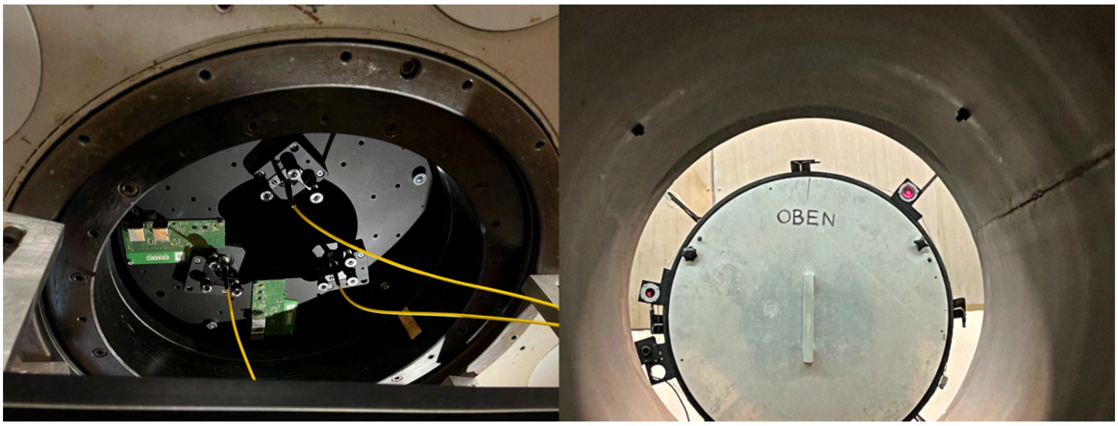

Figure 2.9.: Mounting solutions for the metrology system implemented on the 1.5m LFOA telescope showing the primary mirror mounting ring (left) and secondary mirror mounting modules (right).

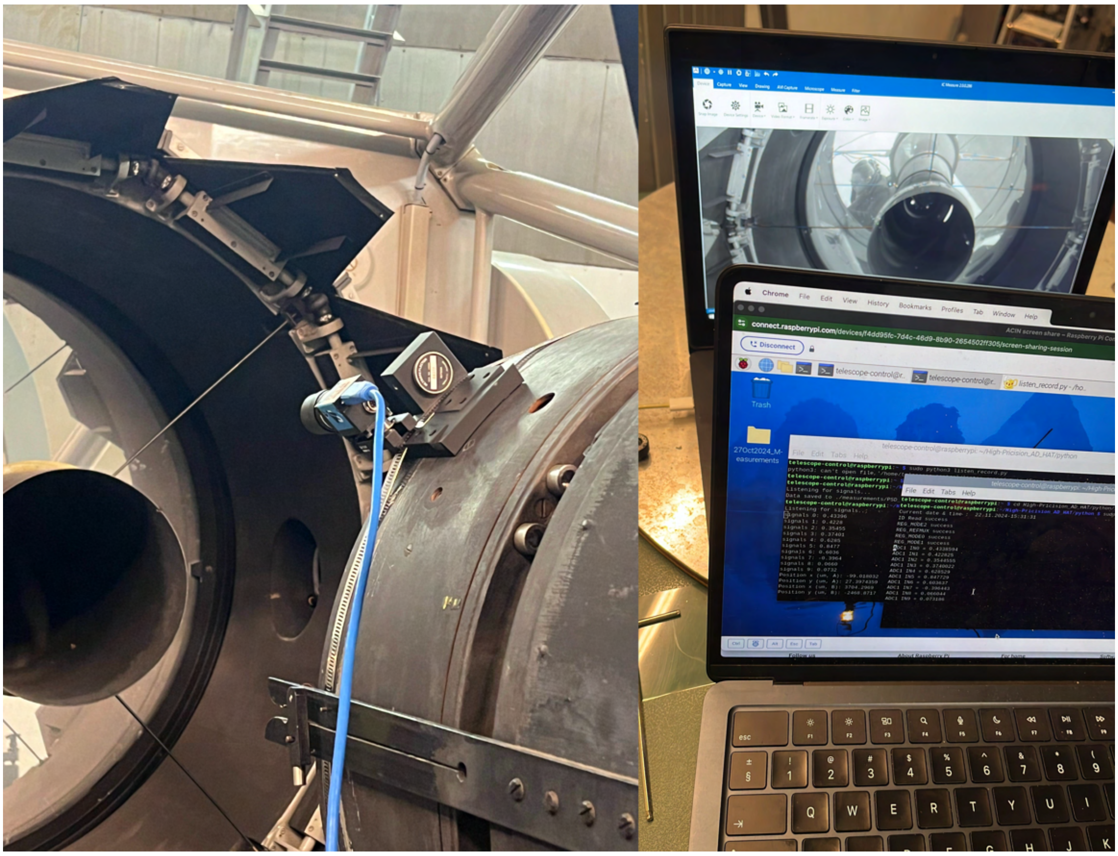

Figure 2.10.: Alignment process for the PSD detectors and laser unit combo showing the Infrared camera (left) used for the rough positioning of the laser spot and the computer setup (right) used for precise alignment.

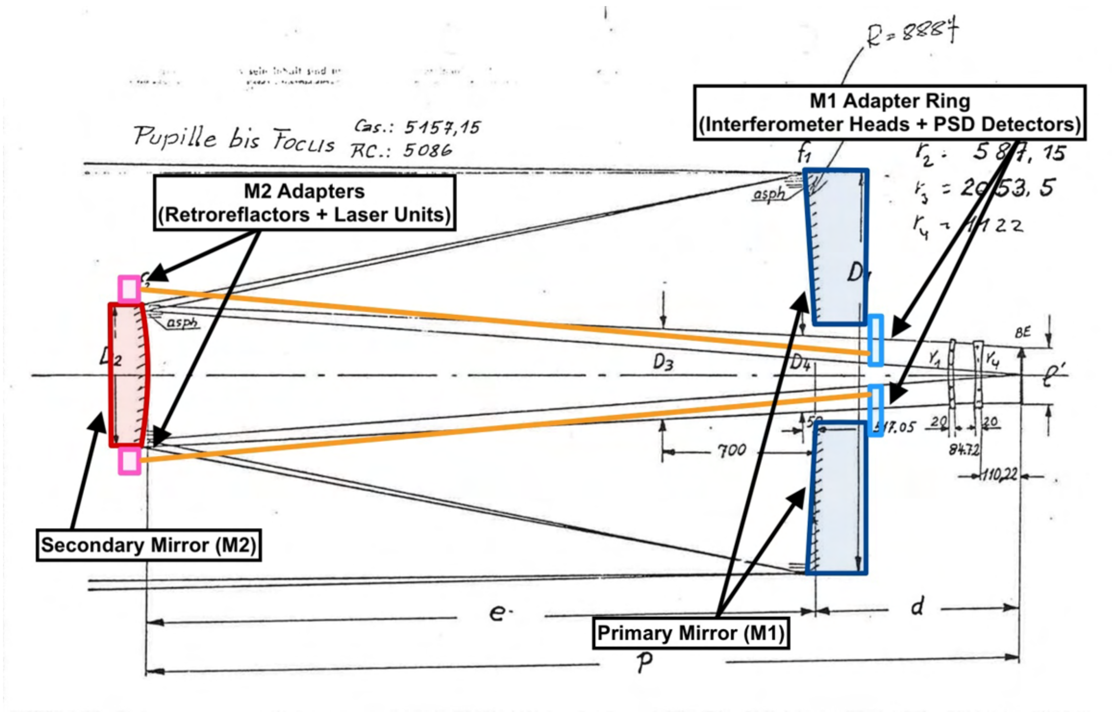

Figure 2.11.: Diagram of the metrology system installed on the 1.5m LFOA telescope showing the primary and secondary mirrors along with equipment adapters and their positions.

frame of reference chosen as follows: the Y-axis is along the Declination coordinate while the X-axis is along the RA coordinate, tip is the rotation around the X-axis while tilt is the rotation along the Y-axis and the axial defocus remains the distance between the two mirrors. Since all of the detectors are offset to some degree from this frame of reference, a set of conversion matrices were calculated based on the mapped positions of all of the detectors. Applying these transformations to the measured data allows all observables to be more easily compared and interpreted. All results are stated in terms of this common frame of reference. With the metrology system aligned and operational, measurements took place and the resulting data was analysed in order to characterise the opto-mechanical behaviour of the 1.5m LFOA.

3. Results and Discussion

3.1. Preliminary measurements

A preliminary set of measurements was taken while the telescope was in operation. Measurements were taken separately with the interferometer and the PSD and covered a range of telescope positions towards east, west and along the meridian. All of these measurements and their metadata are shown in Table 3.1.

The interferometer measurements were taken first and investigated a range of telescope positions with two pointing east, with a negative hour angle (HA$<$0), another two pointing west, with a positive hour angle (HA$>$0), and the rest pointing along the meridian (HA=0). These measurements were taken with the telescope either pointing or tracking. While pointing, the telescope was static and remained at its initial pointing coordinates, and while tracking, the telescope follows the rotation of the Earth at a rate of 0.25 degrees per minute, essentially pointing at the same region of sky. The recording duration also differed between measurements. For the interferometer measurements, a duration of 10 minutes was used for static measurements and 15 minutes for the tracking ones. The interferometer measurements were taken in two separate batches of 8 and 12 measurements respectively. Since the instrument was realigned between measurements, the results need to be analysed separately in order to calculate the displacement of each metric from their observed mean values. These first interferometer measurements were taken collaboratively as part of an adjacent master project by Florian Kreuzmair from TU Wien. [19]

The lateral position "PSD" measurements were taken next and were realised in such a way as to investigate the same positions as the previously taken interferometer measurements. For the first batch of PSD measurements, the same tracking modes and recording times were used, resulting in 11 measurements. A second batch of 3 PSD measurements was taken. Due to time constraints, this batch focused on recording the telescope tracking while crossing the meridian in order to investigate shifts in mirror positions caused by the weight shifts in the structure of the telescope. These measurements were recorded for 20 minutes each.

3.1.1. Interferometer measurement analysis

An analysis of the individual interferometer measurements was made, and for each one, a set of plots was created. Fig. 3.1 shows the plotsheet created for observation No.1 from

Obs. No.	Date and Detector	HA (degrees)	Dec (degrees)	Duration (min)	Mode
1	5.Nov.24 - IF	0	48	10	static
2	5.Nov.24 - IF	-30	-15	10	static
3	5.Nov.24 - IF	-30	0	10	static
4	5.Nov.24 - IF	0	0	10	static
5	5.Nov.24 - IF	0	-32	10	static
6	5.Nov.24 - IF	80	30	10	static
7	5.Nov.24 - IF	50	50	10	static
8	5.Nov.24 - IF	0	0	15	tracking
1	15.Nov.24 - IF	0	30	10	static
2	15.Nov.24 - IF	0	48	10	static
3	15.Nov.24 - IF	0	0	10	static
4	15.Nov.24 - IF	0	-32	10	static
5	15.Nov.24 - IF	0	-20	15	tracking
6	15.Nov.24 - IF	-30	-15	10	static
7	15.Nov.24 - IF	-30	0	15	tracking
8	15.Nov.24 - IF	50	50	15	tracking
9	15.Nov.24 - IF	0	90	10	static
10	15.Nov.24 - IF	80	30	10	static
11	15.Nov.24 - IF	0	90	15	tracking
12	15.Nov.24 - IF	0	48	10	static
1	22.Nov.24 - PSD	0	30	10	static
2	22.Nov.24 - PSD	0	30	15	tracking
3	22.Nov.24 - PSD	0	48	10	static
4	22.Nov.24 - PSD	0	0	10	static
5	22.Nov.24 - PSD	0	-32	10	static
6	22.Nov.24 - PSD	0	-20	15	tracking
7	22.Nov.24 - PSD	-30	-15	10	static
8	22.Nov.24 - PSD	-30	0	15	tracking
9	22.Nov.24 - PSD	50	50	15	tracking
10	22.Nov.24 - PSD	80	30	10	static
11	22.Nov.24 - PSD	0	90	10	static
1	30.Jan.25 - PSD	-0.16	0	20	tracking
2	30.Jan.25 - PSD	-0.16	30	20	tracking
3	30.Jan.25 - PSD	-0.16	48	20	tracking

Table 3.1.: Metadata for the preliminary measurements taken between Nov 5 2024, and Jan 30 2025.

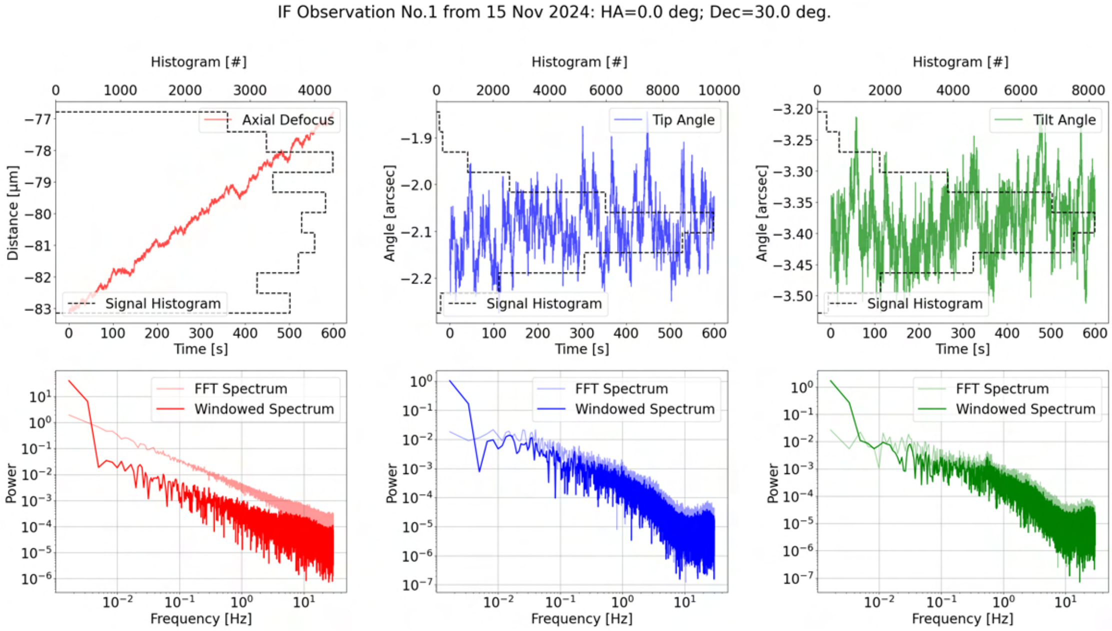

Figure 3.1.: Example Plotsheet of interferometer measurement no.1 from Nov 15. The top row includes the time-series data of the recorded displacements together with their respective histograms. The bottom row includes Fourier analysis of the recorded signals, windowed with a Blackman window.

Nov 15 2024. The first row of plots in this figure shows the time-series data of the axial distance, tip angle and tilt angle displacements. On top of the recorded data, a histogram of the measured values is also plotted. The axial displacement measurement shows a steady increase in the distance between the two mirrors of around 6 µm, while the tip and tilt angle measurements show fluctuations in the range of 0.03 arcsec. The histograms of the measured data show that the distribution of values for the tip and tilt measurements resembles a Gaussian distribution, meaning that the measurements can be summarised by a mean with an uncertainty given in the form of standard deviation. The signal histogram for the axial displacements does not resemble a Gaussian but rather a flat distribution within the measured range. Because of this, the defocus measurement will be expressed as the mean value with an uncertainty within the minimum and maximum observed values in the individual measurements. The second row of plots in Fig. 3.1 shows a Fourier analysis of the time-series data recorded during each measurement. A Blackman window function is also applied to the signals in order to reduce spectral leakage arising from the non-periodicity of these measurements. No high frequency components, such as structural vibrations, have been found as a result of this analysis, suggesting stable operation within individual measurements.

Analysing the other measurements in this fashion reveals comparable results; therefore, the data was summarised and can be found in Table 3.2. This table includes all measure-

#	Date	HA (degrees)	Dec (degrees)	Axial Defocus (µm)	Tip Rotation (arcsec)	Tilt Rotation (arcsec)
1	5.Nov.24	0.0	48.0	-57.3 ± 4.1	-14.32 ± 2.67	0.52 ± 1.38
2	5.Nov.24	-30.0	-15.0	17.7 ± 1.0	6.49 ± 0.04	-6.22 ± 0.04
3	5.Nov.24	-30.0	0.0	0.2 ± 0.8	2.63 ± 0.05	-7.15 ± 0.05
4	5.Nov.24	0.0	0.0	-6.0 ± 0.6	3.0 ± 0.05	-3.19 ± 0.05
5	5.Nov.24	0.0	-32.0	43.9 ± 1.8	11.1 ± 0.06	-0.92 ± 0.04
6	5.Nov.24	80.0	30.0	16.1 ± 3.6	1.53 ± 0.05	9.19 ± 0.11
7	5.Nov.24	50.0	50.0	-14.7 ± 1.3	-10.44 ± 0.05	7.77 ± 0.04
8	5.Nov.24	0.0	0.0	3.5 ± 2.0	3.15 ± 0.05	-1.73 ± 0.11
1	15.Nov.24	0.0	30.0	-80.0 ± 3.2	-2.09 ± 0.06	-3.38 ± 0.05
2	15.Nov.24	0.0	47.0	-79.7 ± 2.6	-8.32 ± 0.1	-2.82 ± 0.1
3	15.Nov.24	0.0	0.0	-38.4 ± 2.6	8.59 ± 0.05	-4.7 ± 0.04
4	15.Nov.24	0.0	-32.0	39.1 ± 3.0	16.67 ± 0.11	-0.43 ± 0.04
5	15.Nov.24	0.0	-20.0	37.2 ± 3.2	14.73 ± 0.05	-0.64 ± 0.11
6	15.Nov.24	-30.0	-15.0	42.0 ± 2.5	13.11 ± 0.03	-4.37 ± 0.05
7	15.Nov.24	-30.0	0.0	30.3 ± 11.1	9.25 ± 0.6	-4.79 ± 3.09
8	15.Nov.24	50.0	50.0	6.2 ± 3.6	-3.73 ± 0.08	6.52 ± 0.08
9	15.Nov.24	0.0	90.0	-11.9 ± 1.5	-22.39 ± 0.07	3.33 ± 0.05
10	15.Nov.24	80.0	30.0	44.2 ± 3.7	7.22 ± 0.11	6.64 ± 0.13
11	15.Nov.24	0.0	90.0	6.8 ± 1.4	-22.43 ± 0.12	5.63 ± 0.08
12	15.Nov.24	0.0	48.0	4.4 ± 1.3	-10.61 ± 0.04	-1.0 ± 0.05

Table 3.2.: Results from the preliminary interferometer measurements.

ments taken with the interferometers, namely axial defocus, tip and tilt rotation, along with the initial telescope position for each measurement and the Measurement number and date.

In order to better visualise this data, the mean displacements are shown in context with telescope positions by plotting each measurement as circles with coordinates given by the target coordinates of the telescope. The size of circles in these plots corresponds to the absolute values of the displacements, and their colours, blue or red, correspond to negative or positive displacements respectively. This was done separately for the axial, tip and tilt displacements and can be seen in Fig. 3.2. Noting that the zenith, with coordinates HA of 0 and Dec of approx. 48 degrees, is the highest point for the secondary mirror and moving away from this implies the secondary mirror getting closer to the horizon.

From the axial defocus plot in Fig. 3.2, it can be seen that the axial distance is subjected to a negative displacement when the telescope is pointing upwards near zenith, and changes towards positive displacement as the telescope moves closer to the horizon. The tip rotation measurements display a trend of increasing negative displacements when

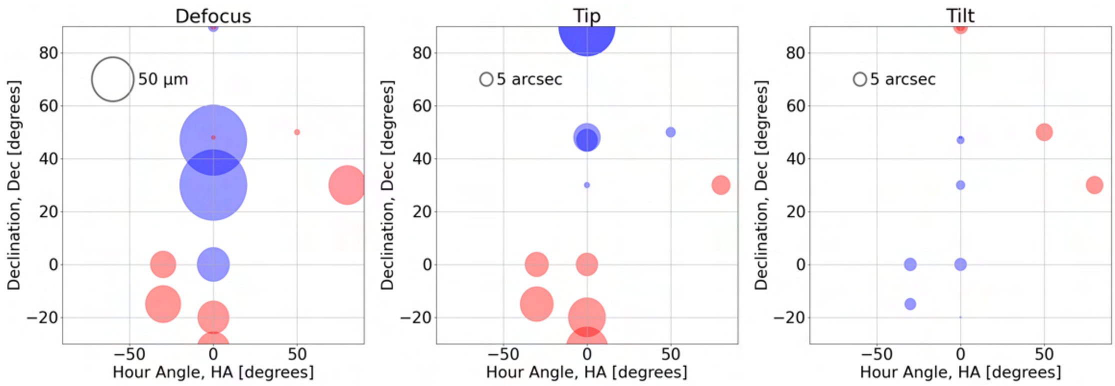

Figure 3.2.: Bubble plots of the preliminary interferometer measurements. Bubble size represents displacement amount, and the empty bubbles provide size reference. The measurement bubbles are coloured red for positive displacement and blue for negative.

the declination, Dec, is higher than the zenith declination, or in other words, when the telescope is pointing north. With the telescope pointing south, increasing positive displacements can be observed. Similarly, the tilt rotation displacements show a trend that is hour angle, HA, dependent, with negative values towards east and positive values towards west. All of these trends indicate a strong gravitational dependency of the displacements between the primary and secondary mirrors measured by the interferometer.

3.1.2. PSD measurement analysis

Similarly to the interferometer investigations, an analysis of the individual PSD measurements was made, and a set of plots was created. A sample of these plots is shown in Fig. 3.3 for the first measurement from Nov 22nd 2024. Due to alignment issues, one of the detectors was not used in the preliminary measurements, and so the available data is the X and Y-axis displacements measured with detector A.

Consistent with the interferometer measurements, these plots show time-series data recorded and its Fourier power spectrum. The first row of plots corresponds to the X-axis while the second corresponds to the Y-axis measurements. The plots on the left side show the recorded data, a moving average applied to the signal with a window of 100 samples and a histogram of the recorded data, showing a Gaussian distribution for both measured variables. The left side plots show the power spectrum of this data. This Fourier analysis reveals more noise compared to the interferometer measurements; however, still no significant high frequency contribution to the measured displacements.

As with the interferometer data, the other measurements taken with the PSD detector behave similarly to the displayed example. Because of this, the data has been summarised

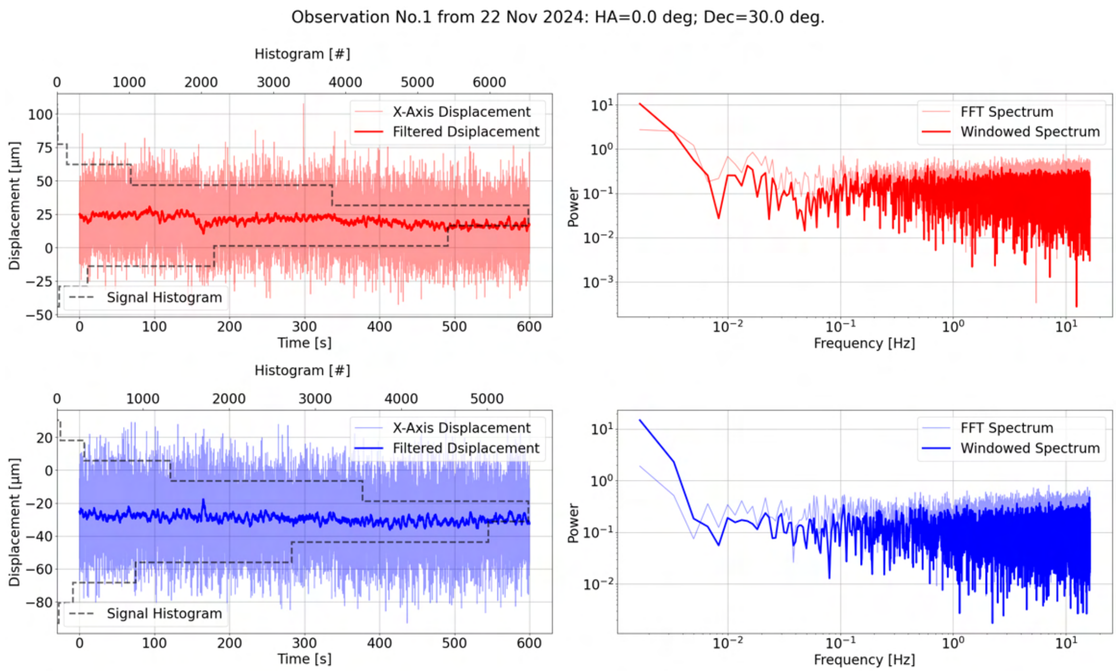

Figure 3.3.: Example plotsheet of the first PSD measurements from Nov 22. The left column includes the time-series data of the recorded displacements, together with their respective histograms and the filtered signal. The right column includes Fourier analysis of the recorded signals, windowed with a Blackman window.

Obs. No.	Date	HA (degrees)	Dec (degrees)	X Displacement (µm)	Y Displacement (µm)
1	22.Nov.24	0	30	20.4 ± 17	-29.5 ± 17
2	22.Nov.24	0	30	17.2 ± 17	-32.2 ± 17
3	22.Nov.24	0	48	7.1 ± 17	-128.7 ± 17
4	22.Nov.24	0	0	17.4 ± 17	75.6 ± 16
5	22.Nov.24	0	-32	34.5 ± 18	163.7 ± 17
6	22.Nov.24	0	-20	22.1 ± 18	132.0 ± 17
7	22.Nov.24	-30	-15	98.3 ± 19	120.3 ± 18
8	22.Nov.24	-30	0	81.3 ± 20	64.8 ± 18
9	22.Nov.24	50	50	-89.0 ± 17	-101.2 ± 17
10	22.Nov.24	80	30	-130.1 ± 17	31.2 ± 17
11	22.Nov.24	0	90	-79.1 ± 20	-296.1 ± 20
1	30.Jan.25	-0.16	0	1.8 ± 7	2.4 ± 8
2	30.Jan.25	-0.16	30	-0.2 ± 7	-0.1 ± 8
3	30.Jan.25	-0.16	48	-1.6 ± 7	-2.2 ± 8

Table 3.3.: Results from the preliminary lateral position PSD measurements.

by the mean of each measurement in X and Y respectively, with the uncertainty estimated as the standard deviation of the mean for each measurement. The summary of the data is shown in Table 3.3.

Using the bubble plots to visualise these deviations as a function of telescope position reveals similar results to the interferometer analysis. Fig. 3.4 shows the relative displacement in X (left) and Y (right) as a function of telescope position. Once again, the magnitude of the bubbles represents the absolute deviation, while their colour indicates positive (red) or negative (blue) displacement. Similarly to the interferometer results, the X-axis displacements reveal a stronger HA dependency, with positive displacements towards east and negative displacements towards west. A declination dependence can also be seen with lower deviations when the telescope is pointing closer to zenith. The Y-axis deviations show strong declination dependence, with positive displacements towards south and negative displacements towards north, while also displaying the same trend for lower absolute displacements towards zenith. As with the interferometer results, these trends indicate strong gravitational influences on the relative lateral displacement between the two mirrors.

Another way to visualise the PSD data is by mapping the mean PSD measurements and their uncertainty on the surface of the detector. Fig. 3.5 displays the relative positions of the secondary mirror with respect to the primary one as they would have been detected at the surface of the detector. The datapoints are adjusted for the frame of reference used to display these results. A summary of these measurements is given as the expected deviation in X or Y, calculated as the standard deviation of the measured datapoints to

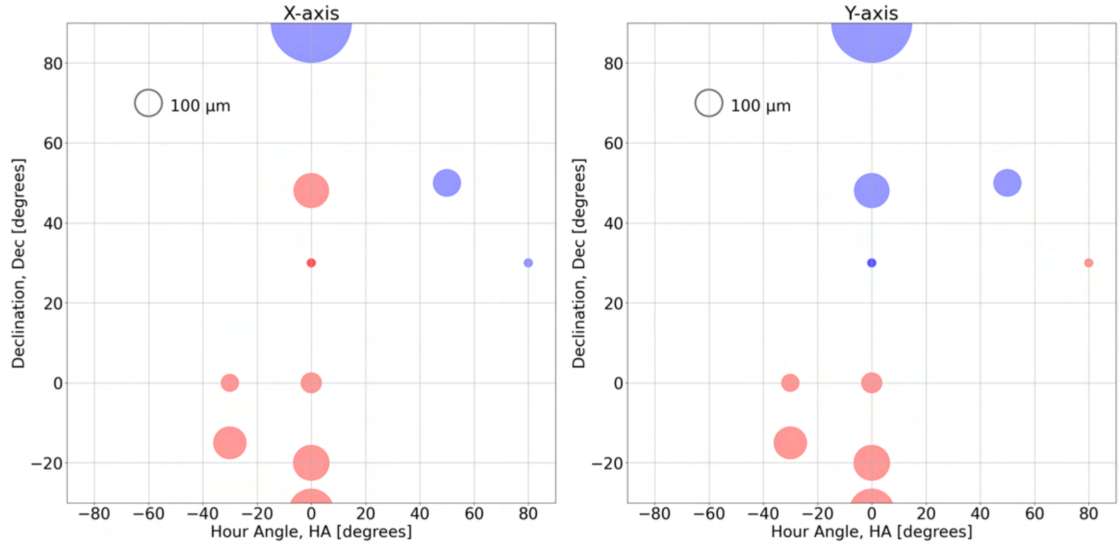

Figure 3.4.: Bubble plots of the preliminary PSD measurements. Bubble size represents displacement amount, and the empty bubbles provide size reference. The measurement bubbles are coloured red for positive displacement and blue for negative.

be in the order of 100 µm, explicitly 70.8 µm and 136 µm for the X and Y-axis respectively. This is illustrated on the map as an ellipse with dimensions given by these expected deviations. Once again, the trend showcased by this plot indicated much larger deviations along the Y-axis than the X-axis, almost twice as large, which is consistent with the previously indicated gravitationally induced deviations.

Regarding the three measurements taken on January 30 2025, with the PSD detector. These measurements were few, and since the telescope did not move considerably between positions, they do not show the same degree of deviations as with the previous measurements. This could indicate that with lighter use, when the telescope is not moved at wide extremes over short periods of time, the effects of lateral displacement are not as strong; however does not fully rule out the misalignment of the two mirrors. Another consequence of these few measurements is that they cannot be easily placed together with the measurements from the previous batch to obtain an estimated deviation.

3.1.3. Discussions

Using the measurements gathered so far, one can estimate a set of expected deviations for each of the measured degrees of freedom. This was calculated as the standard deviation of the measurements taken for each variable individually, within each separate batch of results and from each detector. All together, this provides two estimates for

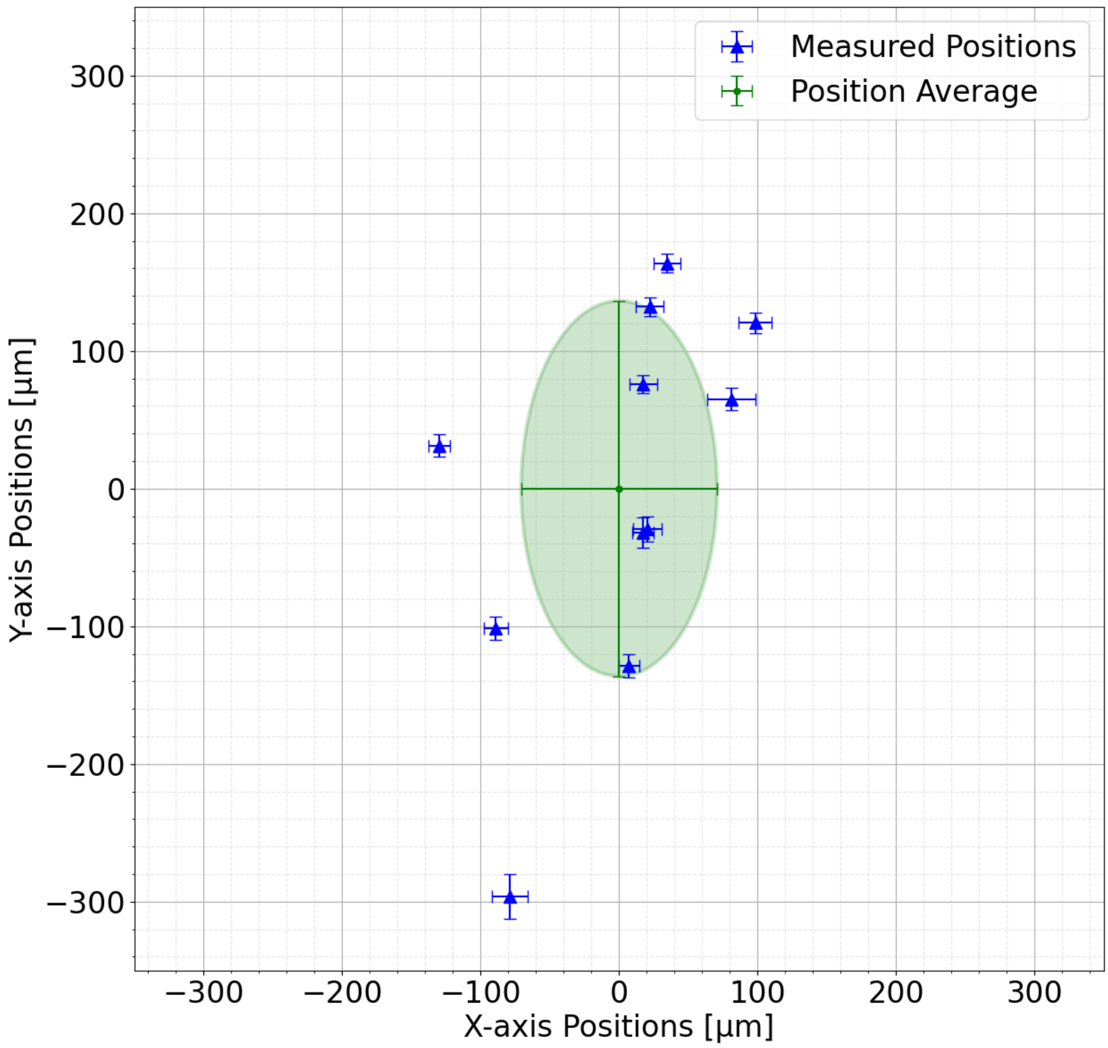

Figure 3.5.: Map of the measured positions from the preliminary measurements on Nov 22. The blue scatter represents the measured relative positions, and the green surface represents the range of expected displacements estimated as the standard deviation of the blue scatter.

Obs. Date and Detector	Observed Value	Expected Deviation	Maximum Observed Deviation
5.Nov.24 - IF	Axial Defocus (µm)	31.7	57.2
	Tip Rotation (arcsec)	9.1	14.3
	Tilt Rotation (arcsec)	6.4	9.2
15.Nov.24 - IF	Axial Defocus (µm)	46.9	79.6
	Tip Rotation (arcsec)	14.0	23.4
	Tilt Rotation (arcsec)	4.6	6.55
22.Nov.24 - PSD	X Displacement (µm)	70.8	130.1
	Y Displacement (µm)	136.4	296.1
30.Jan.25 - PSD	X Displacement (µm)	1.41	1.8
	Y Displacement (µm)	1.87	2.37

Table 3.4.: Summary of the preliminary measurements.

each of the degrees of freedom measured by the interferometer, and one estimate for each of the PSD degrees of freedom. Additionally, for each expected displacement, a worst case displacement was also estimated as the absolute deviation from the mean of each batch of results. The expected and worst case displacements are shown in Table 3.4.

Together, these values can be used to investigate the impact on image quality caused by the relative motion between the secondary and primary mirror. However, to improve available data, a new set of measurements was planned. With these additional measurements, more relevant scenarios were investigated, making use of our current knowledge of the telescope's behaviour. Additionally, for the following measurements, all detectors (two PSDs and one interferometer) could be used simultaneously, giving a more complete view of the investigation.

3.2. Additional measurements

An additional set of measurements was taken on February 21 2025, as previously mentioned. Over the course of this investigation, the telescope was pointed in ten positions of interest. The observations began and ended with the telescope pointing towards the north star, in order to compare the telescope behaviour when returning to roughly the same position on the sky. The following four positions investigate the telescope's behaviour when pointing in either east or west directions while being closed or higher with respect to the horizon. The last four positions before ending on the north star investigate the behaviour of the telescope crossing the meridian, as was done in the last PSD observations. All of the initial telescope positions and measurement durations are displayed in Table 3.5. For additional visual context, a collage of the telescope positions for each of the 10 measurements can be seen in Fig. 3.6.

Figure 3.6.: Photographs of the telescope positions as reported in Table 3.5.

Since in the preliminary measurements, pointing and tracking did not show much of a difference, and since the telescope is expected to be operated while tracking astronomical objects, all of the measurements in this additional investigation were performed with the telescope in tracking mode, with most measurements lasting 10 minuted, with for the four meridian measurements which lasted 20 minutes, 10 minutes on each side of the meridian. An analysis of the interferometer and PSD data was made similarly to the preliminary measurements by creating plot sheets for each individual observation. Since these results are consistent with the preliminary ones, the same method of analysis has been applied. The plotsheets from the secondary set of measurements can be found in the Appendix. The summary of these results, along with additional information such as measurement duration and telescope position, is shown in Table 3.5.

3.2.1. Interferometer measurement analysis

The first set of data shown in Table 3.5 are the interferometer measurements. Each observation summary gives an axial displacement measured in µm, followed by tip and tilt displacements, in that order, measured in arcsec. Just as for the preliminary results, the axial displacement is given as a mean of the recorded data, with uncertainties expressed as the interval of the recorded slope. The tip and tilt displacement results are simply given as the mean and standard deviation of the recorded data, which was shown to resemble a Gaussian distribution.

A way to visualise the data as a function of telescope positions is once again given in the form of bubble plots in Fig. 3.7. The same trends as before are once again present. Axial displacement is most negative while the telescope is pointing up and most positive

Obs. No.	HA (hours)	Dec (degrees)	Duration (minutes)	Interferometer Measurements (µm, as, as)	PSD Detector A Measurements (µm, µm)	PSD Detector B Measurements (µm, µm)
1	0.93	89.37	10	10.1 ± 1.3 -16.52 ± 0.04 2.3 ± 0.1	-34.6 ± 15.5 -186.9 ± 18.7	-29.2 ± 15.5 -219.1 ± 18.7
2	-4.42	19.58	10	43.8 ± 2.2 9.83 ± 0.04 -8.51 ± 0.04	125.9 ± 16.1 103.9 ± 17.3	111.4 ± 16.1 83.3 ± 17.3
3	-1.48	6.02	10	-4.4 ± 1.5 -1.94 ± 0.07 -5.69 ± 0.08	66.2 ± 15.9 -10.9 ± 16.1	90.0 ± 15.9 -17.4 ± 16.1
4	2.7	42.45	10	-1.0 ± 0.9 1.25 ± 0.11 3.24 ± 0.13	-45.2 ± 15.3 10.8 ± 15.6	-35.8 ± 15.3 -1.2 ± 15.6
5	4.77	15.33	10	51.9 ± 0.3 14.31 ± 0.14 8.66 ± 0.07	-90.7 ± 14.5 119.7 ± 16.4	-134.6 ± 14.5 144.2 ± 16.4
6	-0.17	0.0	20	14.9 ± 2.6 13.12 ± 0.03 -2.01 ± 0.08	22.7 ± 15.0 127.2 ± 17.4	19.7 ± 15.0 142.4 ± 17.4
7	-0.17	30.0	20	-19.1 ± 2.5 3.68 ± 0.04 -3.56 ± 0.1	28.9 ± 15.3 46.3 ± 17.2	39.2 ± 15.3 74.3 ± 17.2
8	-0.16	48.08	20	-31.5 ± 1.8 -3.34 ± 0.04 -2.3 ± 0.14	17.1 ± 15.6 -21.2 ± 17.6	36.5 ± 15.6 -14.9 ± 17.6
9	-0.17	66.0	20	-39.4 ± 1.4 -9.78 ± 0.06 -0.55 ± 0.14	2.4 ± 15.6 -83.8 ± 15.9	21.8 ± 15.6 -92.1 ± 15.9
10	3.83	89.37	10	-25.4 ± 0.8 -10.62 ± 0.15 8.42 ± 0.06	-92.8 ± 15.1 -105.2 ± 16.7	-119.0 ± 15.1 -99.6 ± 16.7

Table 3.5.: Metadata and results from the secondary measurements.

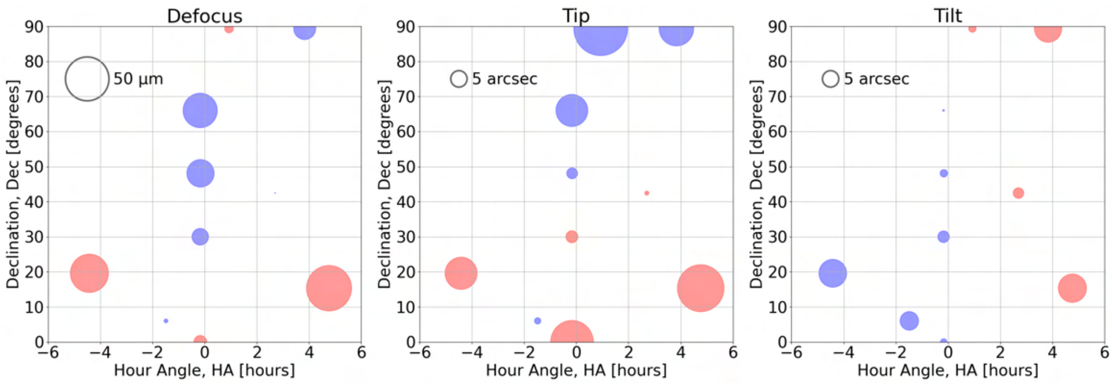

Figure 3.7.: Bubble plots of the secondary interferometer measurements. Bubble size represents displacement amount, and the empty bubbles provide size reference. The measurement bubbles are coloured red for positive displacement and blue for negative.

while close to the horizon. Tip angular displacement is growing negatively as the telescope is pointing north of zenith and growing positively when pointing south of zenith. And finally tilt angular displacement grows negatively while pointing east and grows positively while pointing west.

3.2.2. PSD measurement analysis

The next results shown in 3.5 are the results from PSD detectors A and B. Each column gives the X and Y-axis displacements respectively, measured in µm. Since the data recorded by the two detectors also matches a Gaussian distribution, it was summarised as a mean with standard deviation, like in the preliminary results. The positions measured by the two detectors were projected onto the same frame of reference in order to facilitate comparing the two detectors points of view. By calculating the difference between the two detectors, one can investigate the presence of twisting between the primary and secondary mirrors.

To visualise these results as a function of telescope position, a set of bubble plots for the X, Y-axis and detector differences in X and Y-axis is shown in Fig. 3.8. The first two subplots show the X and Y displacements measured by both detectors. The two detectors are given different bubble textures in the plot to differentiate between them. As with the preliminary results, the same trends can be seen. Displacements measured along the X-axis grow positively when the telescope is pointing east and negatively when pointing west, while the displacements measured along the Y-axis grow positively when pointing south of zenith and negatively when pointing north of zenith. Investigating the changes in detector differences, assuming no twisting of the secondary mirror with respect to the primary, it would be expected that the differences between detector measurements

Detector	Observed Value	Expected Deviation	Maximum Observed Deviation
Interferometer	Axial Defocus (µm)	30.8	51.9
	Tip Rotation (arcsec)	2.9	16.5
	Tilt Rotation (arcsec)	1.6	8.7
PSD Detector A	X Displacement (µm)	68.3	125.9
	Y Displacement (µm)	103.9	186.9
PSD Detector B	X Displacement (µm)	80.8	134.6
	Y Displacement (µm)	115.7	219.1

Table 3.6.: Summary of secondary measurements.

are constant in the X and Y-axis respectively. From these measurements, most of the detector differences are within two to three standard deviations of the measured values themselves, making them considerably small. And while some dependence of position can be seen in the third and fourth subplots in Fig. 3.8, their magnitude is not sufficient to cause significant concern.

An additional way of visualising the PSD data is once again possible by mapping the measured positions on the PSD surface. Similarly to the preliminary results, Fig. 3.9 shows the measured displacements from both detectors projected on a common frame of reference. Once again, an expected deviation on both axes is shown in the form of an ellipsis sized according to the standard deviation of the measurements in X and Y respectively. The displayed data once again reinforces the visible trend that the displacements in the Y-axis are almost twice are strong compared to the X-axis displacements. Numerically, this is shown by the X-axis having expected displacements of 68.3 and 80.8 µm measured by detectors A and B respectively, while the Y-axis has a 103.9 and 115.7 µm expected displacements from detectors A and B respectively.

3.2.3. Discussion

With the data gathered from these additional measurements, another set of expected and worst case displacements can be estimated, as was done with the preliminary data. Summarising over the previously discussed results, the interferometer measurements provide one estimate of expected axial defocus and tip, tilt angular displacements, along with one estimate of maximum displacement for each. From the PSD measurements, each detector provides one estimate of expected displacements and one for maximum displacement for each of the two axes, X and Y. All together these estimates are shown in Table 3.6.

These summarised results can be combined with the preliminary results in order to characterise the telescope's mechanical deviations and infer their optical effects. By averaging all of the expected and maximum observed deviations obtained along the

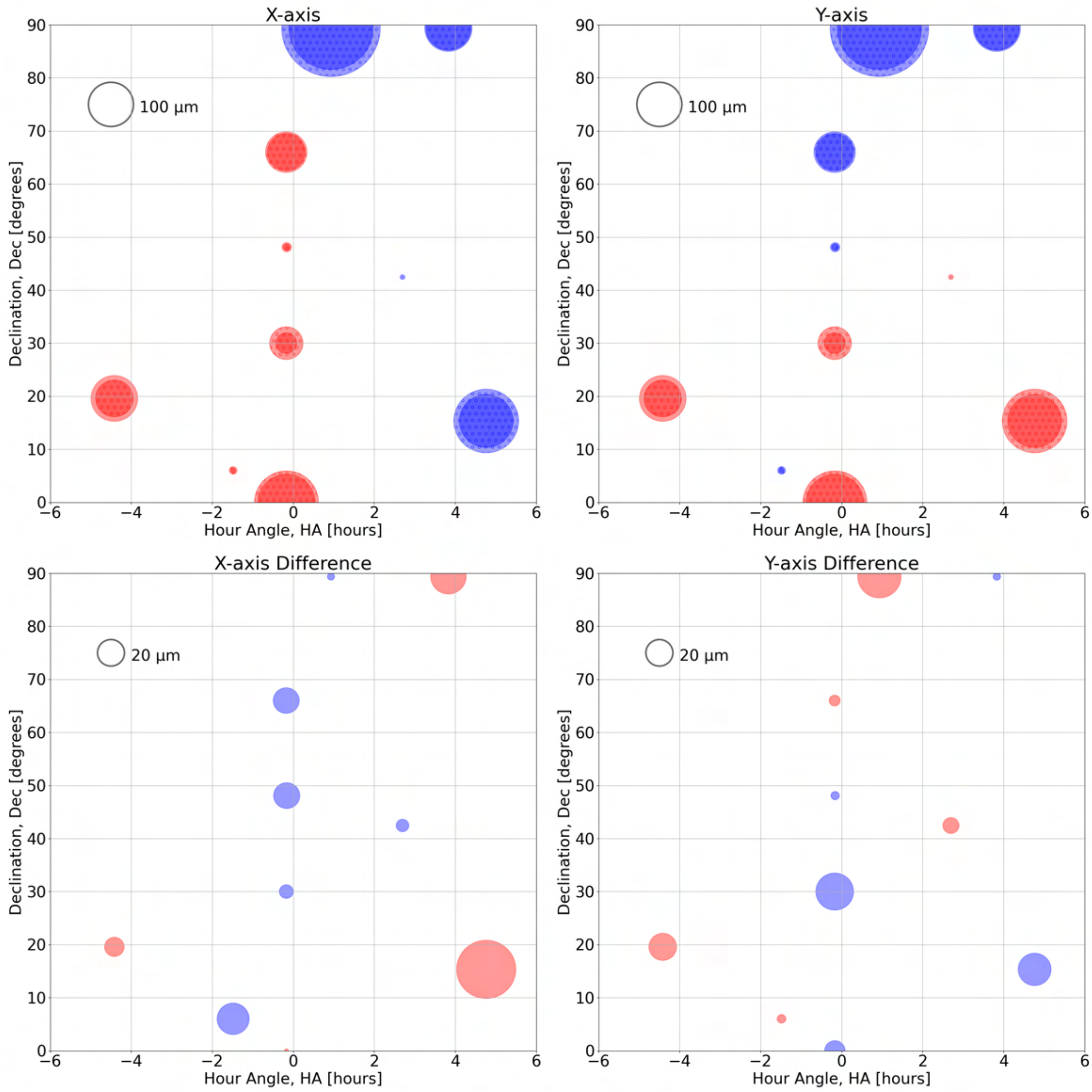

Figure 3.8.: Bubble plots of the secondary PSD measurements. Bubble size represents displacement amount, and the empty bubbles provide size reference. The measurement bubbles are coloured red for positive displacement and blue for negative.

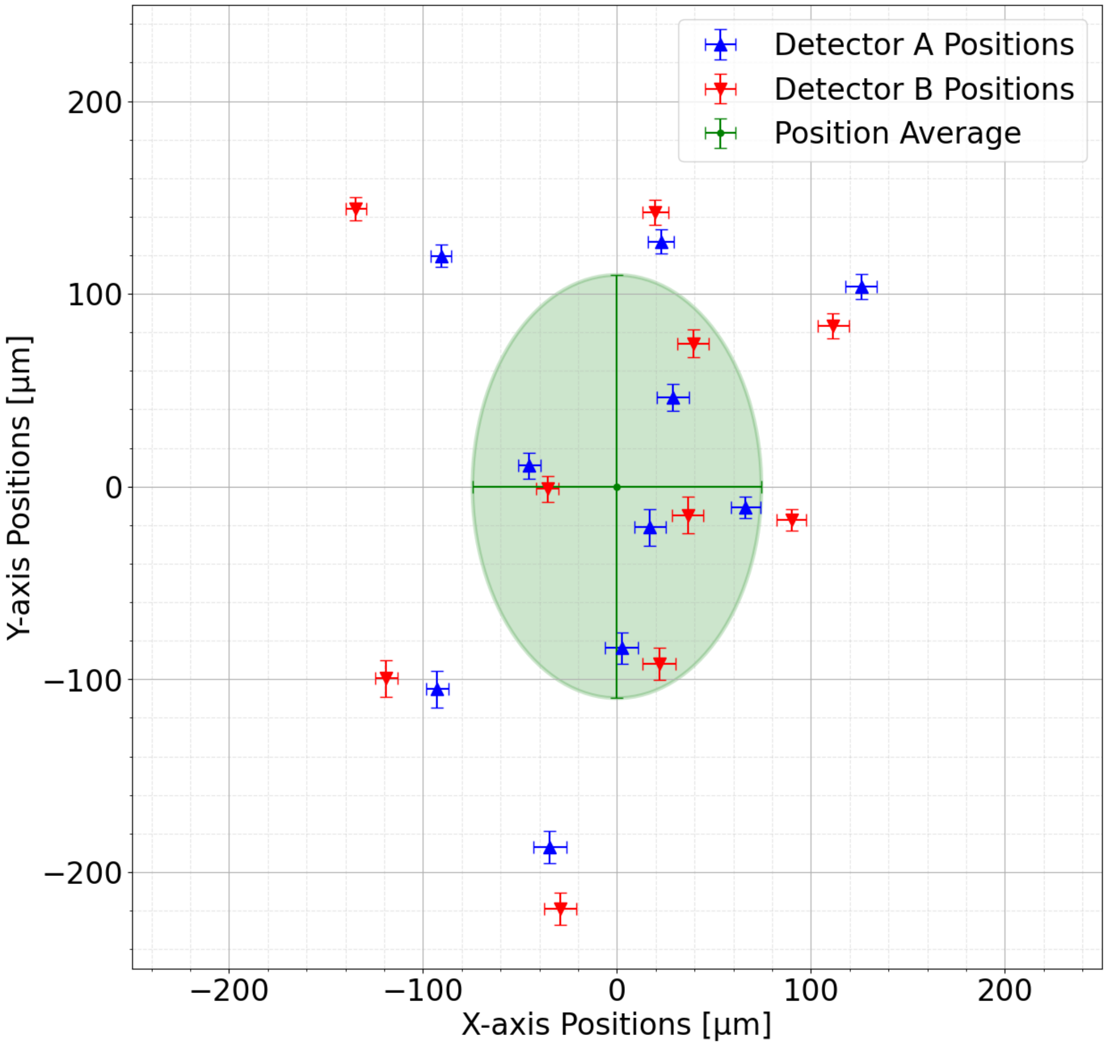

Figure 3.9.: Map of the recorded relative positions from the additional measurements on Feb 21. The blue and red scatter represent the measured relative positions by detectors A and B respectively. The green surface represents the range of expected displacements estimated as the standard deviation of the blue and red scatters.

various measurements taken, the following values were obtained. The expected displacements between the primary and secondary mirrors of the telescope are an axial defocus of 36 ± 9 µm, a tip rotation of 8 ± 5 arcsec, a tilt rotation of 4 ± 2 arcsec, X-axis displacement of 73 ± 3 µm and a Y-axis displacement of 118 ± 16 µm. The maximum observed displacements are an axial defocus of 63 ± 14 µm, tip rotation of 18 ± 5 arcsec, a tilt rotation of 8.2 ± 1.4 arcsec, an X-axis displacement of 130 ± 4 µm and a Y-axis displacement of 230 ± 60 µm. This summarised behaviour can then be used to estimate the expected and worst case changes in image quality for the 1.5m LFOA.

3.3. Telescope assessment

With the help of optical simulations, namely the ZEMAX OpticStudio software package, a characterisation of the 1.5m telescope at the "Leopold-Figl" Observatory for Astrophysics was made. The errors of the optical system were estimated by varying several degrees of freedom and creating a characterisation curve for axial displacements, angular displacements, which can be either tip or tilt, and lateral displacements, which can be either in the X or Y direction. This optical characterisation can be seen in Fig 3.10 as both the rms Wavefront error, W_{rms} measured in µm and the Strehl ratio, S_R, for the previously mentioned degrees of freedom.

Using this characterisation with our previously measured expected and maximum displacements of the telescope system, the optical error produced by each of these can be calculated. Table 3.7 shows the measured expected and maximum displacements and their respective errors. From the Strehl ratio, the axial defocus can be observed to have the most significant impact on image quality, resulting in an expected Strehl ratio of 4.1% and a worst case 0%. This is to be expected, however, since for each observation the telescope needs to be refocused onto the target object. Knowing this, the effects of axial defocus can be overlooked since they are easily corrected during normal telescope operation.

Apart from axial defocus, the other expected displacements are seen to have a smaller impact on image quality, with the angular displacements resulting in a Strehl ratio above 99% each and the expected lateral displacements resulting in Strehl ratios between 94% and 98%. The maximum estimated displacements have a more significant contribution to image quality with the angular displacements resulting in Strehl ratios of 96% to 99%, and the lateral displacements resulting in Strehl ratios of 93.7% for the X-axis, and most significantly, an 81.7% Strehl ratio caused by the Y-axis displacement.

However, these measurements are estimates of individual mechanical disturbances. To better understand the behaviour of the telescope structure as a whole, an additional series of simulations were made with the combined effects of mechanical errors, given as a series of scenarios. The first two scenarios investigate the combined expected and worst case displacements as given in Table 3.6 with and without axial defocus. As previously

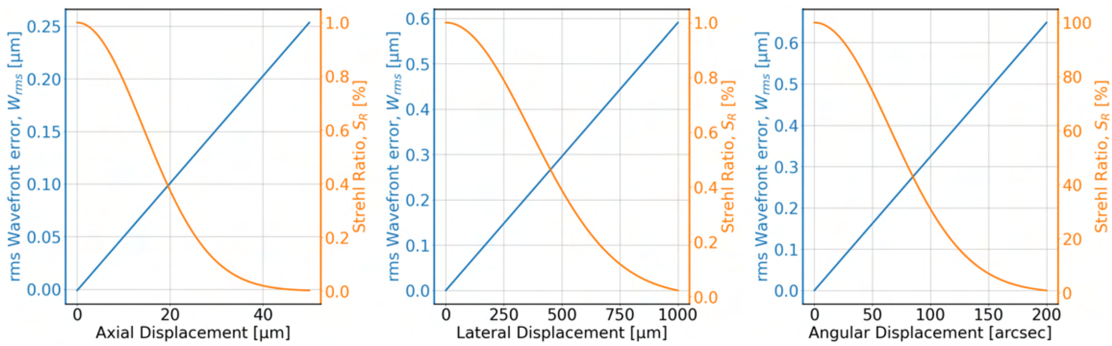

Figure 3.10.: Mechanical sources of error and their effect on optical quality as calculated by simulations of the 1.5m LFOA telescope. The blue curves represent rms Wavefront error, W_{rms}, while the orange curve represents Strehl ratio, S_R.

Measurement	Estimated Value	RMS WFE	Strehl Ratio
Axial Defocus (Expected)	36 ± 9 µm	0.18 µm	4.1 %
Tip Rotation (Expected)	8 ± 5 arcsec	0.02 µm	99.2 %
Tilt Rotation (Expected)	4 ± 2 arcsec	0.01 µm	99.8 %
X Displacement (Expected)	73 ± 3 µm	0.04 µm	97.9 %
Y Displacement (Expected)	118 ± 16 µm	0.07 µm	94.8 %
Axial Defocus (Maximum)	63 ± 14 µm	0.3 µm	0.0 %
Tip Rotation (Maximum)	18 ± 5 arcsec	0.06 µm	96.2 %
Tilt Rotation (Maximum)	8.2 ± 1.4 arcsec	0.02 µm	99.2 %
X Displacement (Maximum)	130 ± 4 µm	0.08 µm	93.7 %
Y Displacement (Maximum)	230 ± 60 µm	0.14 µm	81.7 %

Table 3.7.: Summary of optical errors induced by individual measured mechanical displacements. Both expected and maximum (worst case) displacement estimates are included.

		Expected	**Worst Case**	**Example 1**	**Example 2**
Corrected focus	W_{rms} (µm)	0.026	0.052	0.029	0.012
	S_R (%)	93.6	77.0	92.3	98.5
Not refocussed	W_{rms} (µm)	0.144	0.251	0.189	0.032
	S_R (%)	13.0	<10%	<10%	90.2

Table 3.8.: Summary of the Optical effect of four proposed scenarios of combined mechanical disturbances. The expected and worst case (maximum) conditions are given in Table 3.7, while examples 1 and 2 are given as the displacements between two consecutive measurements. Example 1 is given by displacements between measurements 2 and 3, while example 2 is given by displacements between measurements 8 and 9.

discussed, the effect of axial defocus is the most severe and must be corrected between each observation. This is reflected in the simulation results, and therefore, a corrected focus needs to be assumed in order to investigate the effects of the other aberrations. The results of these two simulations show that, with corrected focus, the expected deviations lead to a Strehl ratio of 93.6% while the worst case deviations lead to 77%. Without refocusing, however, both scenarios result in errors corresponding to a Strehl ratio around and below 10%. The following two scenarios discussed were the displacements between two consecutive measurements, simulating more realistic conditions. Example no. 1, which investigates the displacements between measurements 2 and 3, shows the induced optical errors when the telescope is moved from east to west. These errors are slightly higher than the ones from the expected deviations case with a Strehl ratio of 92.3% with a corrected focus and less than 10% without refocusing. Example no. 2 investigates the displacements between measurements 8 and 9, which were two very close positions on the meridian. This simulation reveal our best case scenario for optical errors, giving a Strehl ratio of 98.5% with corrected focus and 90.2% without refocusing. These simulation results are summarised and shown in Table 3.8.

In most cases, if considering only mechanical disturbances, the telescope is shown to remain diffraction limited, with the exception of the worst case scenario where its estimated Strehl ratio is below 0.8 for very extreme movements of the telescope. The only other factors left to consider are the cumulative effects of optical errors from mirror deformations or atmospheric seeing. Together with mechanical deformations, these effects could further increase the overall optical error to a point where correcting mechanical effects could improve imaging quality. Because of this, the implementation of an active correction system for mechanical effects should be considered, and its potential benefits compared to the drawbacks of such implementation.

4. Telescope Upgrade

To ensure the future scientific reliability of the “Leopold-Figl” Observatory for Astrophysics, the control system of the 1.5m telescope has been undergoing a major upgrade. This is the first major system upgrade taking place in the last 10 years and aims to maintain the scientific relevance of the telescope for the next 10 years. On the hardware side, the aim is to improve the pointing and tracking precision of the telescope as well as introducing an end-to-end control system which allows the planning, execution, analysis, and archiving of observations. On the software side, the upgrade will include an improved web-based graphical interface, which will facilitate easy remote access to the telescope control system, expanding the already existing remote capabilities of the telescope. This not only maintains the relevance of this facility, but expands its use cases and user base, while reducing its ecological footprint by requiring fewer in person visits. [20]

As part of the goal to ensure the continued optimisation of the LFOA, this project has provided assistance to the software upgrade efforts by turning the previous graphical interface into a new web-based interface for the control system upgrade. The benefits to this include improved ease of access and ease of maintenance. This implementation allows users, such as guest scientists, to connect with only a web browser and removes barriers such as version dependencies and unintuitive programming languages. It also allows for quick updates based on user feedback, ensuring the continuous improvement of the user experience. As the need for remote observations has increased, the user interfaces of telescopes have to grow as well. A web-based interface, together with an improved control system incorporating fast control, analysis, and storage, can facilitate this growth and revitalise this instrument as demand for remote observation is growing. [21]

The work done as part of this project was recreating the main interface menus necessary for remote observations. This included the menus for target control, telescope control, and dome control. Additional menus offer extended information about the telescope’s operation, which could be necessary for telescope maintenance; however, the average guest user should be able to make most observations with access to only these three menus. The web-interface is built using HTML, and most of the assets and elements use a popular open source library known as Bootstrap [22]. It is designed to be the front-end mask that will connect to the server side back-end of the telescope control system. Due to the modular nature of this interface, the elements created so far can be easily expanded to create additional elements and menus, simplifying future updates.

An important element of this interface is its header. This section is always displayed and contains important telescope controls such as an emergency motor stop and a dome lock toggle, as well as status indicators for weather and telescope connection. For observations, the header contains critical time information such as Modified Julian Date (MJD), Coordinated Universal Time (UTC), and Sideral Time, which can be useful in determining the location of celestial objects. And lastly, the header enables the connection and disconnection of the interface.

After the header, a navigation bar is present, which allows the user to connect to any of the control menus available. The first menu and the one which was most often used over the course of this thesis was the target control menu labelled "Target". To illustrate the interface upgrade, Fig. 4.1 shows a comparison of the target control window from the previous interface and the HTML-based one. The "Target" window allows the user to select a target by providing its coordinates, track the given target, and also manually control the telescope's position. The target input form takes the desired celestial object either in the form of an Object ID related to a celestial object database, or by manually setting the sky coordinates of the object, Right Ascension (RA) and Declination (Dec). Additional inputs, such as proper motion and Epoch, can improve locating these objects if their reported location on the sky has changed over time. If, however, the telescope is not being used to track a point on the sky and its position needs to be altered in other ways, this can be achieved through a selection of buttons, toggles, and select menus found in the middle of the control window. The last section of the "Target" window displays relevant information for the observations being made. Some of this information describes the telescope's position, like Hour Angle (HA), the previously mentioned RA and Dec and Zenith Distance (ZD). The other data can be used in observation interpretation, like Airmass, which describes atmosphere thickness in the line of sight and is used in magnitude measurements, or f-error, which describes the mismatch between focal ratio and telescope aperture. As seen in the web-based interface, all of these elements have been replicated; however, the updating of information and control of inputs is handled by the back-end of the control system. Since these have not yet been connected, placeholders have been used instead during the building of the interface.

The other two control windows are also relevant for telescope users and can be seen in Fig. 4.2. Before a user can use the target pointing of the telescope, its motors can be turned on. The window labelled "Telescope" contains the controls for starting and stopping the telescope motors alongside two indicators showing the status of the motors. Since these functions are important to operating the telescope, these buttons must be clear and visible. For the same reason, the "Stop motors" button is also coloured red, such that in emergency situations it can be easily found and actuated. This window also contains other telescope controls, such as mirror cover control, which enables the protection of the primary mirror when the telescope is not in use, flatfield lamps for CCD calibration, and focus adjustment, which enable the refocusing of the optics before each observation. The focus adjustments window also contains position and status indicators for the focusing mechanism, as well as a select menu for focus setpoints. Lastly, this window shows a set of telescope temperatures which can be used to monitor the varying temperatures

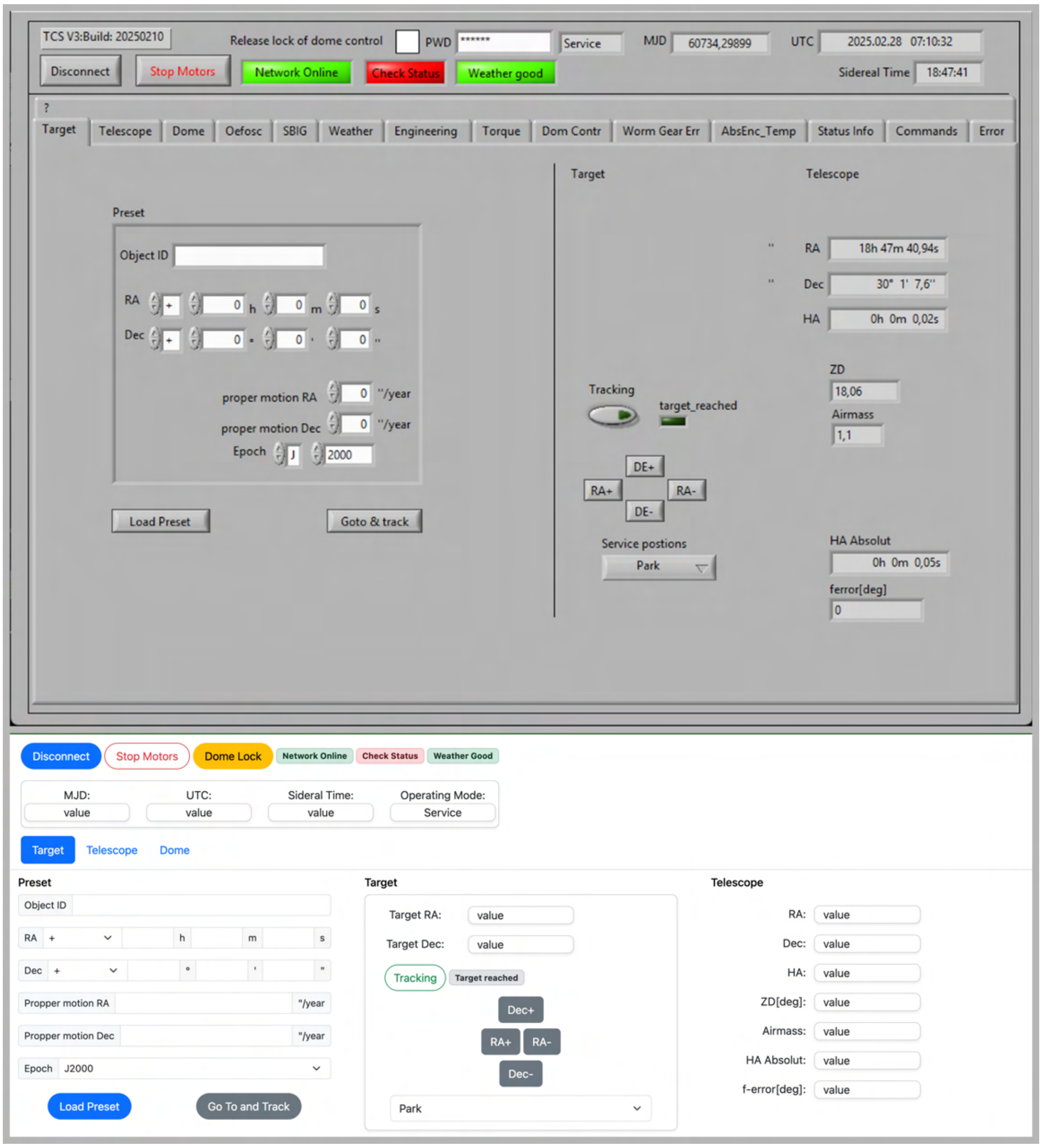

Figure 4.1.: Target window in the new web-based telescope interface (bottom) compared to its corresponding window from the old telescope graphical interface (top).

across the instrument. This includes focus, structure and mirror cell temperatures. Lastly, the “Dome” window contains controls for the various elements of the observatory’s dome. This includes dome position, which allows the rotation of the dome slit, dome shutter, which opens and closes the observation slit, and wind shield controls, which position a canvas shield at the bottom half of the dome slit to block wind from entering the telescope dome and causing wind disturbances which could affect seeing. Each control has a position status window, and the position controls have the option of selecting a set position from a select menu. The rest of the “Dome” window contains information displays for environmental conditions at the observatory site, which could be of interest for users operating the instrument. The first group of displays describe average and peak wind speeds and the wind direction, while the second group describes a set of temperatures within the observatory building, namely the elevator temperature (Temp_lift), data center temperature (Temp_EDV) and power supply temperature (Temp_USV). The last three groups provide temperature, humidity and dewpoint data for the dome, balcony and ambient environments, as well as air pressure for the balcony. These conditions help users monitor harmful weather conditions as well as temperature gradients, which affect air currents and therefore telescope seeing. Together, all of these elements are necessary for monitoring and operating the telescope, making this control system upgrade, with its web interface, a useful change in telescope accessibility.

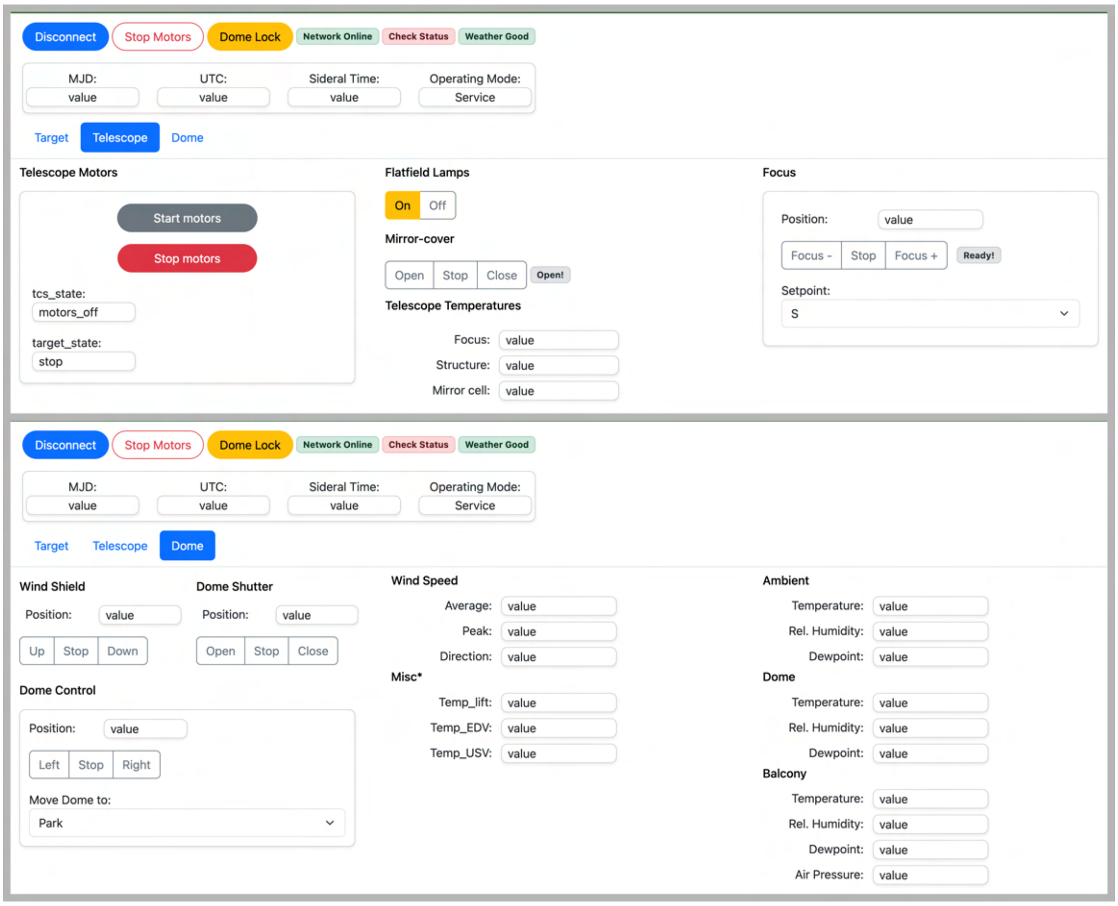

Figure 4.2.: Control windows in the new web-based interface for "Telescope" control (top) and "Dome" control (bottom).

5. Conclusion

The object of study for this work has been the opto-mechanical behaviour of the 1.5m telescope of the Leopold Figl Observatory for Astrophysics. An investigation of telescope theory and optical errors has shown possible aberrations and their sources, introducing active optics as a possible solution for reducing structural errors of mechanical origin. Following up on existing work, a metrology system developed at the Automation and Control Institute (ACIN) at TU Wien has been adapted for the LFOA 1.5m class telescope. A lateral displacement sensor was added, and mounting solutions were found. Several measurements were then taken to investigate the structurally induced changes in the optical system, and their analysis has led to an assessment of the effect on image quality and correction possibilities.

Measurement analysis has shown the following links between possible optical errors and their mechanical origin. Axial defocus was shown to have the largest potential of inducing optical errors. The typical axial displacement between consecutive measurements being enough to reduce the Strehl ratio below 80% or even below 10% in more extreme cases. Despite this, the impact of axial defocus can be corrected by refocusing the telescope system before each observation. Additionally, if the observation time is such that axial defocus becomes considerable during a singular observation, an active refocusing system can be introduced. Since the telescope already has a focusing mechanism, an active refocusing system could be achieved simply with a software implementation. The mechanical error with the second highest impact is lateral displacement. Independently, the typical effect this error has on image quality is shown to be negligible, as the Strehl ratio remains above 0.8 and the system is still diffraction limited. However, in a worst case scenario and in combination with other errors, either mechanical or from seeing effects, the telescope system was shown to no longer be diffraction limited. Therefore, correcting these lateral displacements could noticeably improve imaging quality. Upgrading the secondary mirror to a semi active one with three degrees of freedom would be sufficient for correcting this mechanical error. The lowest impact on image quality was achieved by tip-tilt deviations, their typical effect on image quality being only a fraction (10% of W_{rms}) of the lateral displacement error. An active secondary mirror dedicated to the correction of this mirror would have to be an active hexapod system as shown. However, due to the low impact of this deviation, implementing such an active system only for this error would not provide significant advantages.

The control of the correction system is also an important aspect of deciding what technology should be implemented on the telescope. If an active system is to be implemented, the optical errors can be measured either with a metrology system like the one currently implemented or with a wavefront analyser. In this implementation, both options potentially block/borrow telescope light and reduce signal to noise ratios. In comparison with the wavefront analyser, the metrology system introduces numerous measurement errors, especially at the scale of this telescope, such as electrical noise, bending of optical fibres and movement of mechanical parts. All of these errors can be avoided by implementing a wavefront analyser, which is already industry standard for this sort of application. Another concern for this implementation is the reduction of signal to noise ratio by the image analyser. Since lateral displacements have been found to remain significantly stable during individual measurements, it would be more practical to implement an active correction system at the beginning of individual observations and then carry them out passively.

A drawback of the metrology system implemented at the telescope is that it is unable to detect the warping and deformation of mirror surfaces. These errors are usually corrected through the implementation of an active primary mirror. This is not an option at the LFOA since the heavy and thick primary mirror blank cannot be actively deformed, and replacing the primary mirror would be equivalent to rebuilding the telescope.

With the help of the theory presented, and according to measurement analysis, the 1.5m telescope of the LFOA has been shown to have a stable mechanical structure, which should allow for high quality imaging without the need for active optics. However, if compensation for additional optical errors is found to be necessary for the telescope to remain scientifically competitive, several active or semi-active options have been discussed. This assessment, together with the change to a web-based graphical interface, are among the first steps taken towards the modernisation of the LFOA. In the end, the continued optimisation of operations at the LFOA will make this a sustainable facility, attracting scientists and astronomy enthusiasts alike, and being a valuable asset to the national and international science community.

Bibliography

[1] R. N. Wilson, *Reflecting Telescope Optics I.* Berlin Heidelberg: Springer, 2 ed., 2007.

[2] R. N. Wilson, *Reflecting Telescope Optics II.* Berlin Heidelberg: Springer, 1 ed., 2001.

[3] "Universität Wien - Leopold Figl-Observatorium für Astrophysik." `https://foa.univie.ac.at/`. Accessed: 11-Jun-2025.

[4] N. López-Gil, F. Rucker, L. Stark, M. Badar, T. Borgovan, S. Burke, and P. Kruger, "Effect of third-order aberrations on dynamic accommodation," *Vision research*, vol. 47, pp. 755–65, 04 2007.

[5] W. R. N., "Active optics and the new technology telescope (NTT): The key to improved optical quality at lower cost in large astronomical telescopes," *Contemporary Physics*, vol. 32, no. 3, pp. 157–172, 1991.

[6] P. Schipani, D. Magrin, L. Noethe, C. Arcidiacono, J. Argomedo, M. Dall'Ora, S. D'Orsi, J. Farinato, L. Marty, R. Ragazzoni, and G. Umbriaco, "The active optics system of the VST: concepts and results," in *Ground-based and Airborne Telescopes IV* (L. M. Stepp, R. Gilmozzi, and H. J. Hall, eds.), vol. 8444, p. 84444Z, International Society for Optics and Photonics, SPIE, 2012.

[7] A. Sinn, P. Prager, C. Schwaer, and G. Schitter, "Design and evaluation of an active secondary mirror positioning system for a small telescope," *Journal of Astronomical Telescopes, Instruments, and Systems*, vol. 8, no. 2, p. 029007, 2022.

[8] C. F. Gauß, *Dioptrische Untersuchungen.* Göttingen Dieterich, 1841.

[9] W. Hamilton *Report Brit. Assoc.*, no. 3, p. 360, 1833.

[10] A. Maréchal, "Study of the combined effects of diffraction and geometrical aberrations on the image of a luminous point," *Rev. Opt. Theor. Instrum*, vol. 26, p. 257, 1947.

[11] P. Schipani, L. Noethe, D. Magrin, K. Kuijken, C. Arcidiacono, J. Argomedo, M. Capaccioli, M. Dall'Ora, S. D'Orsi, J. Farinato, D. Fierro, R. Holzlöhner, L. Marty, C. Molfese, F. Perrotta, R. Ragazzoni, S. Savarese, A. Rakich, and G. Umbriaco, "Active optics system of the VLT Survey Telescope," *Appl. Opt.*, vol. 55, pp. 1573–1583, Mar 2016.

[12] J. Puschnig, T. Posch, and S. Uttenthaler, "Night sky photometry and spectroscopy performed at the Vienna University Observatory," *Journal of Quantitative Spectroscopy and Radiative Transfer*, vol. 139, p. 64–75, May 2014.

[13] W. Pessemier, *Knowledge-driven development of telescope control systems*. PhD thesis, Arenberg Doctoral School, Belgium, 2017.

[14] "Displacement measuring interferometer." `https://www.attocube.com/en/products/laser-displacement-sensor/displacement-measuring-interferometer`. Accessed: 12-Jun-2025.

[15] "Two-dimensional PSD S5991-01 | Hamamatsu Photonics." `https://www.hamamatsu.com/eu/en/product/optical-sensors/distance-position-sensor/psd/two-dimensional-psd/S5991-01.html`. Accessed: 12-Jun-2025.

[16] "High-precision AD HAT - waveshare wiki." `https://www.waveshare.com/wiki/High-Precision_AD_HAT`. Accessed: 12-Jun-2025.

[17] "Roithner Lasertechnik - dot laser modules, 850 nm." `http://www.roithner-laser.at/laser_modules_dot_850.html`. Accessed: 12-Jun-2025.

[18] D. Rodríguez-Navarro, J. L. Lázaro-Galilea, I. Bravo-Muñoz, A. Gardel-Vicente, F. Domingo-Perez, and G. Tsirigotis, "Mathematical model and calibration procedure of a PSD sensor used in local positioning systems," *Sensors*, vol. 16, no. 9, 2016.

[19] F. Kreuzmair, "Opto-mechatronical analysis and outlook on potential improvements for Austria's largest telescope system," Master's thesis, Technischen Universität Wien Fakultät für Physik, 2025.

[20] "Gefördertes project FTI22-I-007." `https://www.gff-noe.at/forschungsfoerderung/details/FTI22-I-007/`. Accessed: 16-Jun-2025.

[21] D. Ricci, L. Cabona, B. Salasnich, L. Nicastro, L. Fini, A. Damonte, S. Tosi, and T. Shibata, "Easy remote observations using web interfaces: controlling an Italian telescope from Japan, and more," in *Observatory Operations: Strategies, Processes, and Systems X* (L. J. Storrie-Lombardi, C. R. Benn, and A. Chrysostomou, eds.), p. 31, SPIE, July 2024.

[22] "Bootstrap - the most popular HTML, CSS and JS library in the world." `https://getbootstrap.com/`. Accessed: 16-Jun-2025.

A. Appendix

This Appendix contains the circuit diagram and circuit design for the second variation of the PSD circuit boards.

The following is a listed of the various components present in these diagrams.

- Hamamatsu PSD detector, [15]
- Two dual-OpAmps for the 4 channels of the PSD,
- Three pin temperature sensor,
- Adjustable voltage regulator (TPS7A4901DRBR) (for BIAS),
- Two Ethernet ports,
- Micro resistors and capacitors of various values depending on the circuit requirements.

The Appendix also contains the PSD and interferometer plotsheets from the first and second measurement runs.

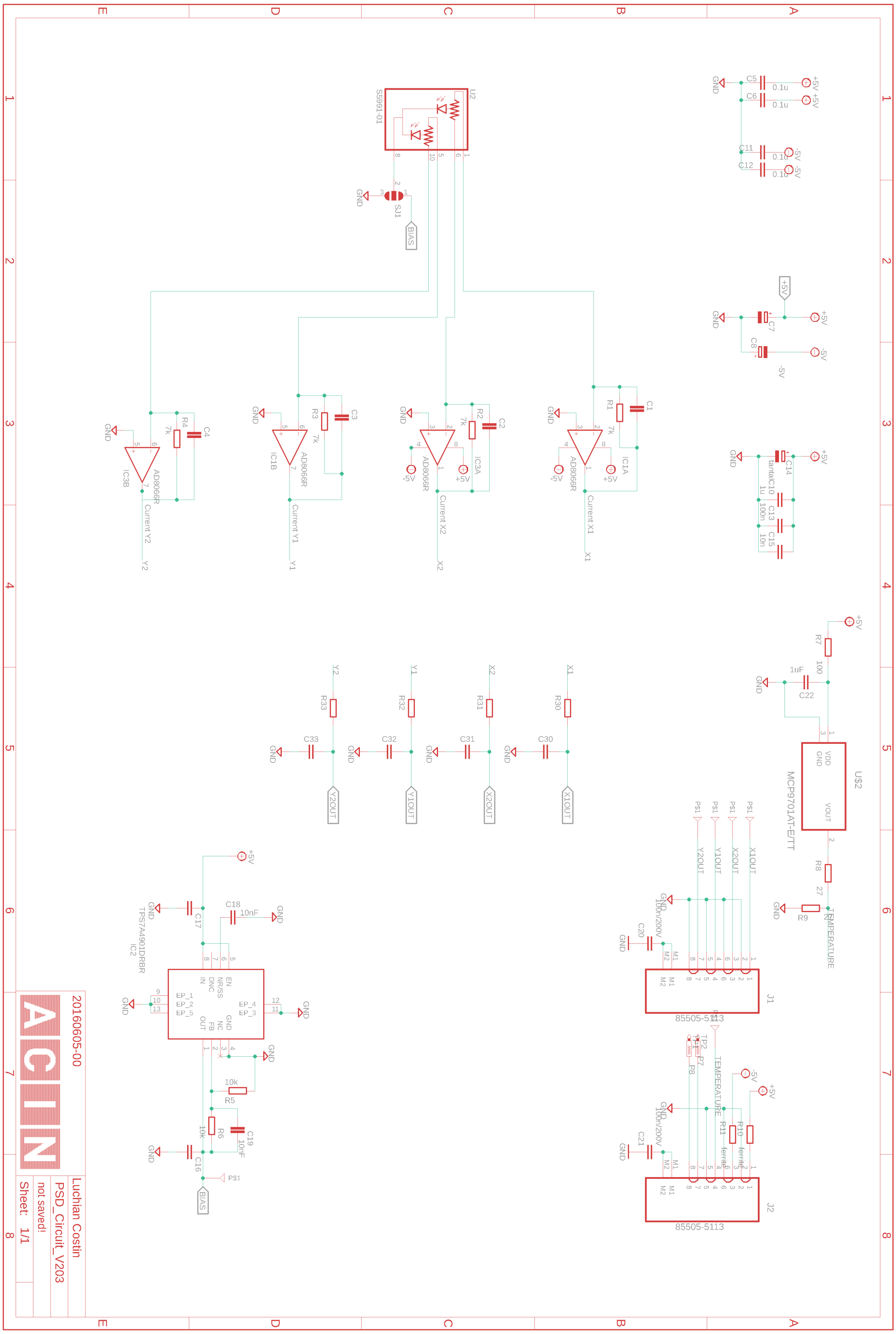

Figure A.1.: Circuit diagram of the PSD Lateral Measurement Circuit Board.

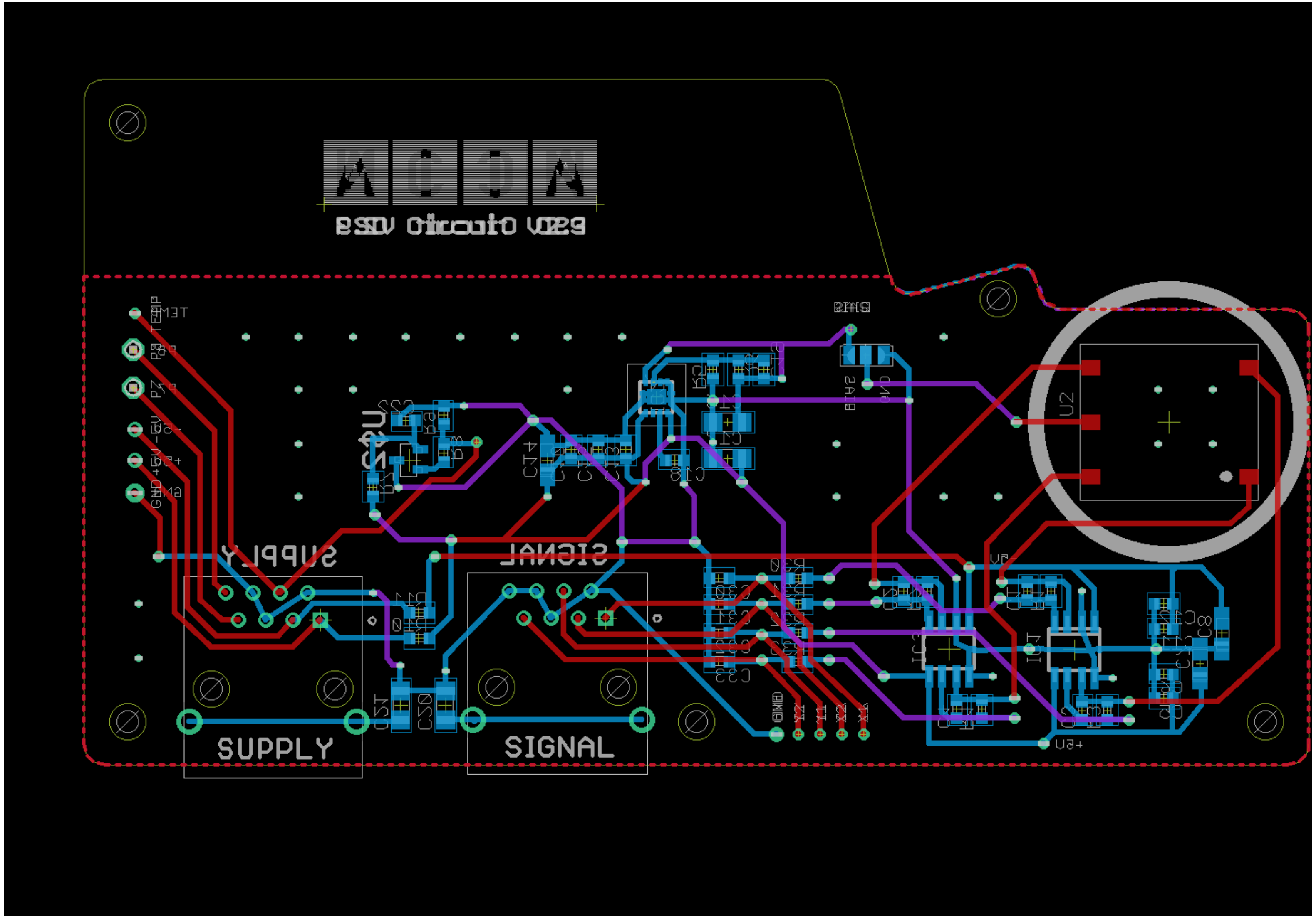

Figure A.2.: Design of the PSD Lateral Measurement Circuit Board.

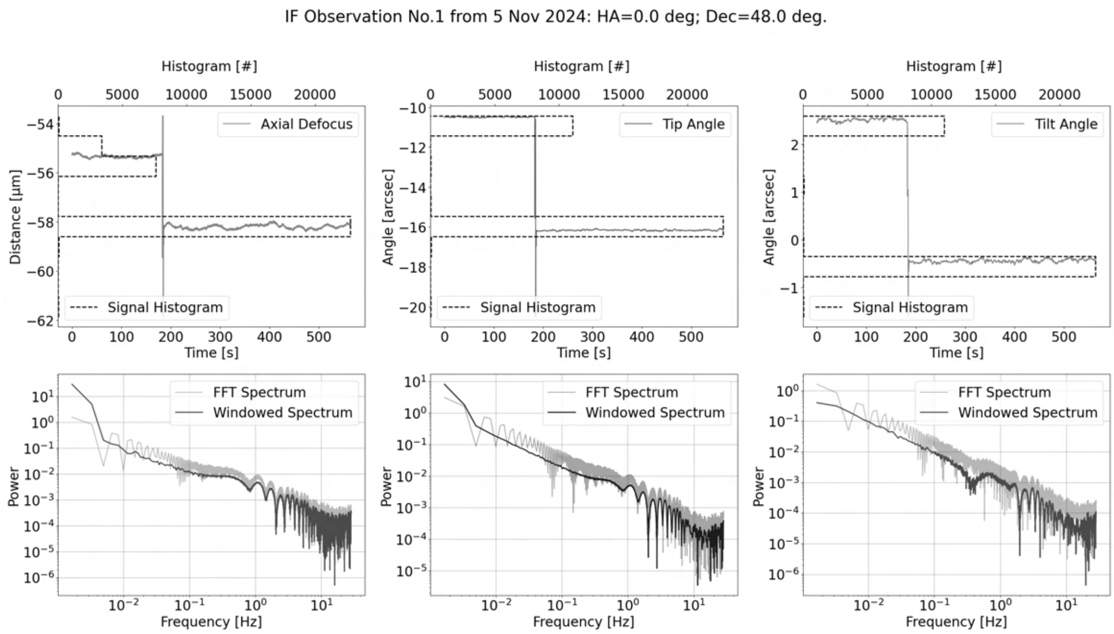

Figure A.3.: Plotsheet of interferometer observation no. 1 from November 5 2024. Measurement artifact was caused by alignment adjustments made while recording.

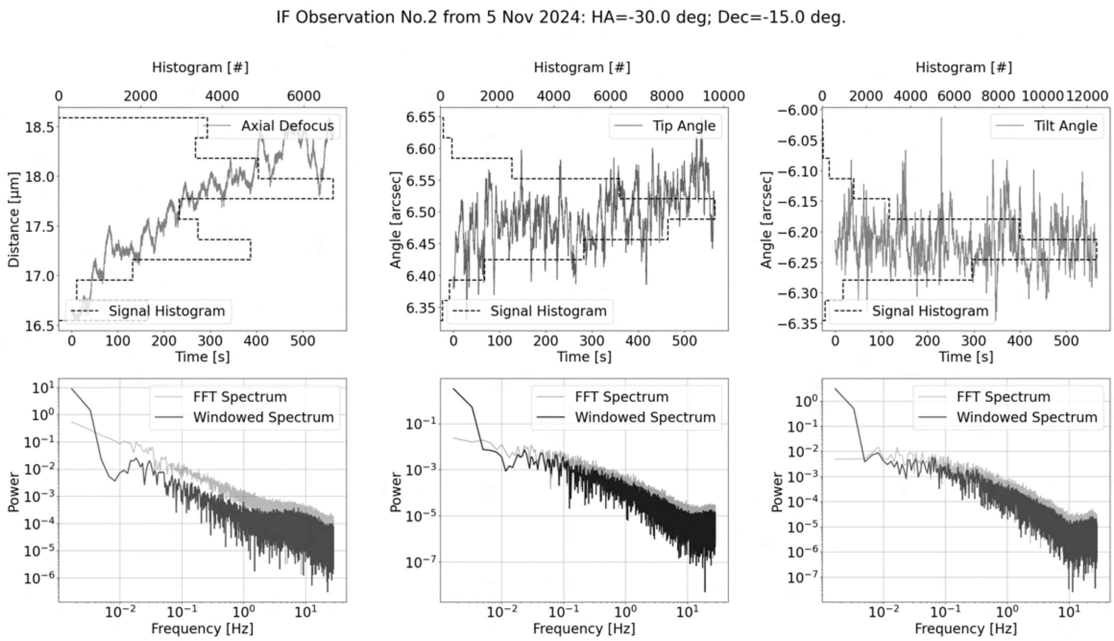

Figure A.4.: Plotsheet of interferometer observation no. 2 from November 5 2024.

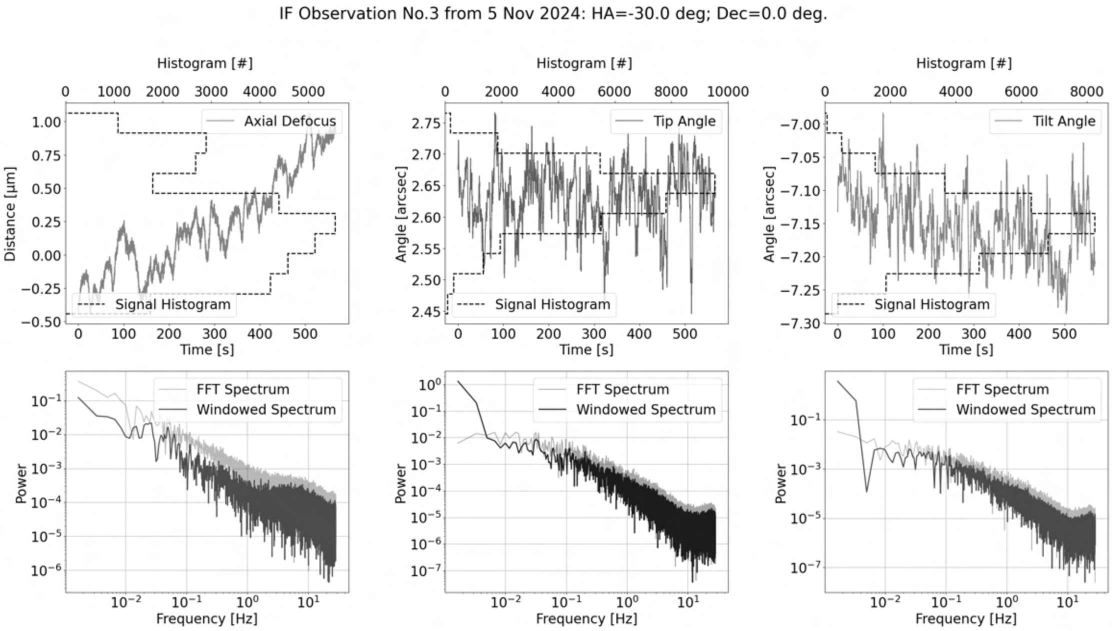

Figure A.5.: Plotsheet of interferometer observation no. 3 from November 5 2024.

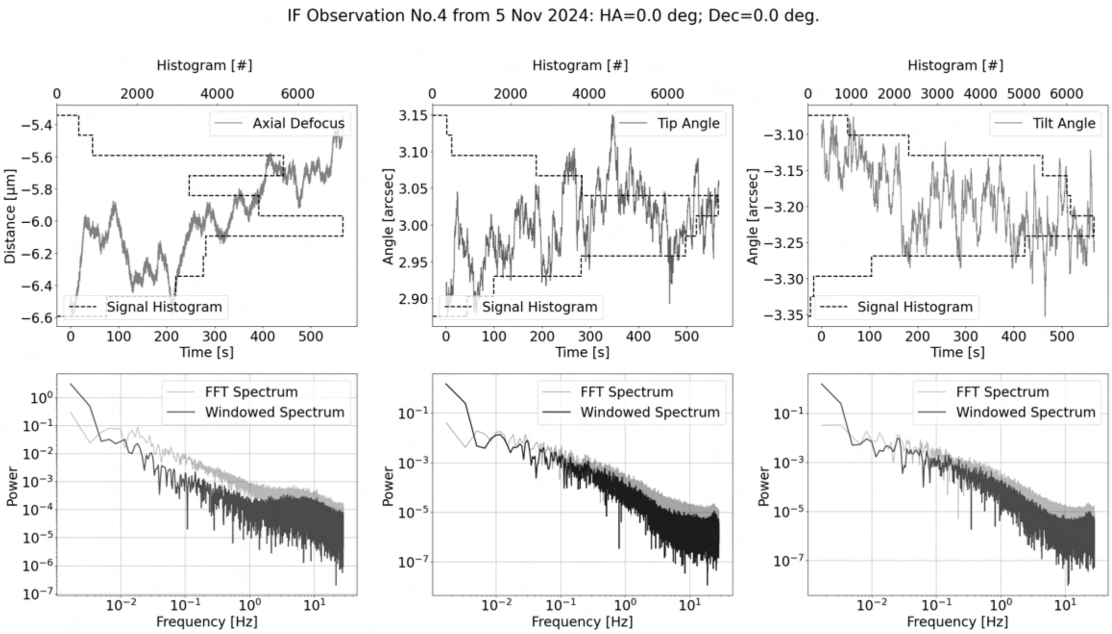

Figure A.6.: Plotsheet of interferometer observation no. 4 from November 5 2024.

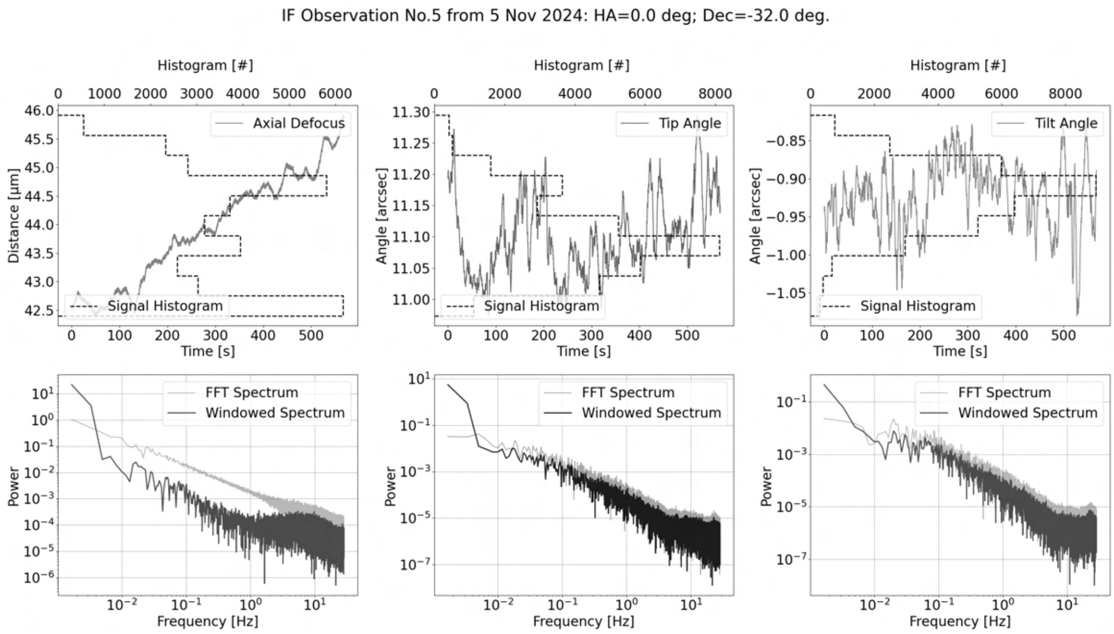

Figure A.7.: Plotsheet of interferometer observation no. 5 from November 5 2024.

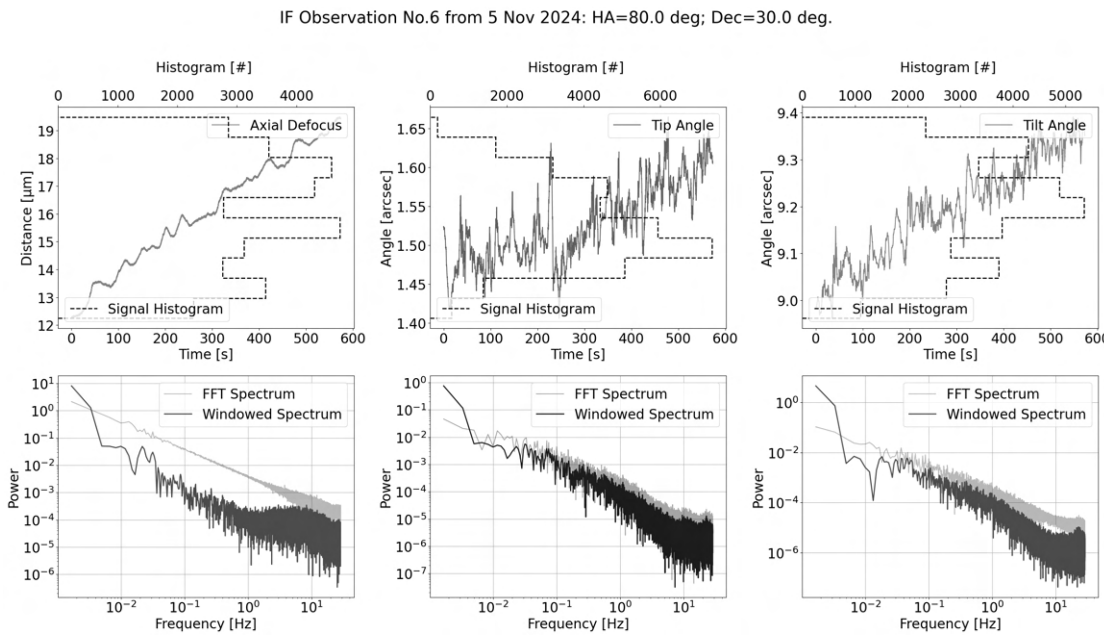

Figure A.8.: Plotsheet of interferometer observation no. 6 from November 5 2024.

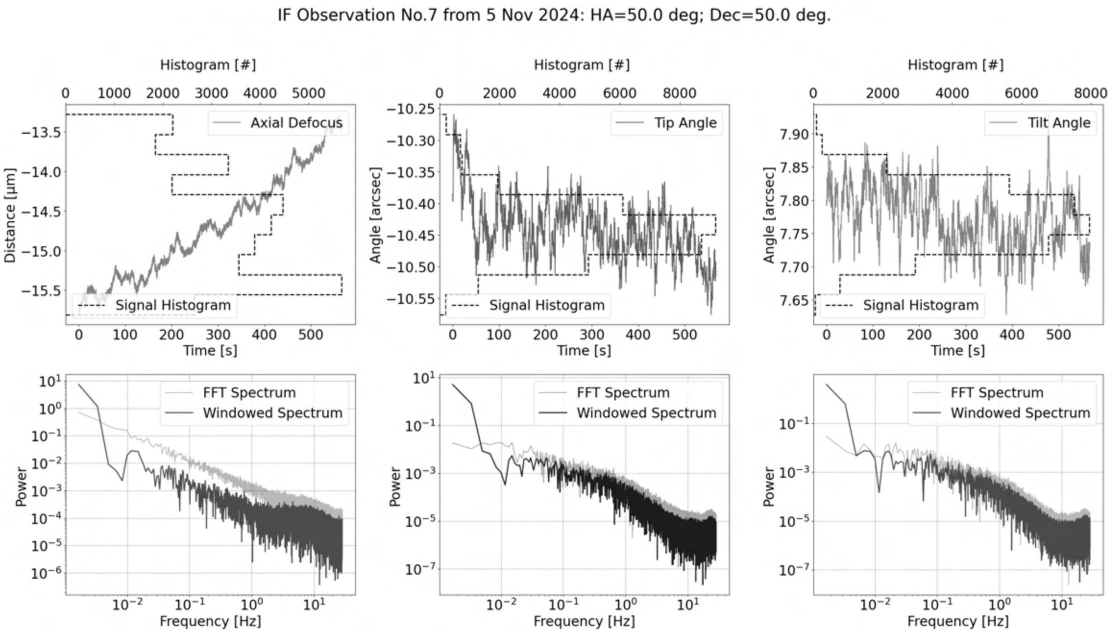

Figure A.9.: Plotsheet of interferometer observation no. 7 from November 5 2024.

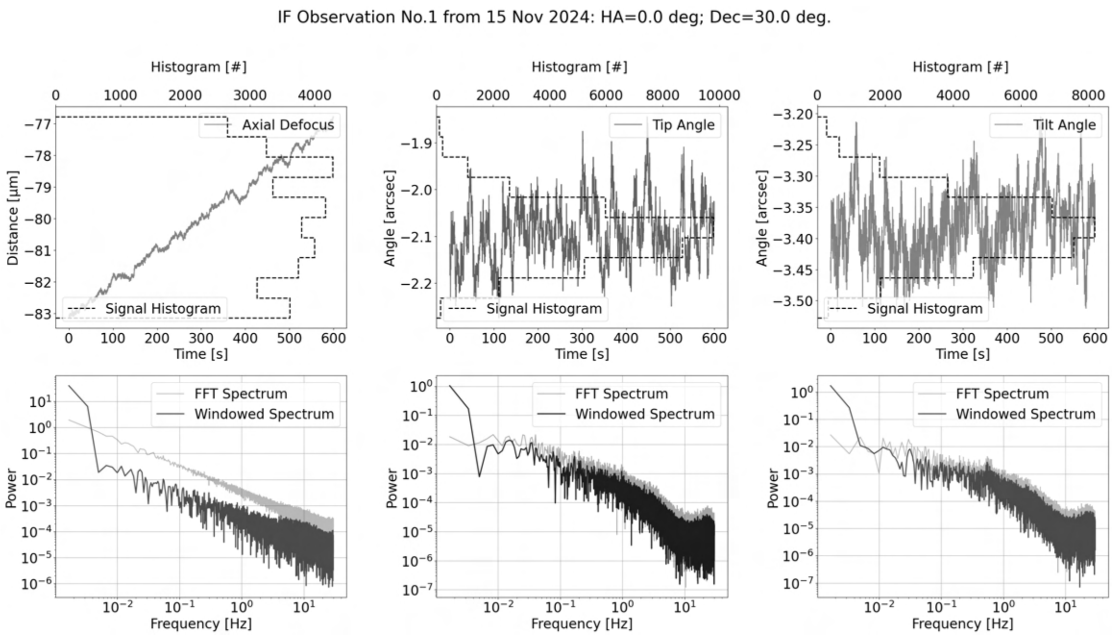

Figure A.10.: Plotsheet of interferometer observation no. 1 from November 15 2024.

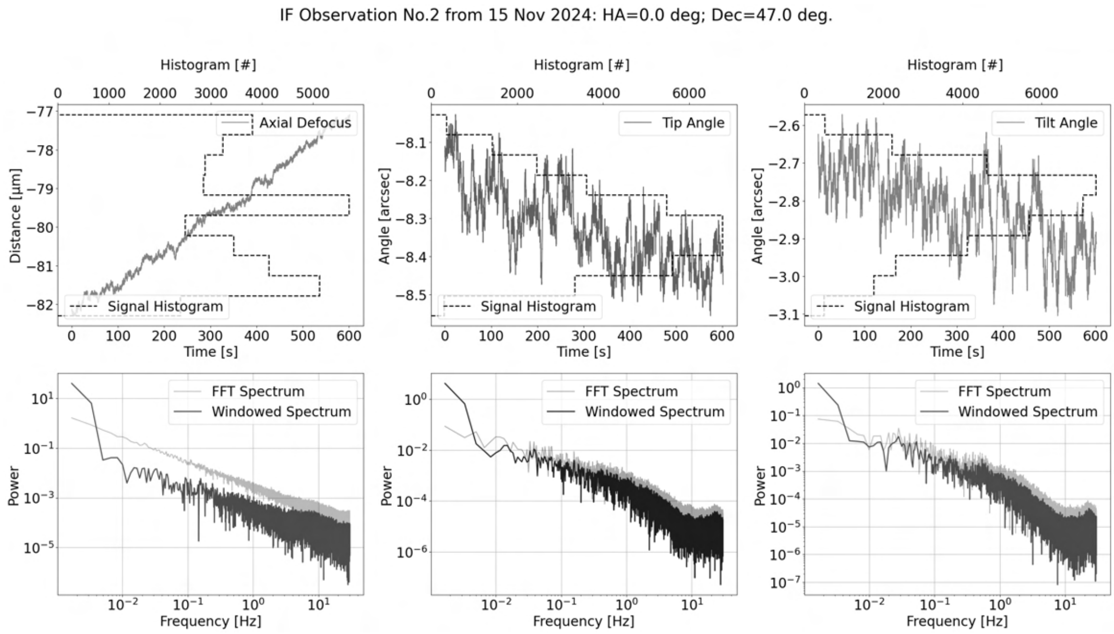

Figure A.11.: Plotsheet of interferometer observation no. 2 from November 15 2024.

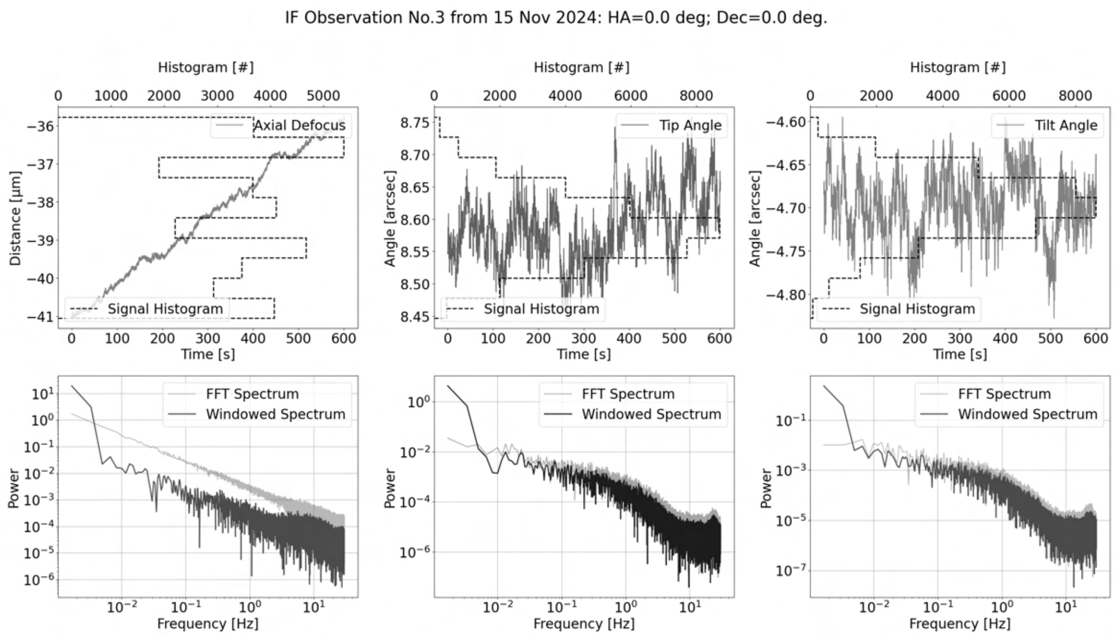

Figure A.12.: Plotsheet of interferometer observation no. 3 from November 15 2024.

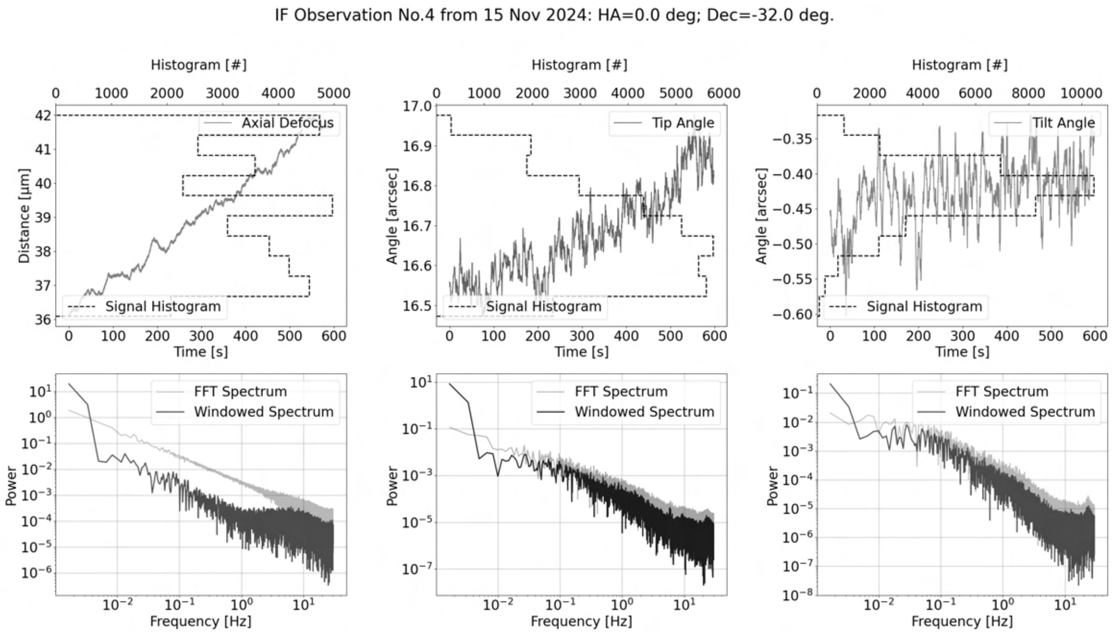

Figure A.13.: Plotsheet of interferometer observation no. 4 from November 15 2024.

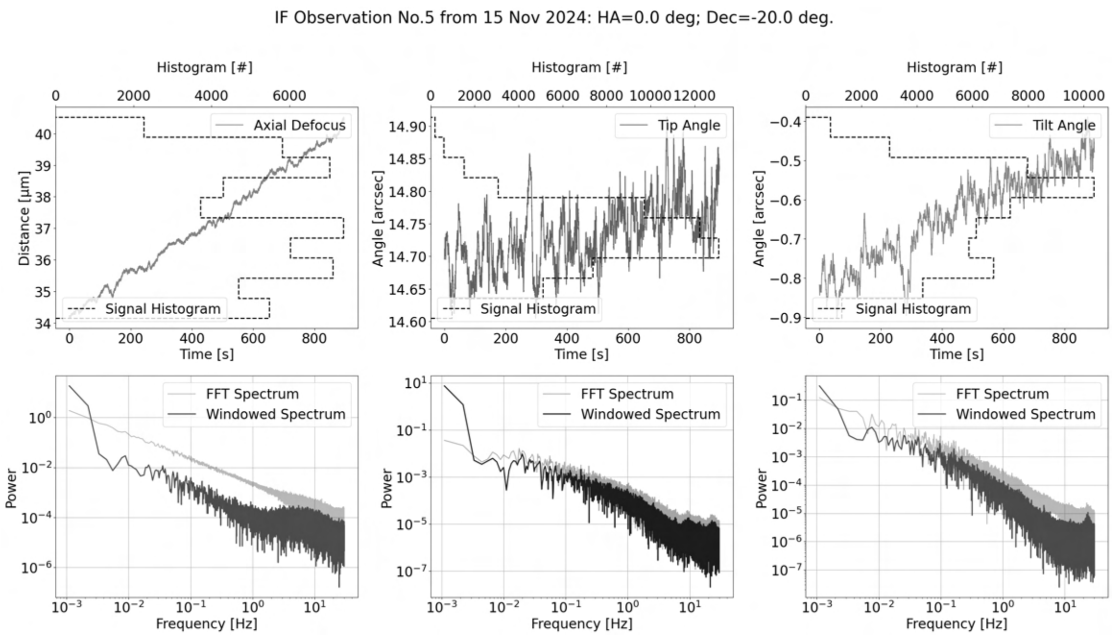

Figure A.14.: Plotsheet of interferometer observation no. 5 from November 15 2024.

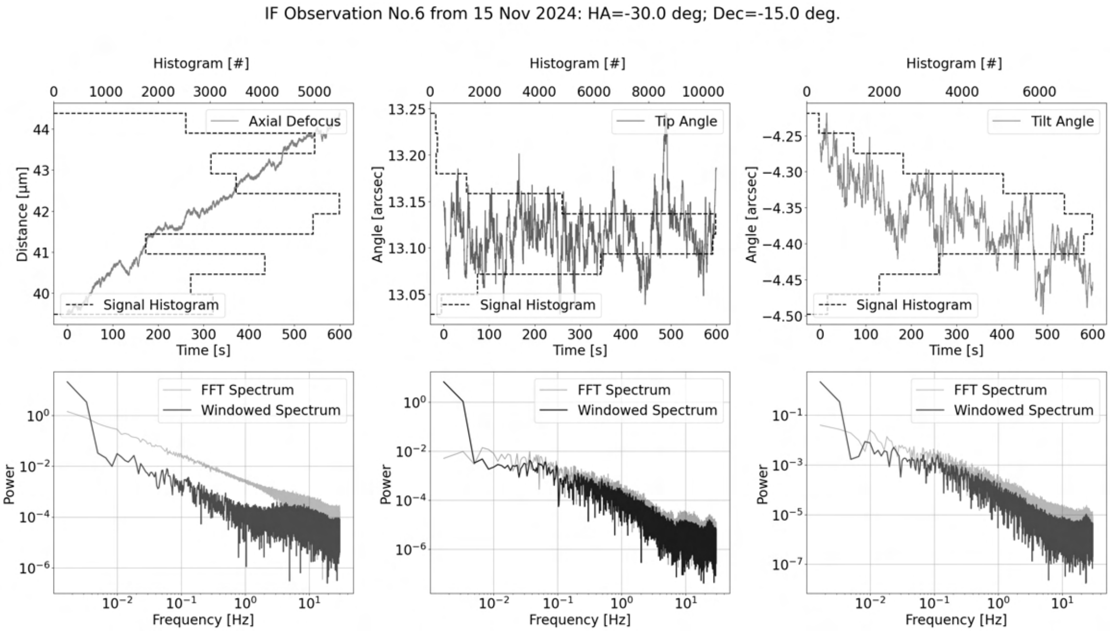

Figure A.15.: Plotsheet of interferometer observation no. 6 from November 15 2024.

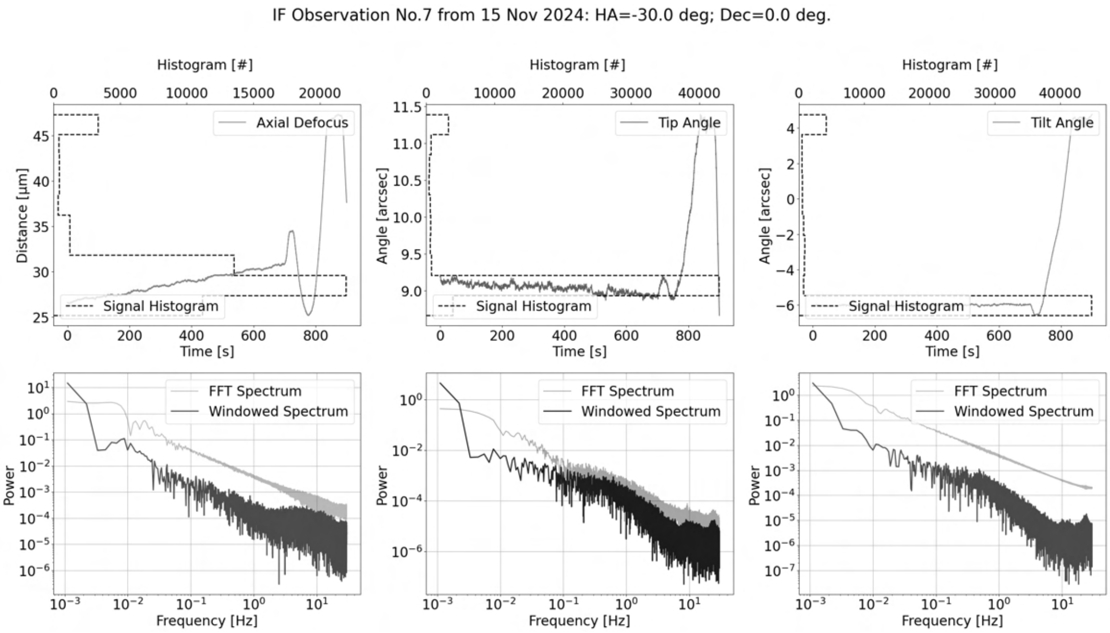

Figure A.16.: Plotsheet of interferometer observation no. 7 from November 15 2024. Measurement artifact was caused by accidental touching of the interferometer optical fibres during recording.

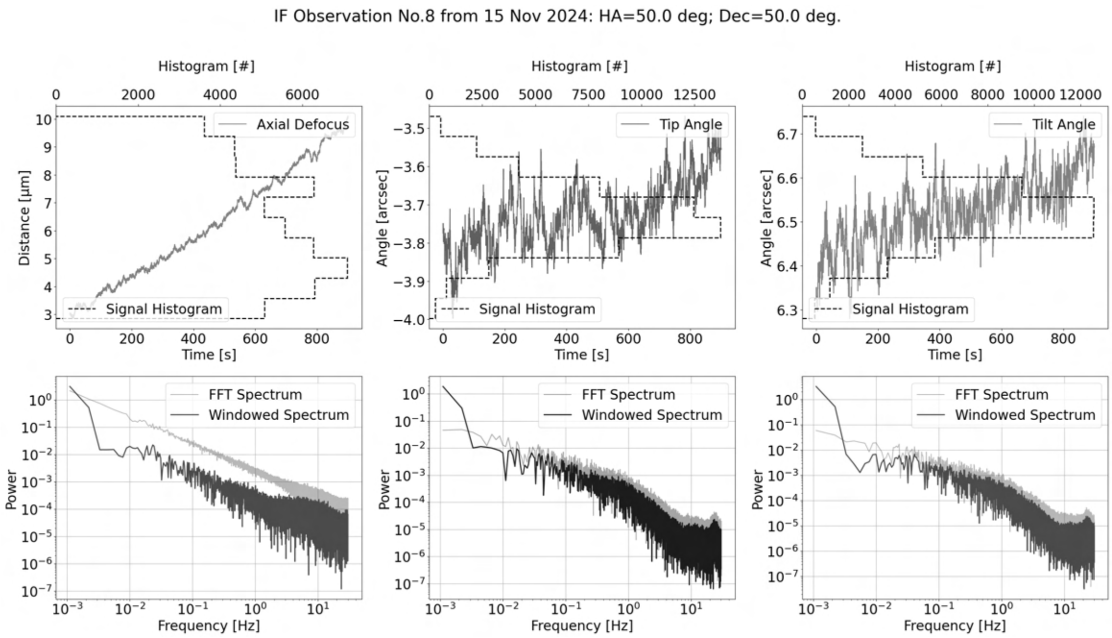

Figure A.17.: Plotsheet of interferometer observation no. 8 from November 15 2024.

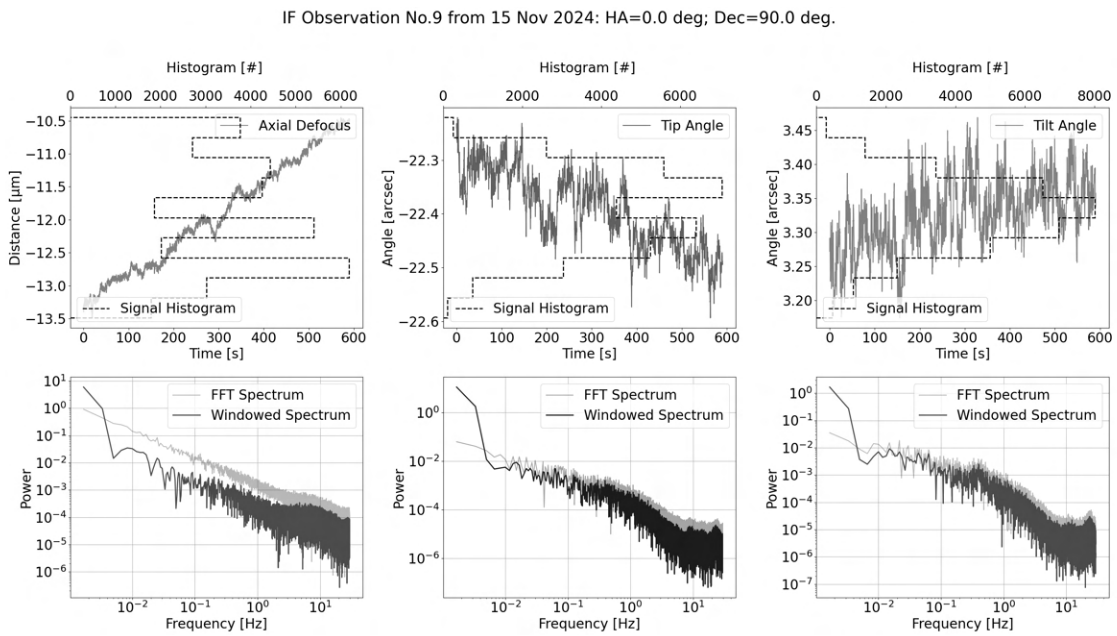

Figure A.18.: Plotsheet of interferometer observation no. 9 from November 15 2024.

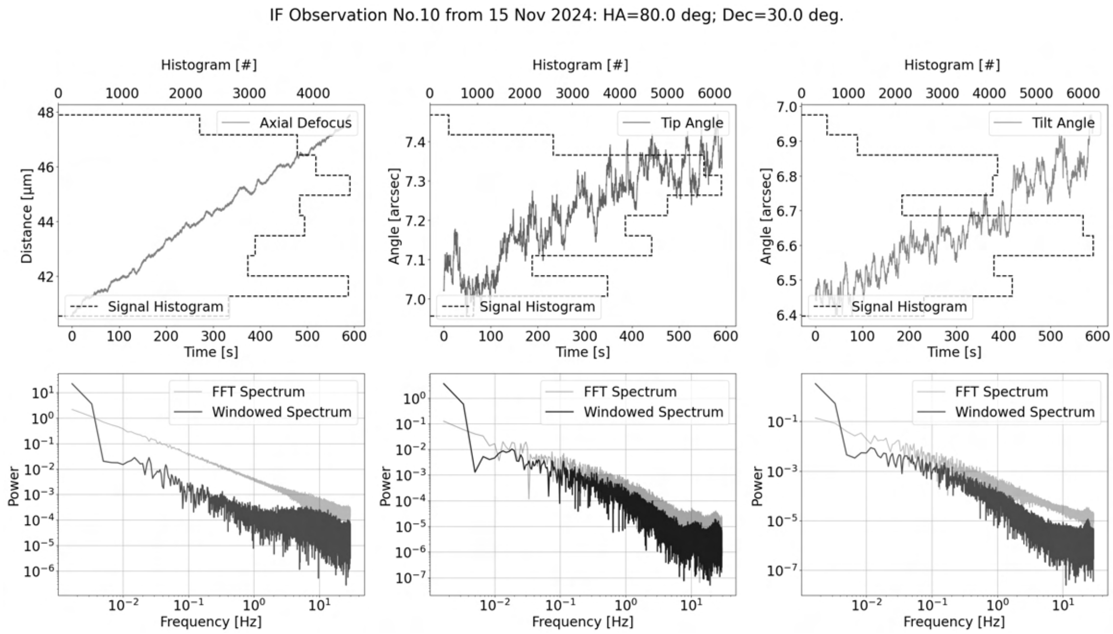

Figure A.19.: Plotsheet of interferometer observation no. 10 from November 15 2024.

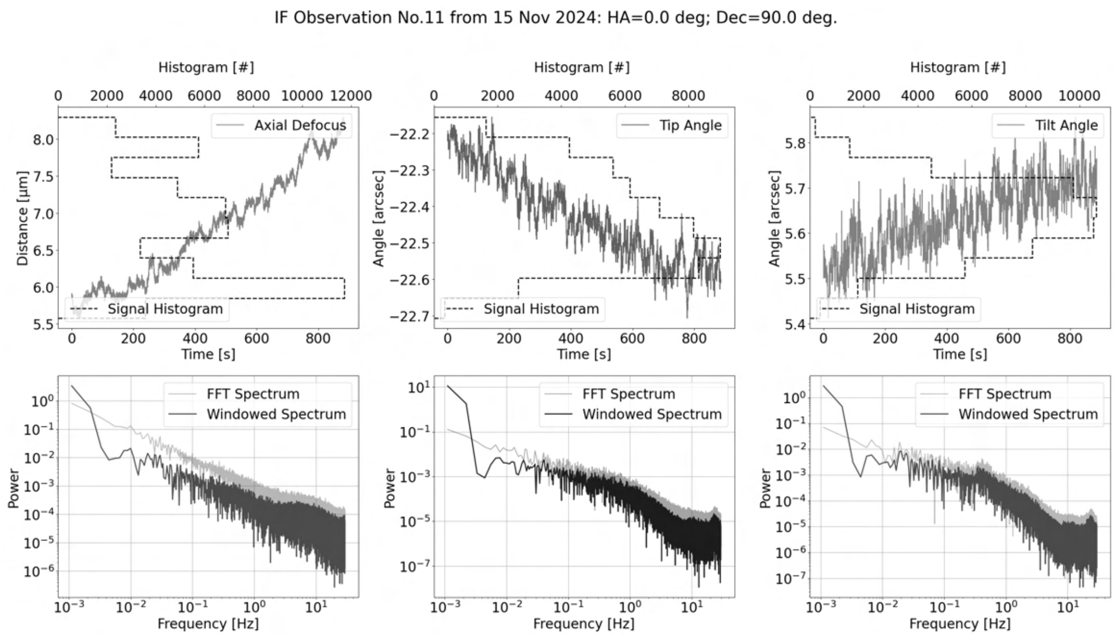

Figure A.20.: Plotsheet of interferometer observation no. 11 from November 15 2024.

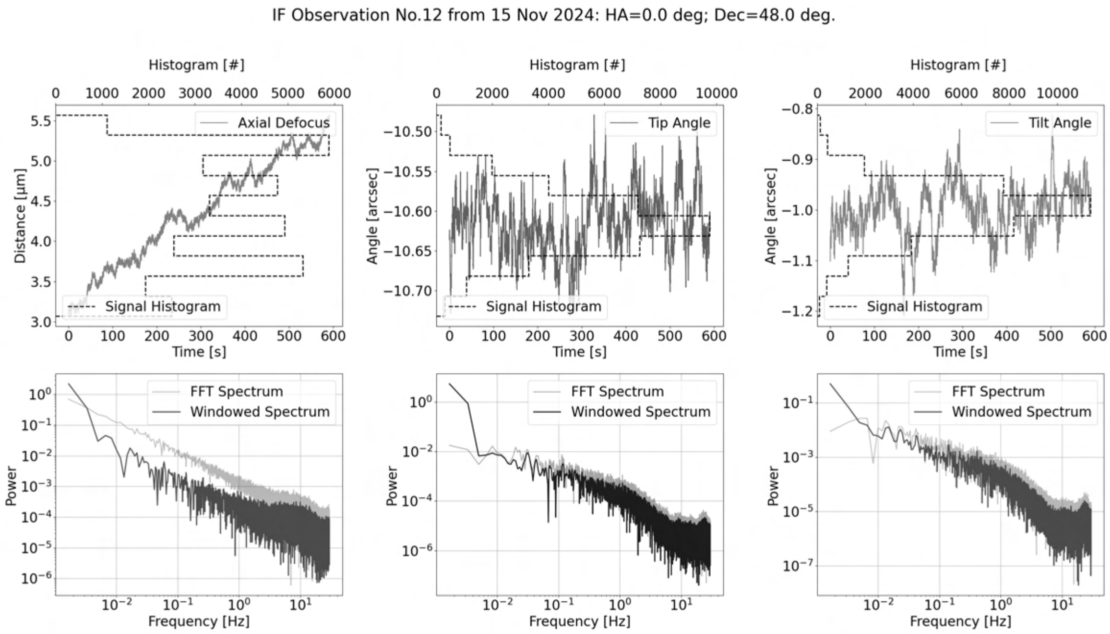

Figure A.21.: Plotsheet of interferometer observation no. 12 from November 15 2024.

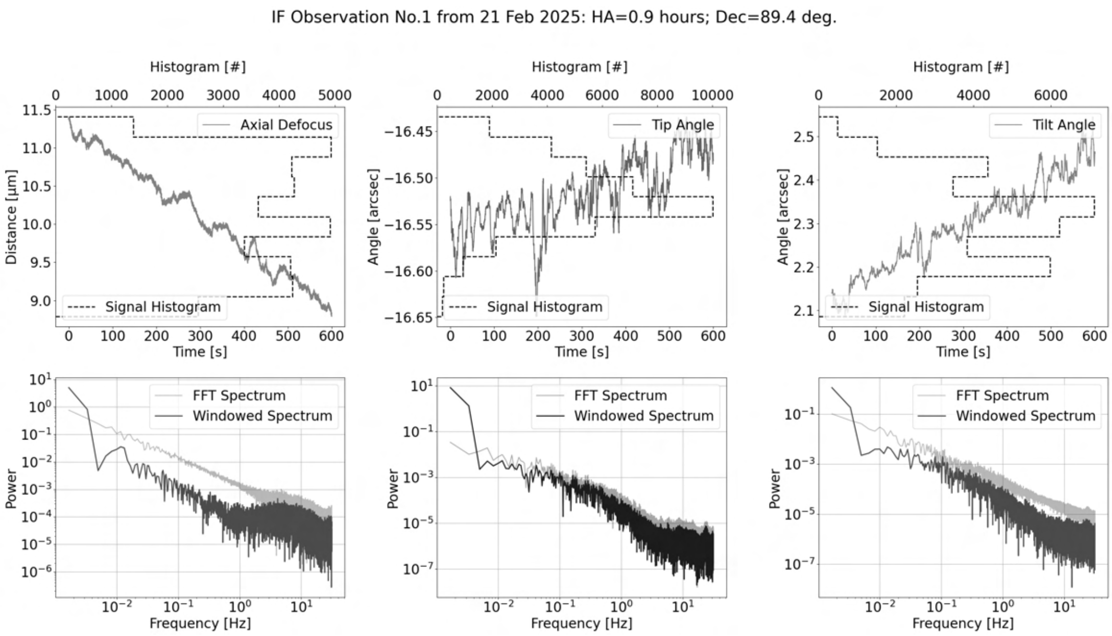

Figure A.22.: Plotsheet of interferometer observation no. 1 from February 21 2025.

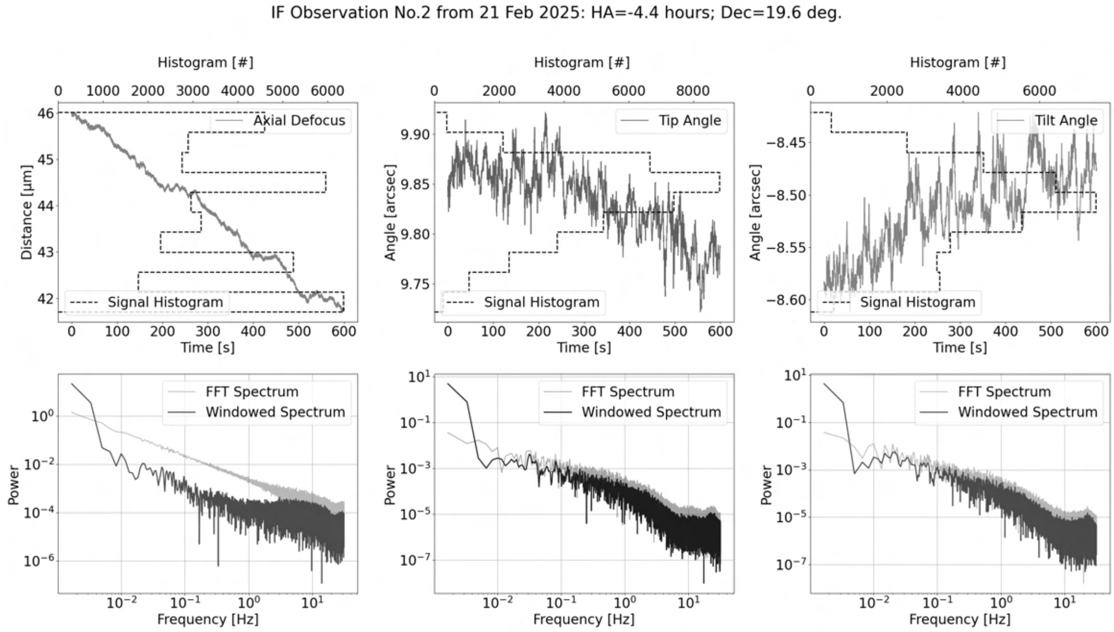

Figure A.23.: Plotsheet of interferometer observation no. 2 from February 21 2025.

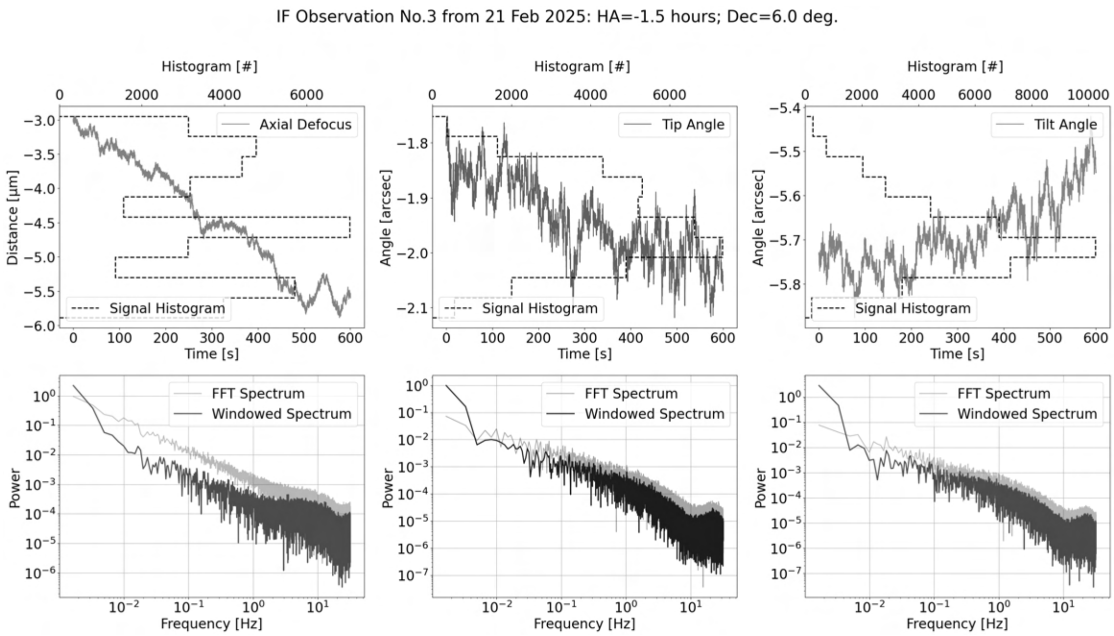

Figure A.24.: Plotsheet of interferometer observation no. 3 from February 21 2025.

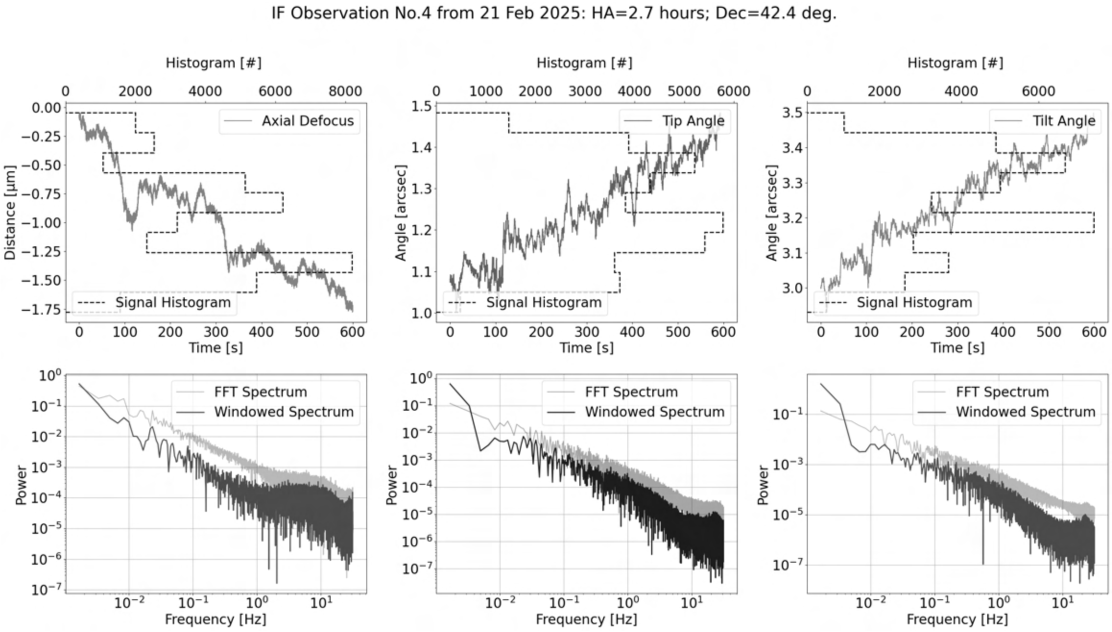

Figure A.25.: Plotsheet of interferometer observation no. 4 from February 21 2025.

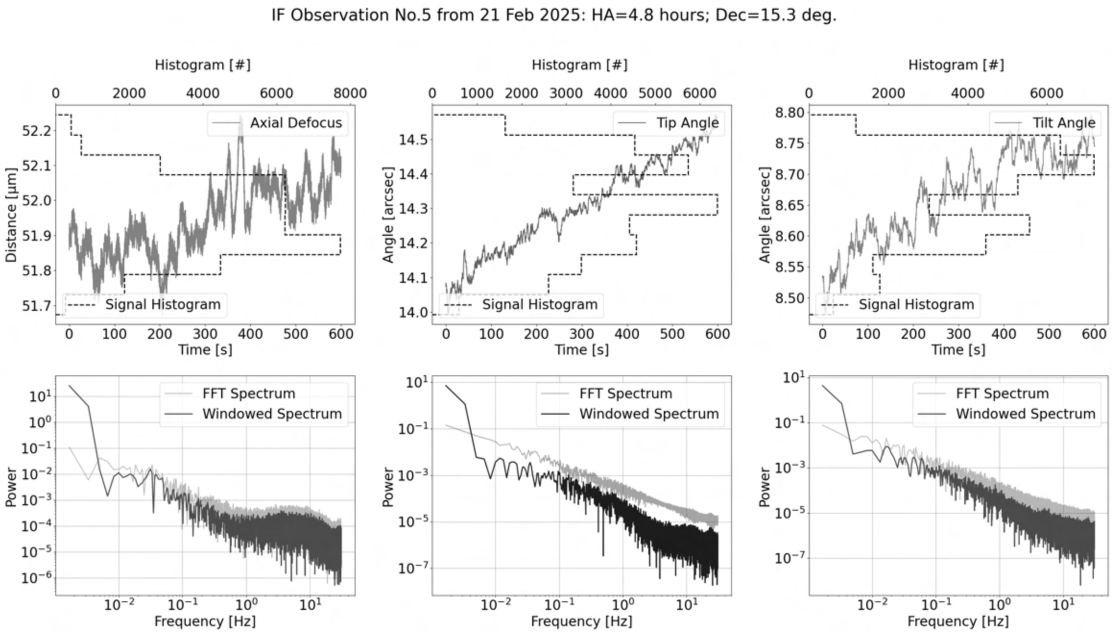

Figure A.26.: Plotsheet of interferometer observation no. 5 from February 21 2025.

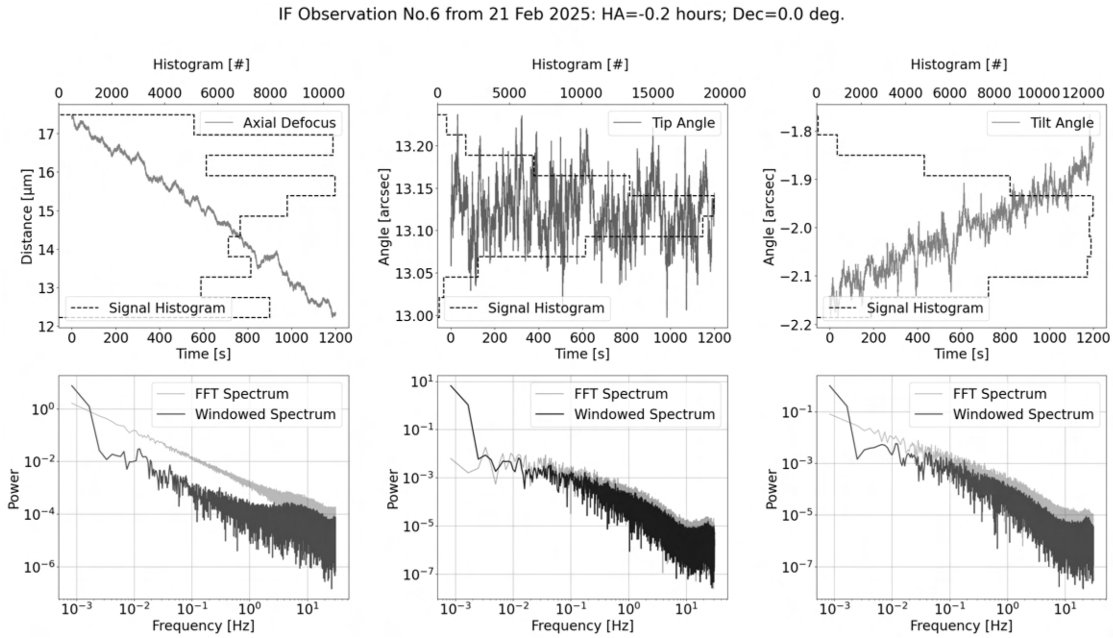

Figure A.27.: Plotsheet of interferometer observation no. 6 from February 21 2025.

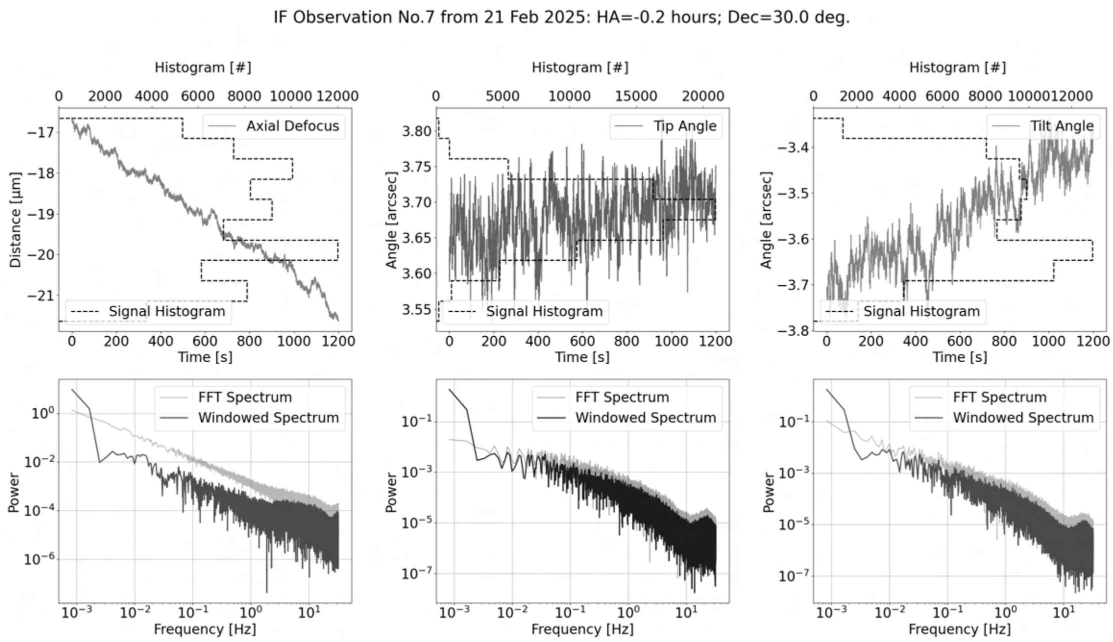

Figure A.28.: Plotsheet of interferometer observation no. 7 from February 21 2025.

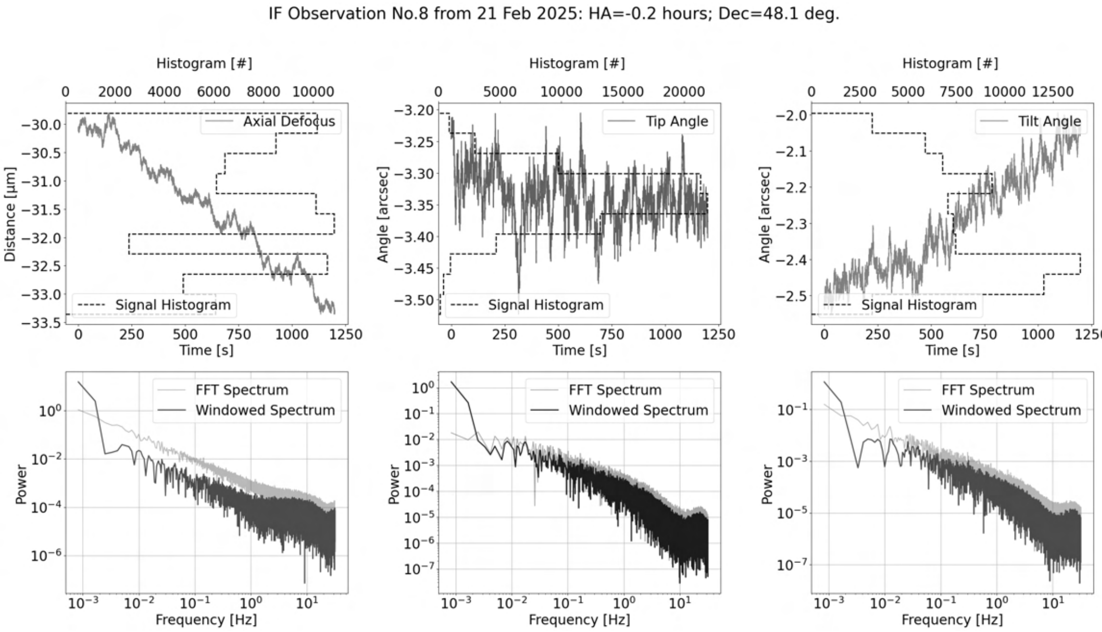

Figure A.29.: Plotsheet of interferometer observation no. 8 from February 21 2025.

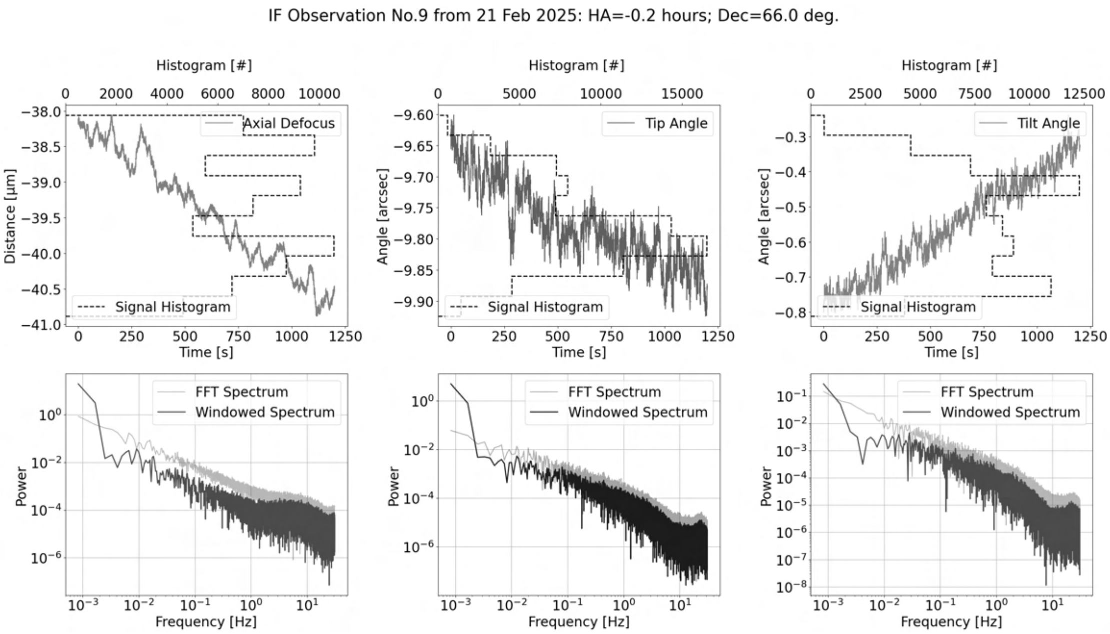

Figure A.30.: Plotsheet of interferometer observation no. 9 from February 21 2025.

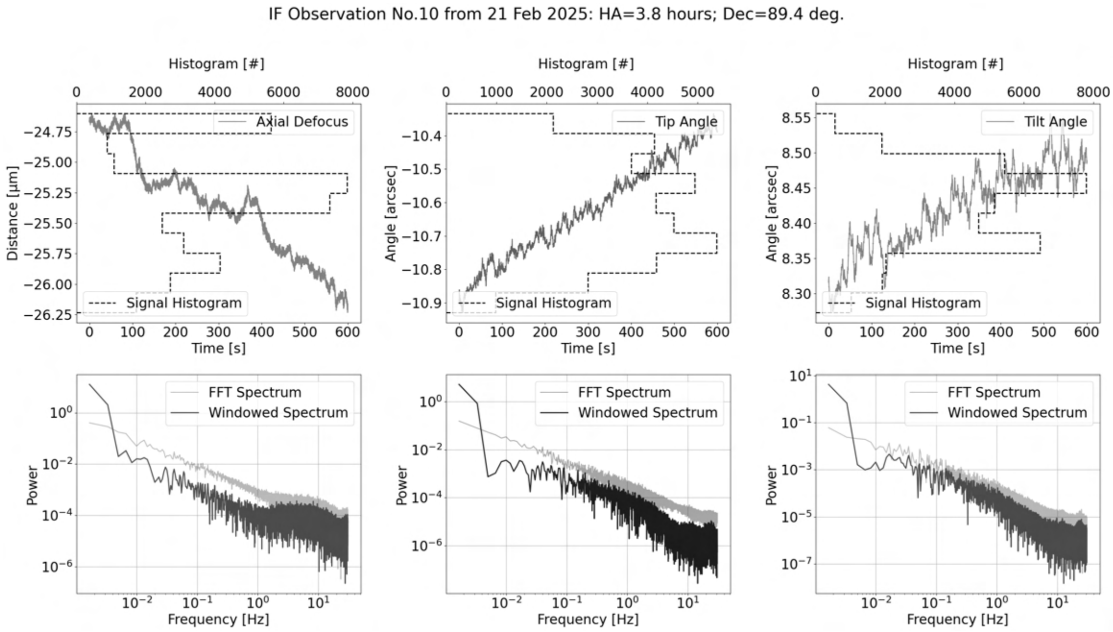

Figure A.31.: Plotsheet of interferometer observation no. 10 from February 21 2025.

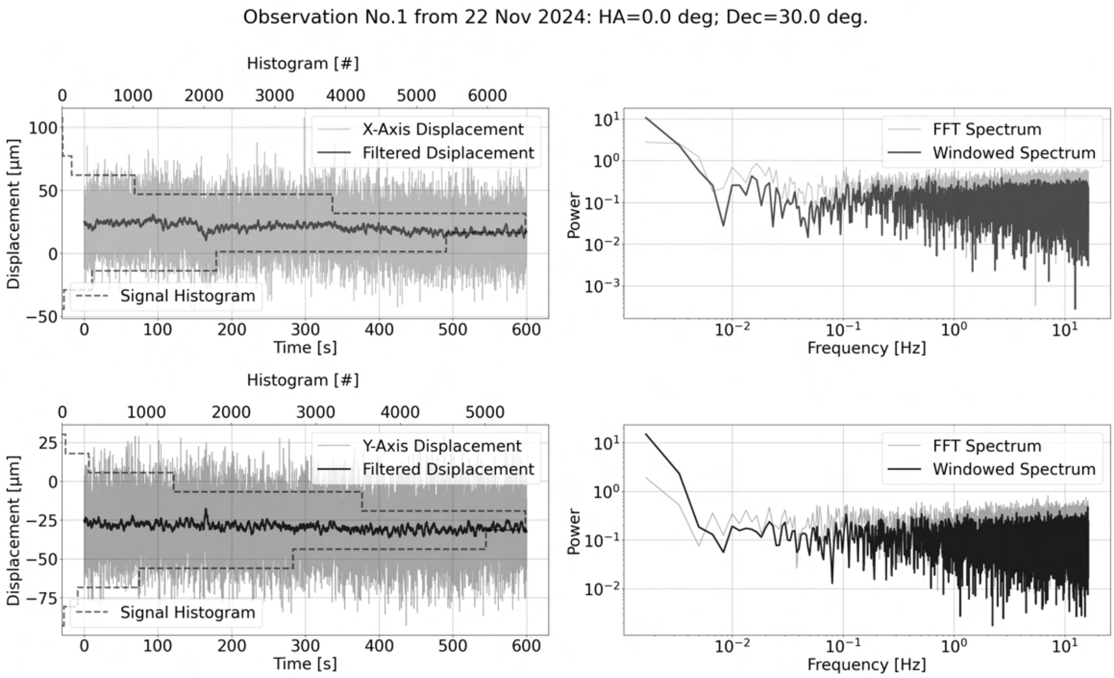

Figure A.32.: Plotsheet of lateral position observation no. 1 from November 22 2024.

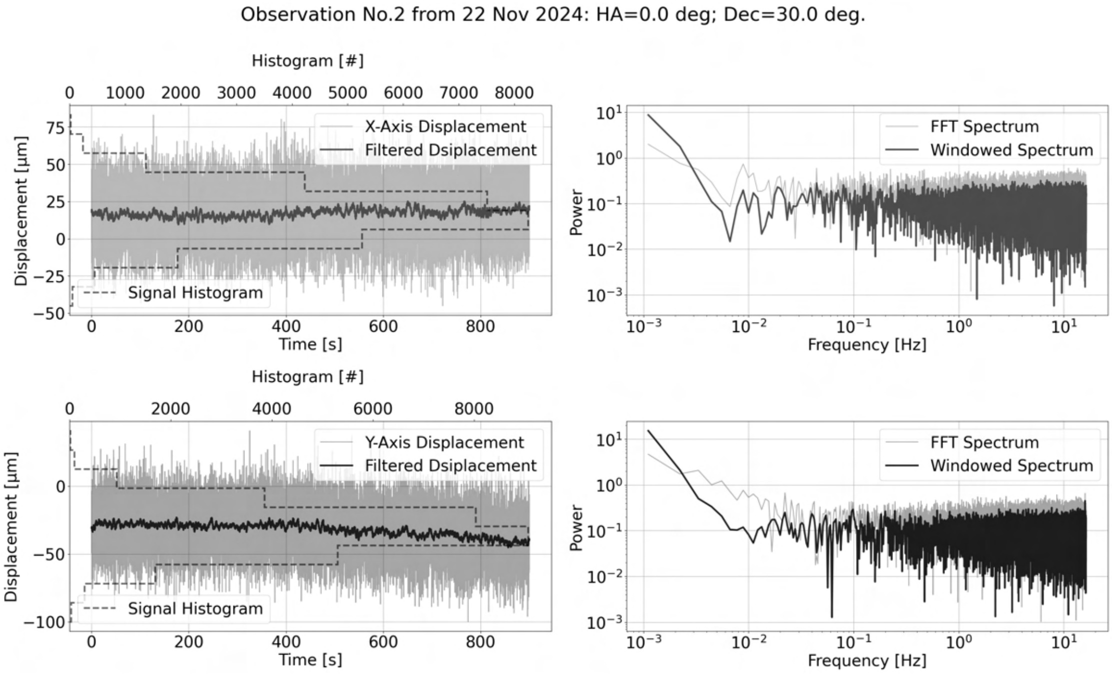

Figure A.33.: Plotsheet of lateral position observation no. 2 from November 22 2024.

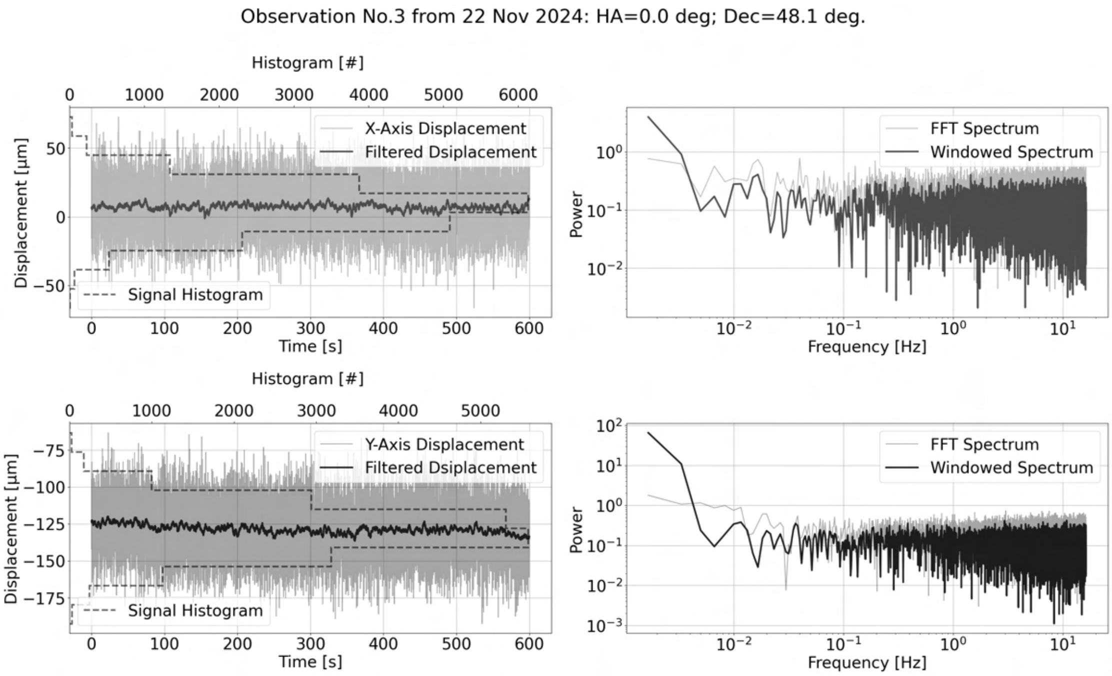

Figure A.34.: Plotsheet of lateral position observation no. 3 from November 22 2024.

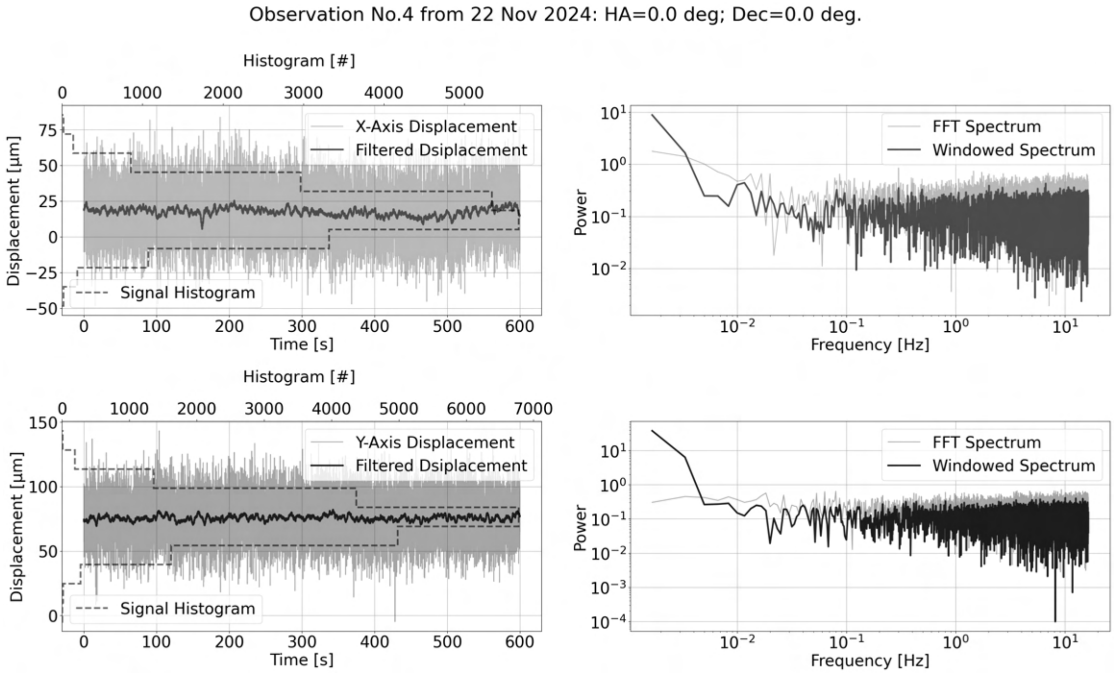

Figure A.35.: Plotsheet of lateral position observation no. 4 from November 22 2024.

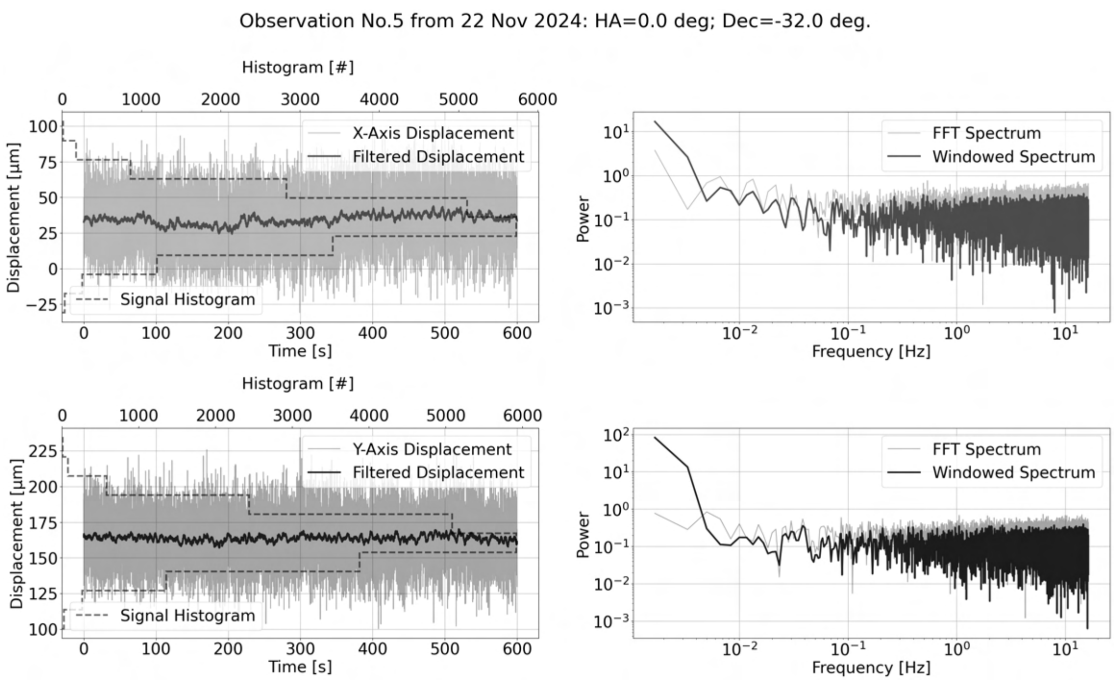

Figure A.36.: Plotsheet of lateral position observation no. 5 from November 22 2024.

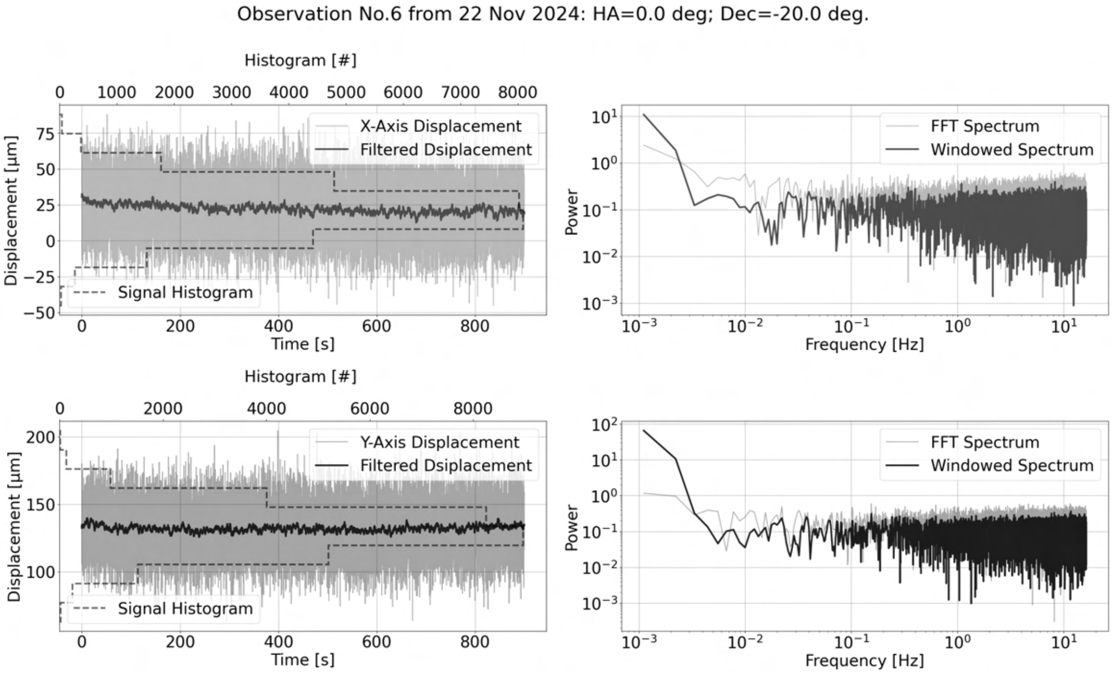

Figure A.37.: Plotsheet of lateral position observation no. 6 from November 22 2024.

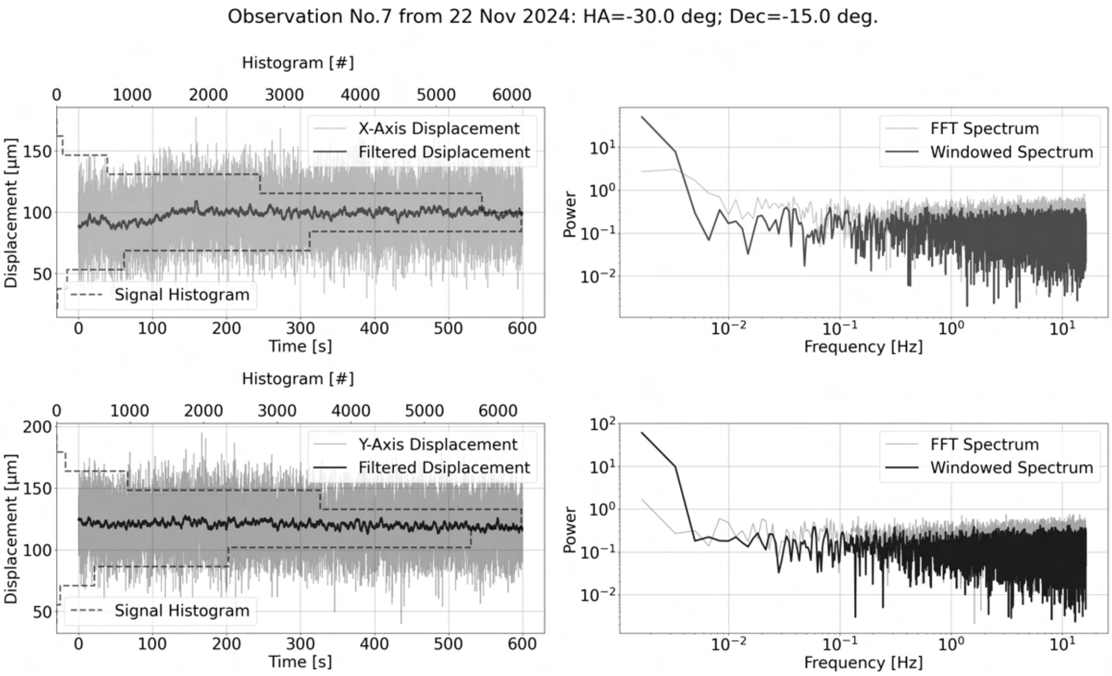

Figure A.38.: Plotsheet of lateral position observation no. 7 from November 22 2024.

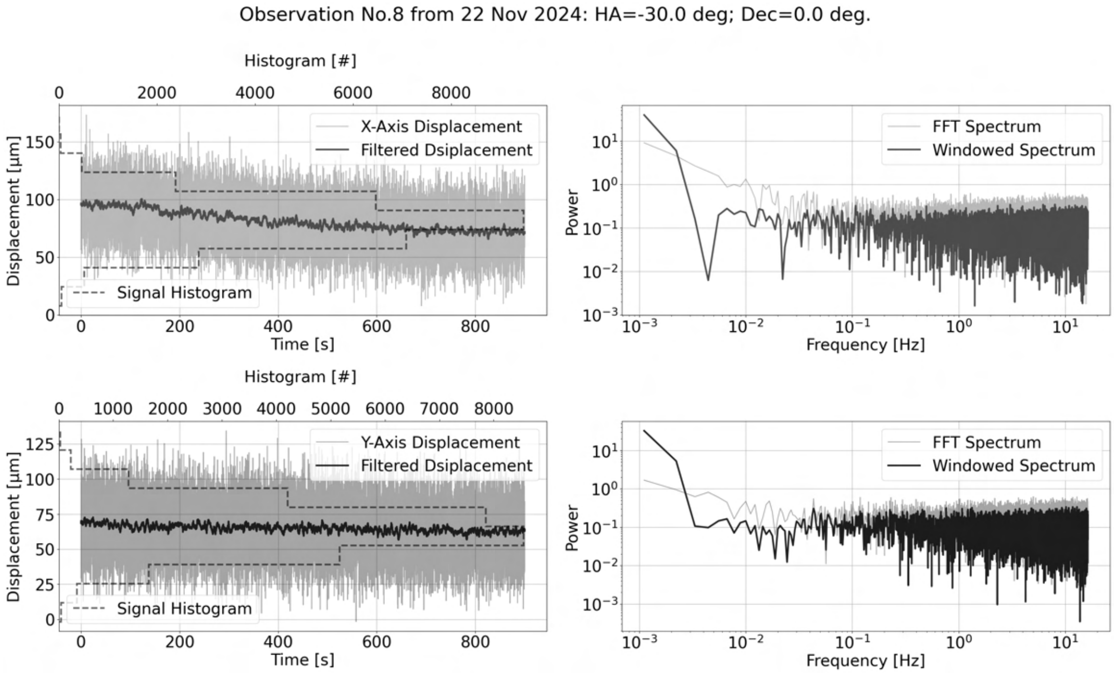

Figure A.39.: Plotsheet of lateral position observation no. 8 from November 22 2024.

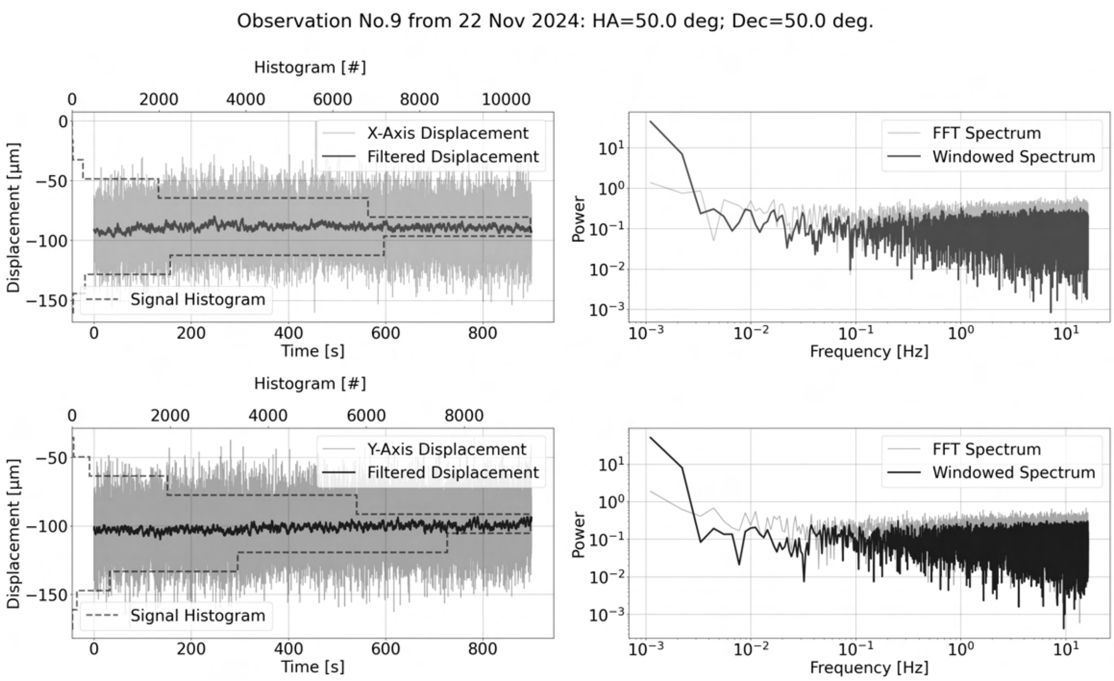

Figure A.40.: Plotsheet of lateral position observation no. 9 from November 22 2024.

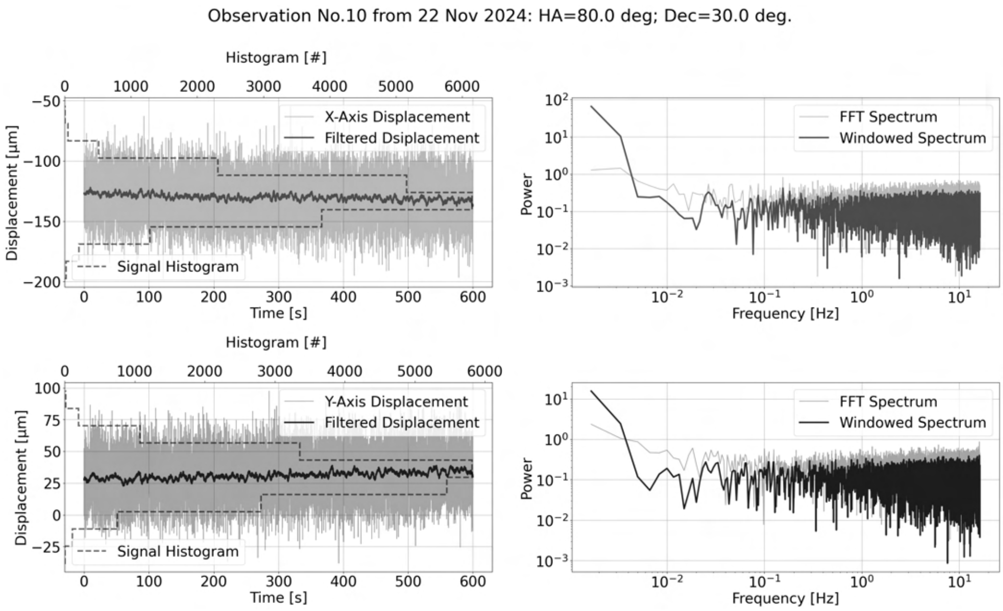

Figure A.41.: Plotsheet of lateral position observation no. 10 from November 22 2024.

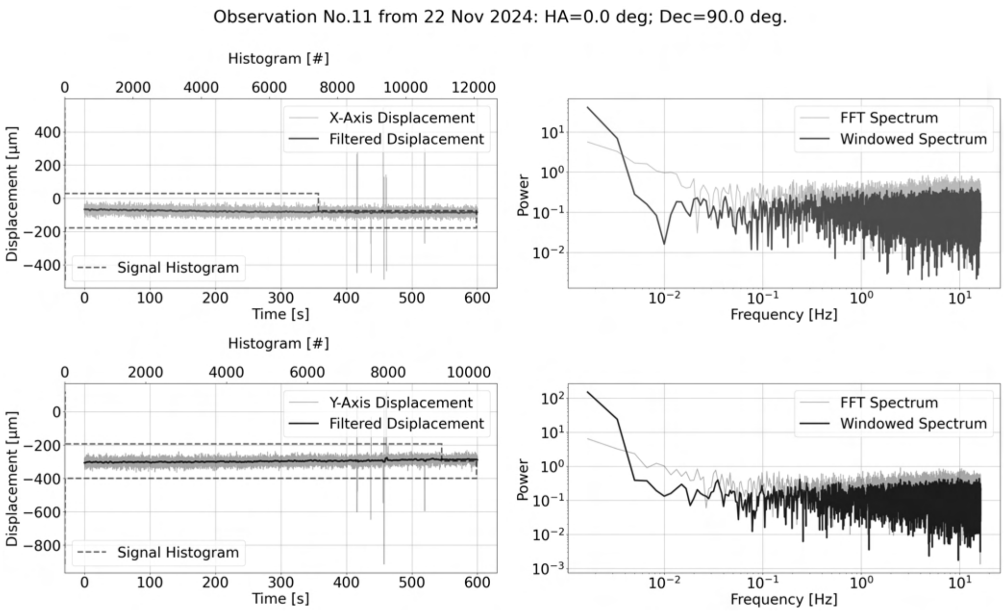

Figure A.42.: Plotsheet of lateral position observation no. 11 from November 22 2024. Measurement artifact of unknown origina, however likely caused by stray light or reflections.

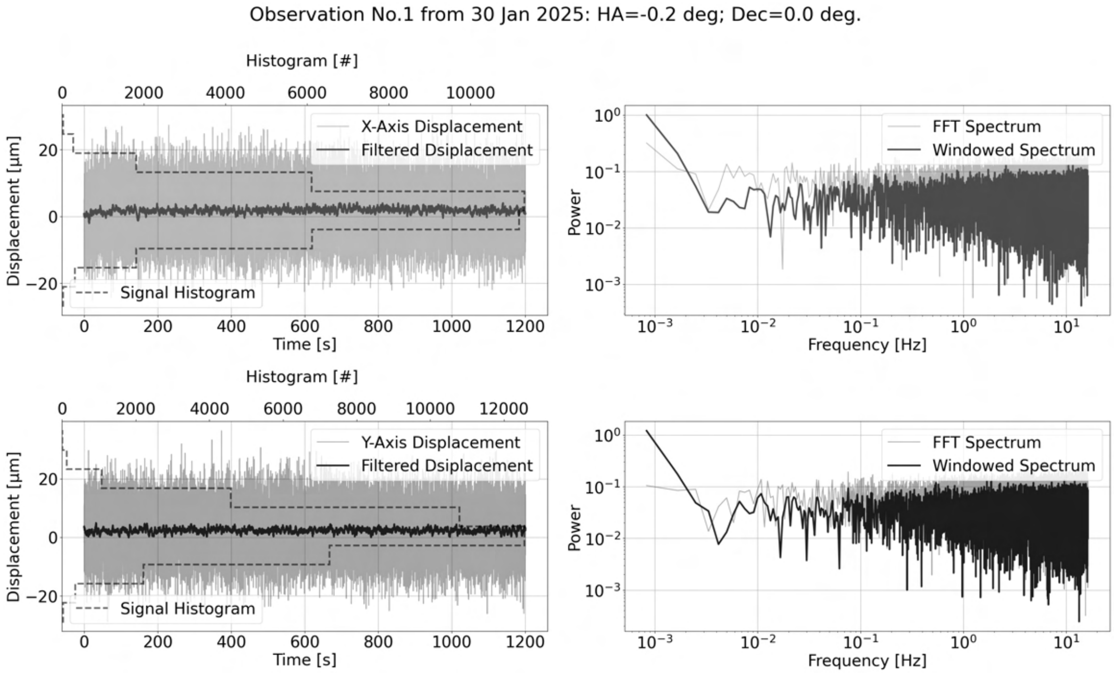

Figure A.43.: Plotsheet of lateral position observation no. 1 from January 30 2025.

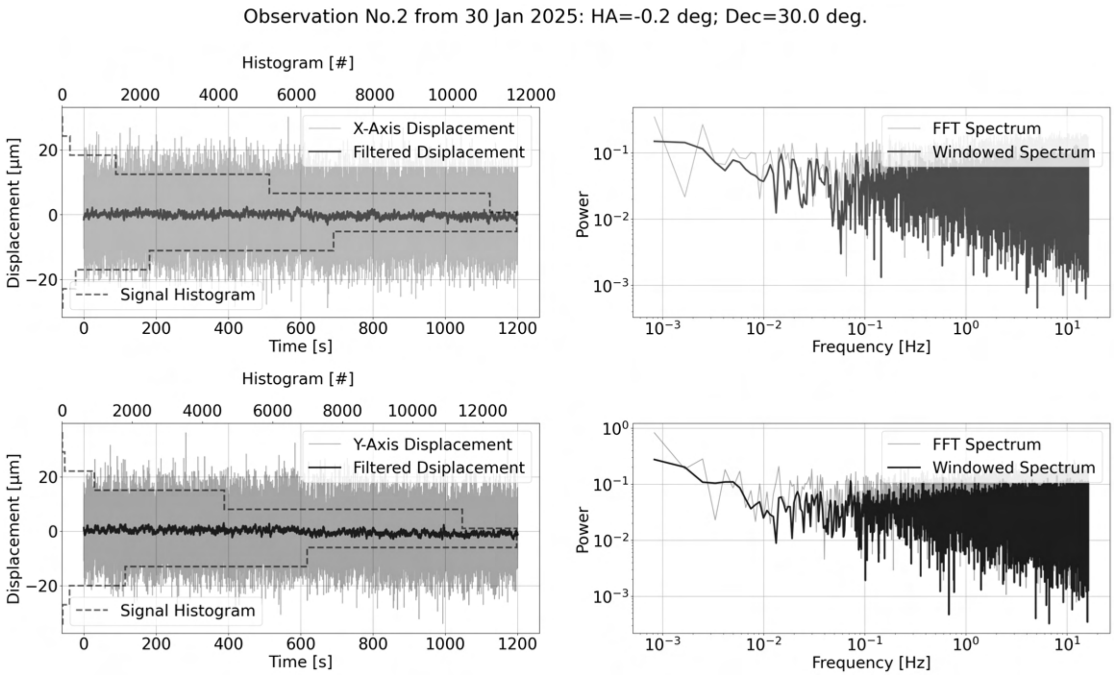

Figure A.44.: Plotsheet of lateral position observation no. 2 from January 30 2025.

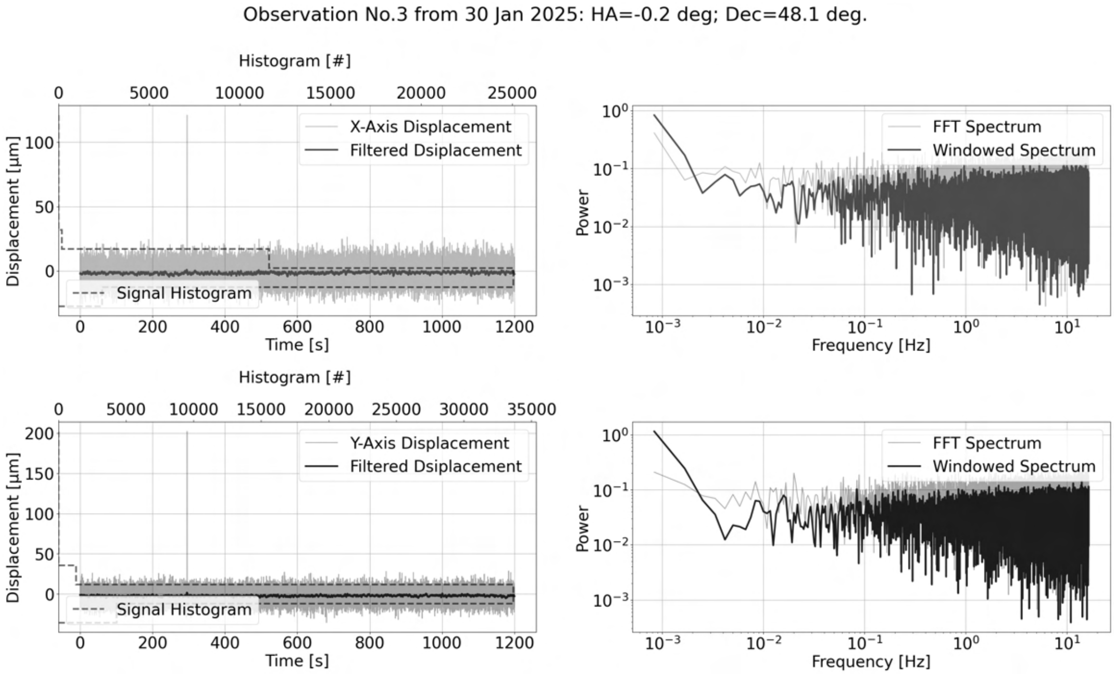

Figure A.45.: Plotsheet of lateral position observation no. 3 from January 30 2025. Measurement artifact of unknown origina, however likely caused by stray light or reflections.

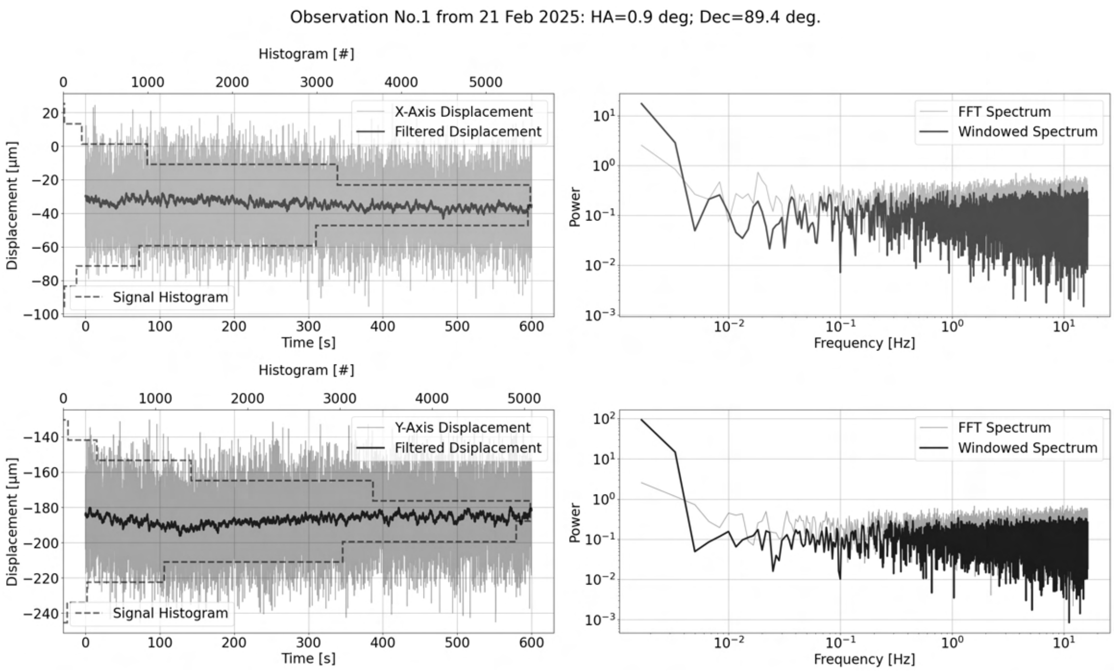

Figure A.46.: Plotsheet of lateral position observation no. 1 from February 21 2025.

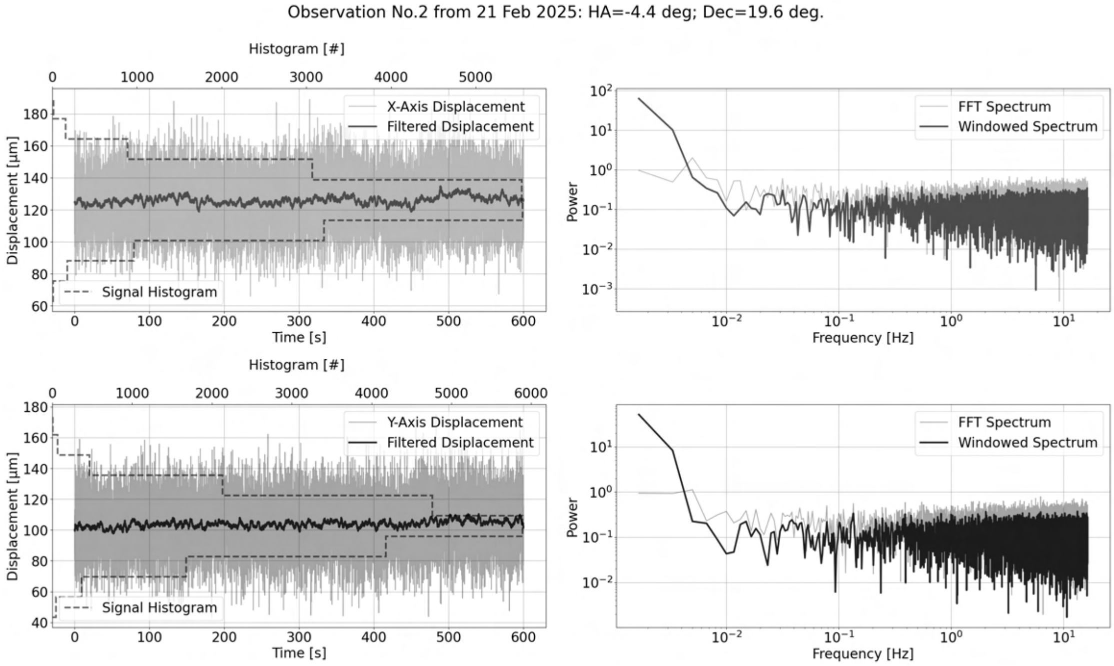

Figure A.47.: Plotsheet of lateral position observation no. 2 from February 21 2025.

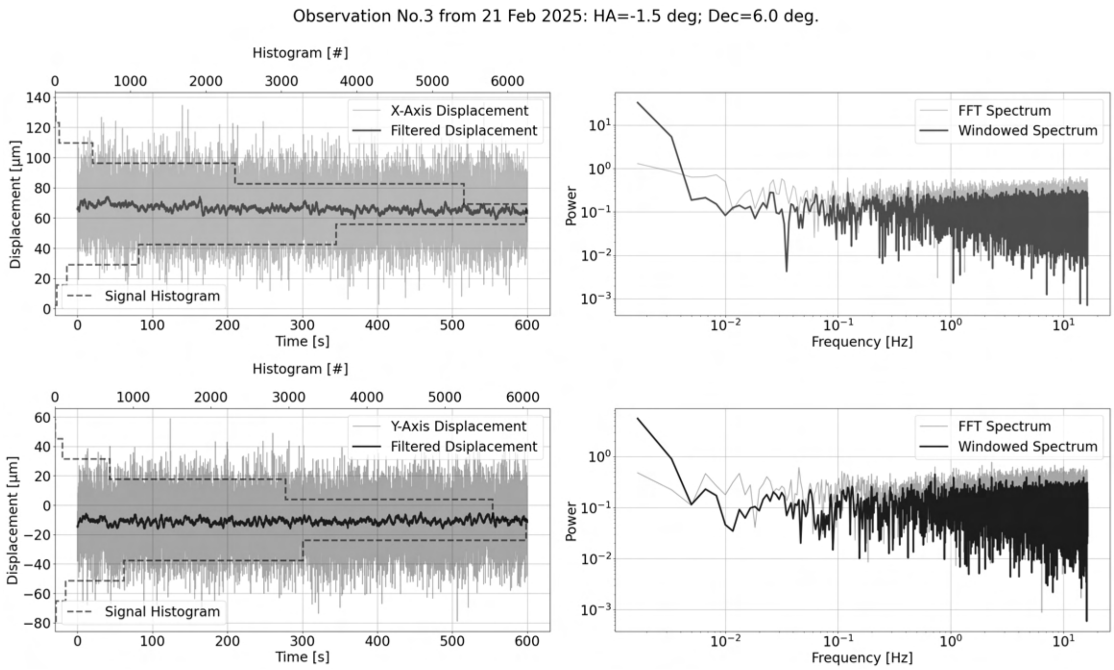

Figure A.48.: Plotsheet of lateral position observation no. 3 from February 21 2025.

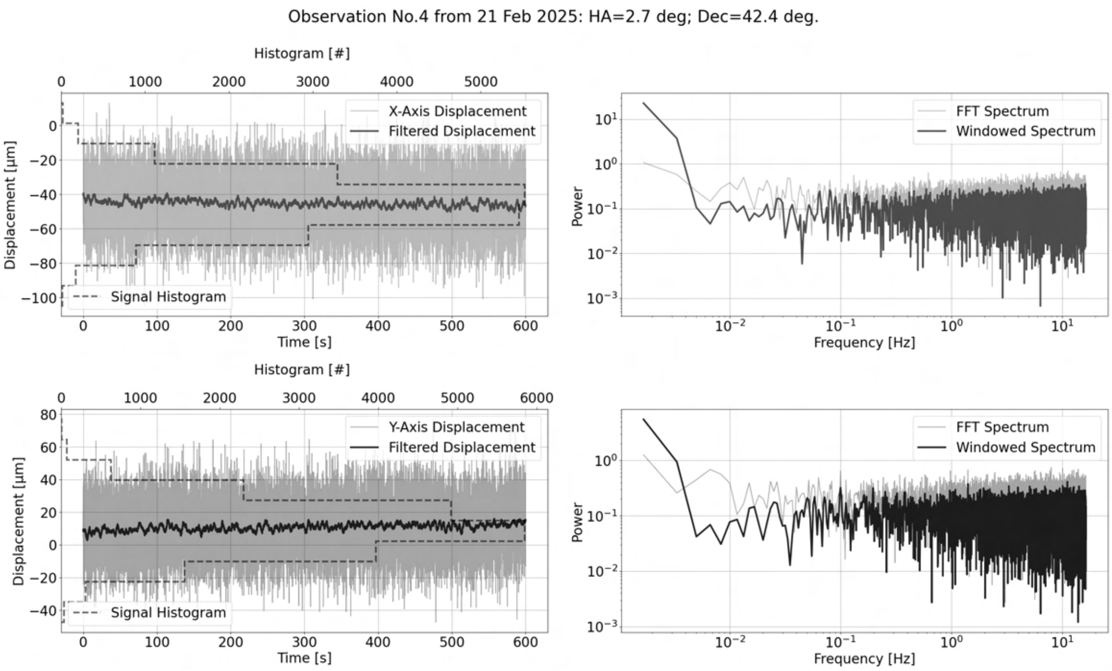

Figure A.49.: Plotsheet of lateral position observation no. 4 from February 21 2025.

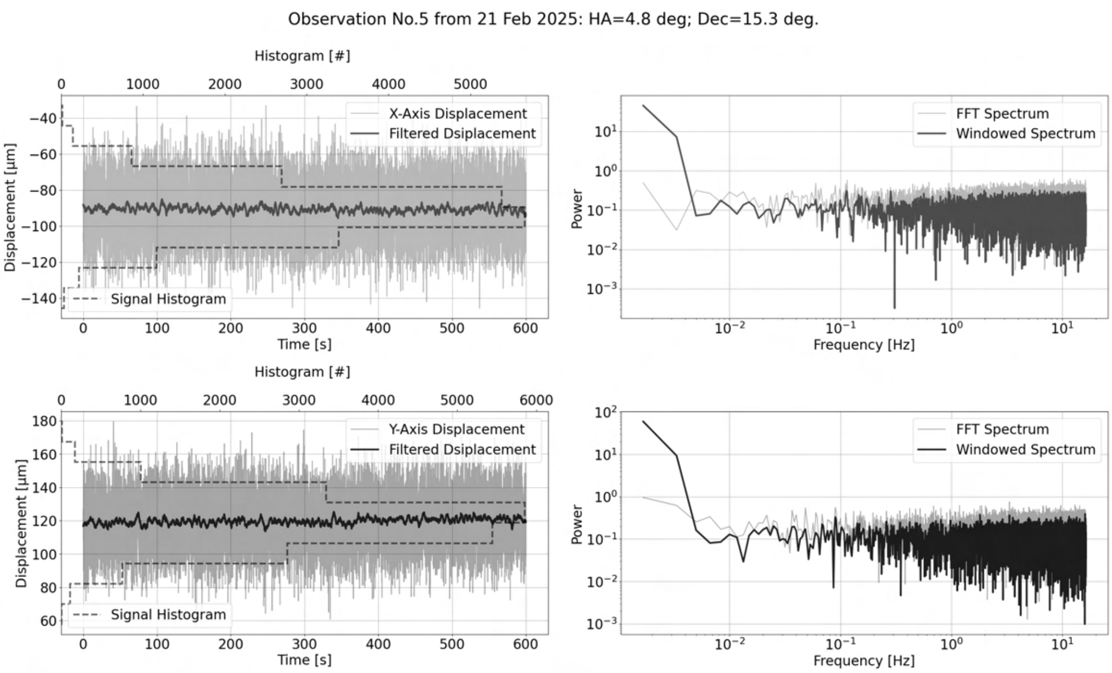

Figure A.50.: Plotsheet of lateral position observation no. 5 from February 21 2025.

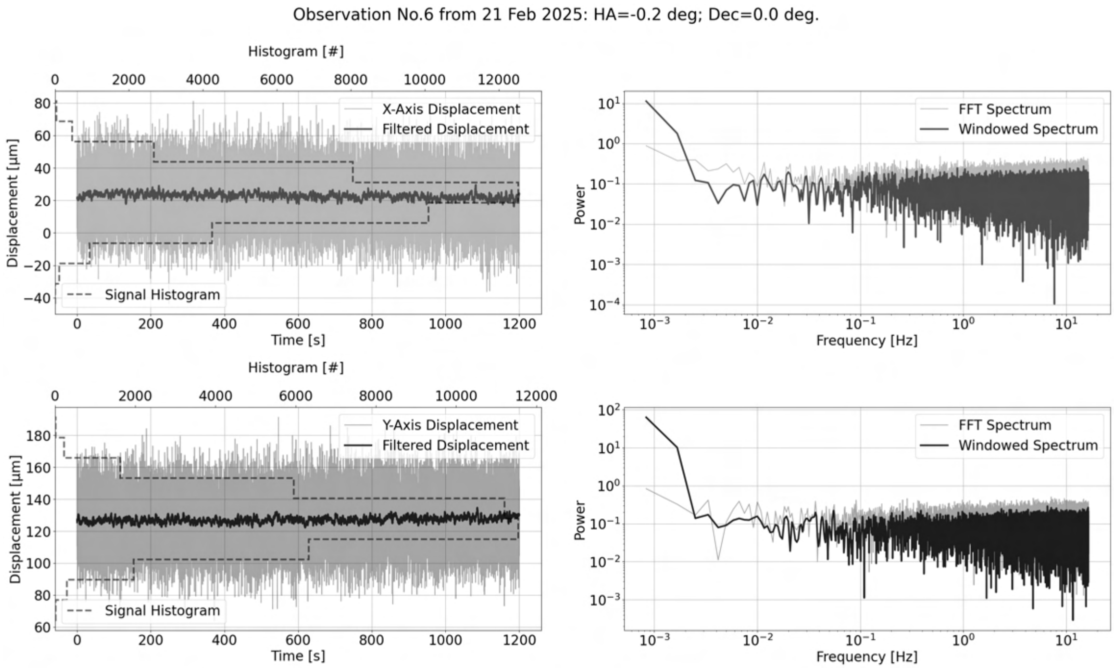

Figure A.51.: Plotsheet of lateral position observation no. 6 from February 21 2025.

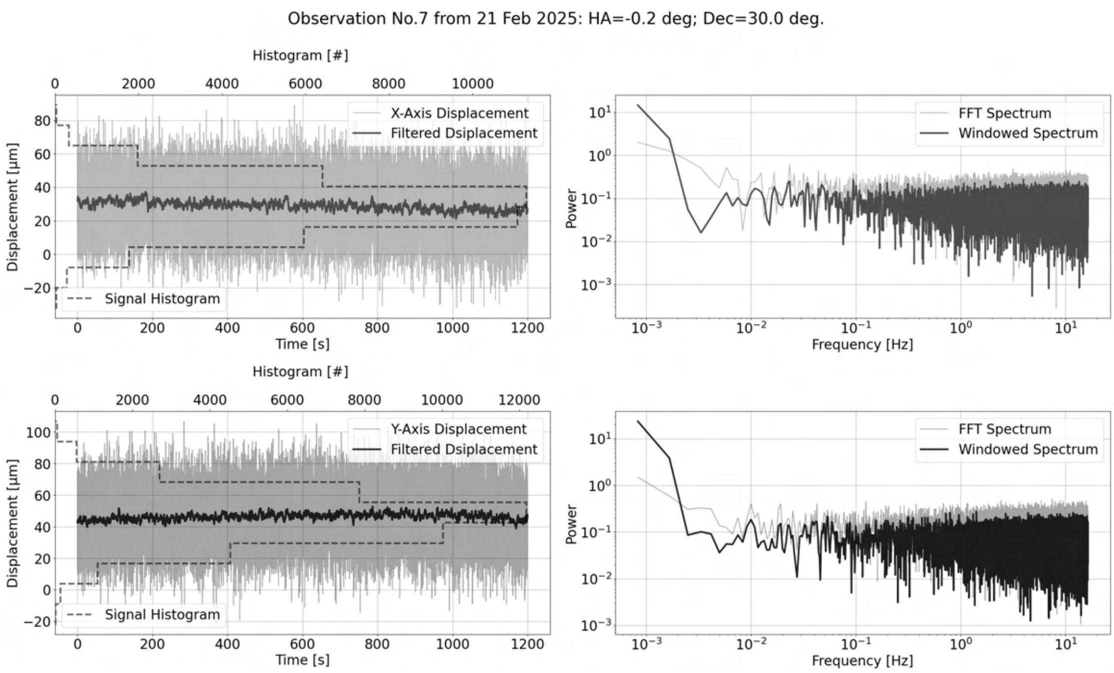

Figure A.52.: Plotsheet of lateral position observation no. 7 from February 21 2025.

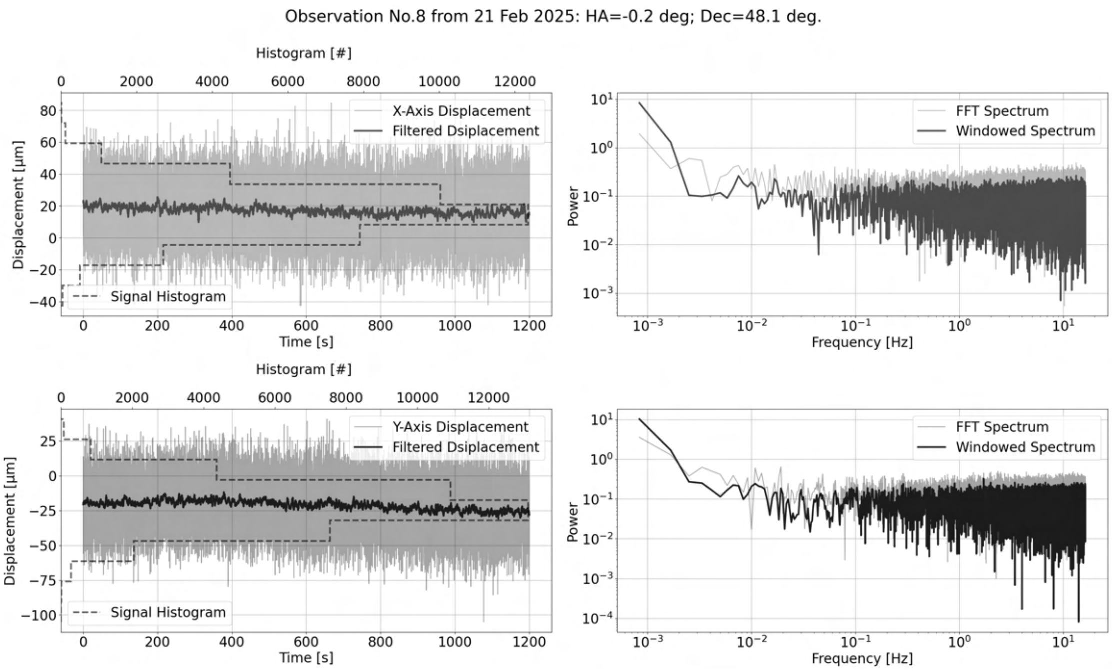

Figure A.53.: Plotsheet of lateral position observation no. 8 from February 21 2025.

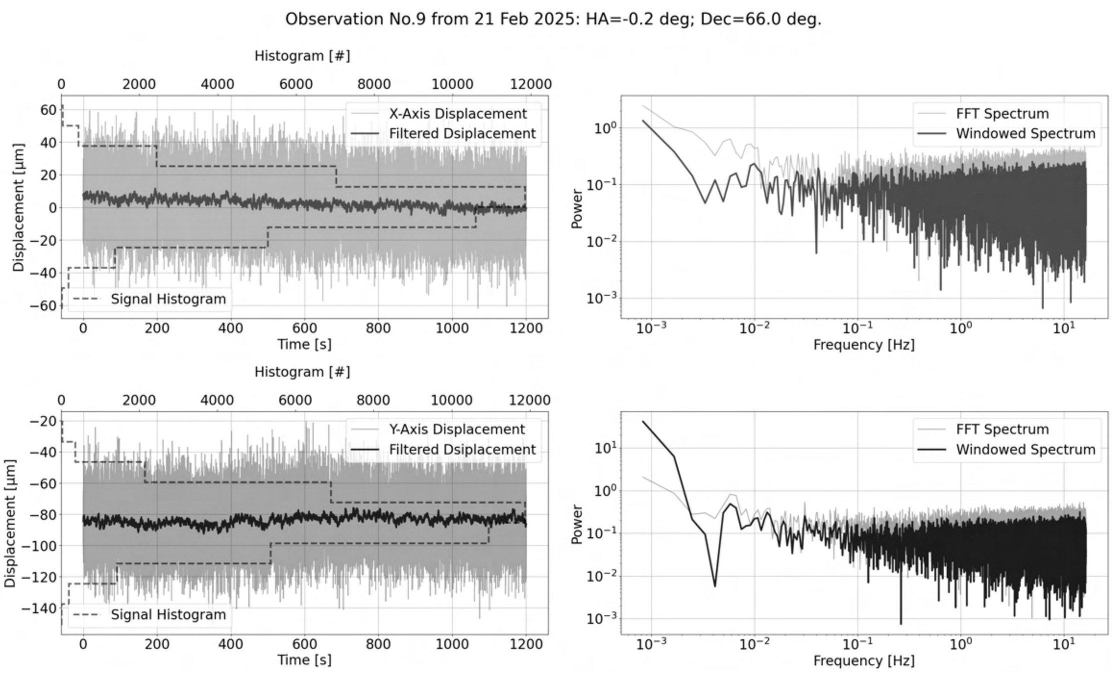

Figure A.54.: Plotsheet of lateral position observation no. 9 from February 21 2025.

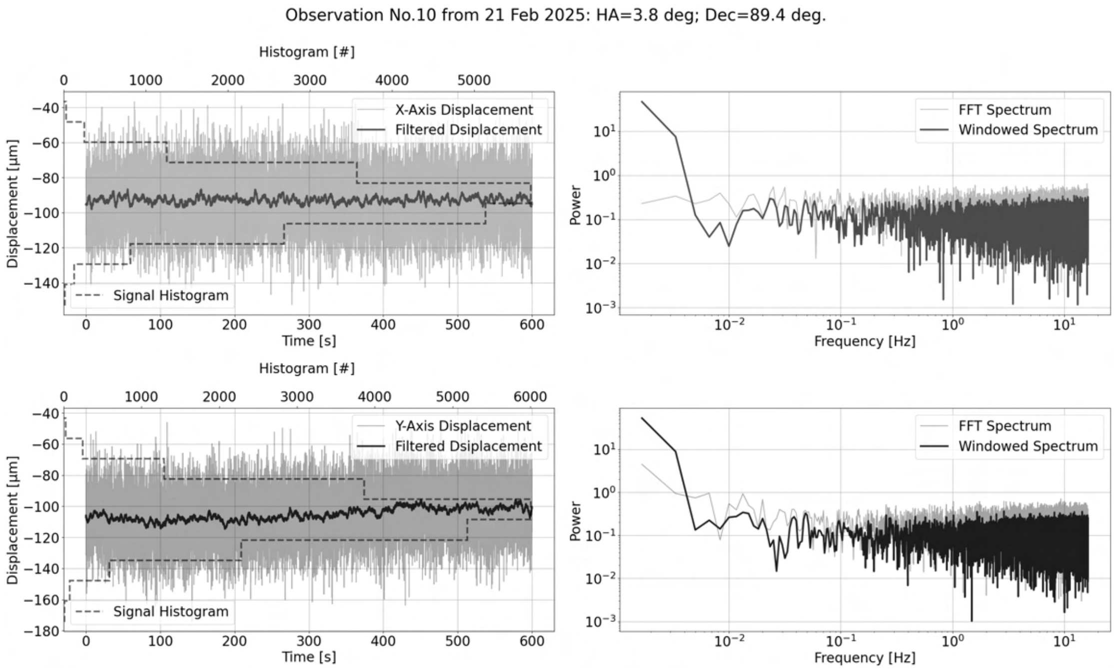

Figure A.55.: Plotsheet of lateral position observation no. 10 from February 21 2025.